BRNO UNIVERSITY OF TECHNOLOGY

VYSOKÉ UČENÍ TECHNICKÉ V BRNĚ

FACULTY OF MECHANICAL ENGINEERING

FAKULTA STROJNÍHO INŽENÝRSTVÍ

INSTITUTE OF PHYSICAL ENGINEERING

ÚSTAV FYZIKÁLNÍHO INŽENÝRSTVÍ

ENHANCED SPECTROSCOPY WITH PHOTONS AND ELECTRONS

ZESÍLENÁ SPEKTROSKOPIE S FOTONY A ELEKTRONY

MASTER'S THESIS

DIPLOMOVÁ PRÁCE

AUTHOR — Bc. Jiří Kabát

AUTOR PRÁCE

SUPERVISOR — doc. Ing. Andrea Konečná, Ph.D.

VEDOUCÍ PRÁCE

BRNO 2024

BRNO UNIVERSITY OF TECHNOLOGY
FACULTY OF MECHANICAL ENGINEERING

Assignment Master's Thesis

Institut:	Institute of Physical Engineering
Student:	**Bc. Jiří Kabát**
Degree programm:	Physical Engineering and Nanotechnology
Branch:	no specialisation
Supervisor:	**doc. Ing. Andrea Konečná, Ph.D.**
Academic year:	2023/24

As provided for by the Act No. 111/98 Coll. on higher education institutions and the BUT Study and Examination Regulations, the director of the Institute hereby assigns the following topic of Master's Thesis:

Enhanced spectroscopy with photons and electrons

Brief Description:

Infrared spectroscopy is widely used for studying the response of samples active in the infrared region, which support molecular vibrations or phonons. However, optical cross–sections of the molecular vibrations in minute amounts of analytes are typically very small and the associated signal can disappear in the measured spectrum. This problem can be overcome by placing the sample in a strong near field produced e.g. by a rough substrate or a plasmonic antenna. The enhancement of the signal has been observed in the case of molecules adsorbed on rough films on which the roughness acts as a confining entity, which provides signal enhancement by a few orders of magnitude. Much larger enhancement is observed if the molecules are placed into the near field of a plasmonic nanoantenna, which has its resonance tuned to the resonance frequency of the molecule vibration. These mechanisms are utilized in experimental techniques such as surface–enhanced infrared absorption (SEIRA), surface–enhanced Raman spectroscopy (SERS), or tip–enhanced Raman spectroscopy (TERS).

The aforementioned techniques can provide excellent spectral resolution, but only a diffraction–limited spatial resolution. To gain information on the localization of the molecular sample, it has been suggested to utilize electron energy loss spectroscopy (EELS) with a focused electron beam, which could provide spatial resolution down to units or tens of nanometers.

This master’s thesis will focus on the theoretical description and optimization of the acquired enhanced signal as probed by photons and electrons, by using analytical and numerical calculations.

Master's Thesis goals:

1) Review and theoretically describe the enhanced spectroscopic methods with light (e.g., surface–enhanced infrared absorption and scattering) enabling the detection of small molecular amounts.
2) Find electron–based analogs to the light–based enhanced spectroscopies. Suggest a suitable theoretical description of the enhanced spectroscopy with electrons.
3) Select a suitable sample system (e.g., a metallic nanorod or surface functionalized with molecules) and theoretically study the sensitivity of the enhanced spectroscopies concerning the type of the collected signal.

Recommended bibliography:

NEUMAN, Tomáš, et al. Importance of plasmonic scattering for an optimal enhancement of vibrational absorption in SEIRA with linear metallic antennas. The Journal of Physical Chemistry C. 2015, vol. 119, issue 47, pp. 26652 - 26662.

KONEČNÁ, Andrea, et al. Surface-enhanced molecular electron energy loss spectroscopy. ACS Nano. 2018, vol. 12, issue 5, pp. 4775 - 4786.

Deadline for submission Master's Thesis is given by the Schedule of the Academic year 2023/24

In Brno,

L. S.

prof. RNDr. Tomáš Šikola, CSc. Director of the Institute	doc. Ing. Jiří Hlinka, Ph.D. FME dean

Abstrakt
Jednou z hlavních aplikací infračervené spektroskopie je analýza složení a chemických vlastností molekulárních vzorků. Techniky infračervené spektroskopie dalekého pole však často mají problém detekovat malá množství molekul. Jedním ze způsobů, jak překonat nízký signál malých molekulárních množství, je pokud je vystavíme vlivu silného blízkého pole. V této práci teoreticky studujeme zesílenou infračervenou spektroskopii s fotonovými a elektronovými sondami. Nejprve představíme řešerši se zaměřením na elektrodynamiku a nanofotoniku. Poté ukážeme výsledky numerických a analytických výpočtů pro optické účinné průřezy a spektra energiových ztrát elektronů pro nanoantény. Hlavní část této práce se zabývá semianalytickým modelováním systému anténa-molekuly, kde porovnáváme modelované výsledky molekulárních signatur ve spektrech s numerickými simulacemi. V neposlední řadě stanovíme měřítka pro návrh nanoantény s nejvyšším výkonem v zesílené spektroskopii pro uvažovaný systém a detekci signálu.

Summary
One of the main applications of infrared spectroscopy is analysis of the composition and chemical properties of molecular samples. However, the far-field infrared spectroscopy techniques often suffer to detect small amounts of molecules. One of the ways to overcome the low signal of minute molecular amounts is by introducing the influence of a strong near field. In this thesis, we theoretically study the enhanced infrared spectroscopy with photon and electron probes. First, we review the theoretical background, with a focus on electrodynamics and nanophotonics. Then we show the results of numerical and analytical calculations for the optical cross sections and the electron energy loss spectra for nano-antennas. The main part of this thesis deals with semi-analytical modeling of the antenna-molecules system, where we compare the results of molecular signatures in the spectra from the model with the numerical simulations. Last, we establish figures of merit for designing nano-antenna with the best performance in enhanced spectroscopy for the considered system and signal detection.

Klíčová slova
molekulární vibrace, povrchově zesílená infračervená spektroskopie absorbce, nanoanténa, spektroskopie energiových ztrát elektronů

Keywords
molecular vibrations, surface-enhanced infrared absorption spectroscopy, nano-antenna, electron energy-loss spectroscopy

KABÁT, J. *Enhanced spectroscopy with photons and electrons* . Brno: Vysoké učení technické v Brně, Fakulta strojního inženýrství, 2024. 102 s. Vedoucí diplomové práce doc. Ing. Andrea Konečná, Ph.D..

I hereby declare that I have written this diploma thesis on the topic of *Enhanced spectroscopy with photons and electrons* autonomously under the scientific supervision of doc. Ing. Andrea Konečná, Ph.D.. All of the sources, references, and literature used throughout the thesis are properly cited in the reference list.

Bc. Jiří Kabát

The part of the results in Chapter 4 about enhanced spectroscopy with photons is based on work done during my six-month Erasmus+ stay in CIC nanoGUNE BRTA, 20018 Donostia-San Sebastián, Basque Country, Spain. During my stay, I was supervised by Dr. Martin Schnell, who I acknowledge for proposing the idea behind this project and for co-supervising the results even after my return back to Brno.

Bc. Jiří Kabát

Firstly I would like to thank to my supervisor doc. Ing. Andrea Konečná Ph.D.. Andrea thank you for all your time and effort you spent regarding this thesis and all the other of my scientific activities. Even when you have so many things on your schedule, with the projects, teaching, and your great scientific journey, you have always found the time for meetings and consultations. Thank you for being such a great mentor and I am grateful that I can work with you.

I would also like to thank the Brno University of Technology for letting me go on Erasmus+ stay. I thank Andrea for proposing and arranging the stay with prof. Rainer Hillenbrand in CIC nanoGUNE in Donostia-San Sebastián. Thank you Rainer for making my stay possible. I want to thank my supervisor during the Erasmus+ stay, Dr. Martin Schnell. Martin, thank you for always being patient and helpful, even at the start, when I had to learn so many new things. The collaboration with you is really pleasant, and I hope for much more. Thank you, Jan, for helping me for the half year, discussing Spanish and life. I hope to see you soon on either kalimotxo or here in Brno. Thank you Carlos Maciel Escudero for always being helpful and kind and helping me with simulations, I am looking up to you as one of my heroes, you are the best! Thank you to all the members of the nano-optics group for the warm half-year in Donostia, I wish you all the best.

I want to thank all the members of the ARTEMIS group, for listening to my talks and giving me feedback, and also the Institute of Physical Engineering FME BUT for providing me the possibility to study these scientific topics.

Drazí rodiče, drahá Eli a Ondro, děkuju vám za veškerou pomoc, rady a přizpůsobování se během celého studia. Moc pro mě všichni znamenáte.

Děkuji dědo, za podporu ve směru, kterým jsem se rozhodl ubírat a naše neustálé hovory. Díky Tome a Pepo, za vzájemné pohánění se směrem ke konci. Velké poděkování patří Rosťovi, který mi během celého studia pomáhal a chvílemi držel nad vodou.

V neposlední řadě děkuji Terezce, za podporu a lásku. Sám bych si všechny životní radosti neužil a překážky nezvládl a moc pro mě znamená, že jsme na to spolu.

Bc. Jiří Kabát

Contents

Introduction

Grau, teurer Freund, ist alle Theorie
und grün des Lebens goldner Baum.

Johann Wolfgang von Goethe
Faust

One of the main applications of infrared spectroscopy is analysis of the composition and chemical properties of molecular samples. With the obtained spectra, one can determine which chemical groups are present in the studied sample, their concentration, identify the chemical bonds, or even the potential chemical reactions [1]. Because of the relatively small optical cross section of the molecules, large amounts of the sample are usually needed for a conclusive measurement and data analysis.

In this context, so-called enhanced spectroscopies emerge as promising candidates for overcoming this hindrance of low signal. By introducing strong near fields that excite the molecular samples, the signals obtained by the measurement can be enhanced by a few orders of magnitudes [2]. Among the enhanced spectroscopy techniques, the most prominent are surface-enhanced fluorescence (SEF) [3], surface-enhanced infrared absorption (SEIRA) [4], surface-enhanced Raman spectroscopy (SERS) [5], or tip-enhanced Raman spectroscopy (TERS) [6]. Much larger enhancement is observed if the molecules are placed into the near field of a resonant nanostructure (e.g. nano-antenna), which has its resonance tuned to the resonance frequency of the molecule vibration [7]. Another direction of the enhanced spectroscopies may be their utilization in spectroscopies based on an inelastic interaction between the sample and fast electrons. The signal enhancement would allow the study of minute amounts of samples and grant unprecedented spatial resolution, with the possibility of studying vibrational sample response, which emerged in recent years.

In this study, we focus mainly on SEIRA spectroscopy with both photons and its analog with electron probes. We introduce their theoretical description of these techniques, involving both numerical and analytical modeling. The proper description of the underlying physical mechanisms behind resonant SEIRA is one of the most important aspects that need to be resolved. The theoretical description could result in designing experiments in a way for optimal enhanced spectroscopy performance.

Some works proposed that the response could be intuitively understood in the means of coupled harmonic oscillators [8] or by the model of coupled dipoles [9, 10]. We continue in work published in a recent article [11], where the enhancement of the signal was discussed in terms of interference.

In Chapter 1, we review the theoretical foundations, mainly the important concepts of electrodynamics and material response. We elaborate on the electromagnetic scattering of a simplified system represented by a point-like oscillating dipole, which will be later used to represent both the molecular sample and a finite-size nano-antenna [(A) in Fig. 1].

In Chapter 2 we first consider the interaction of a point dipole with the field of a nearby second dipole, which results in the coupling of the dipoles. The second dipole can represent, for example, a molecular sample positioned in the vicinity of the nano-antenna [(S) in Fig. 1]. With this formalism, we will model the interaction of an antenna-molecule system considered in the enhanced spectroscopies. Then, we consider illumination and

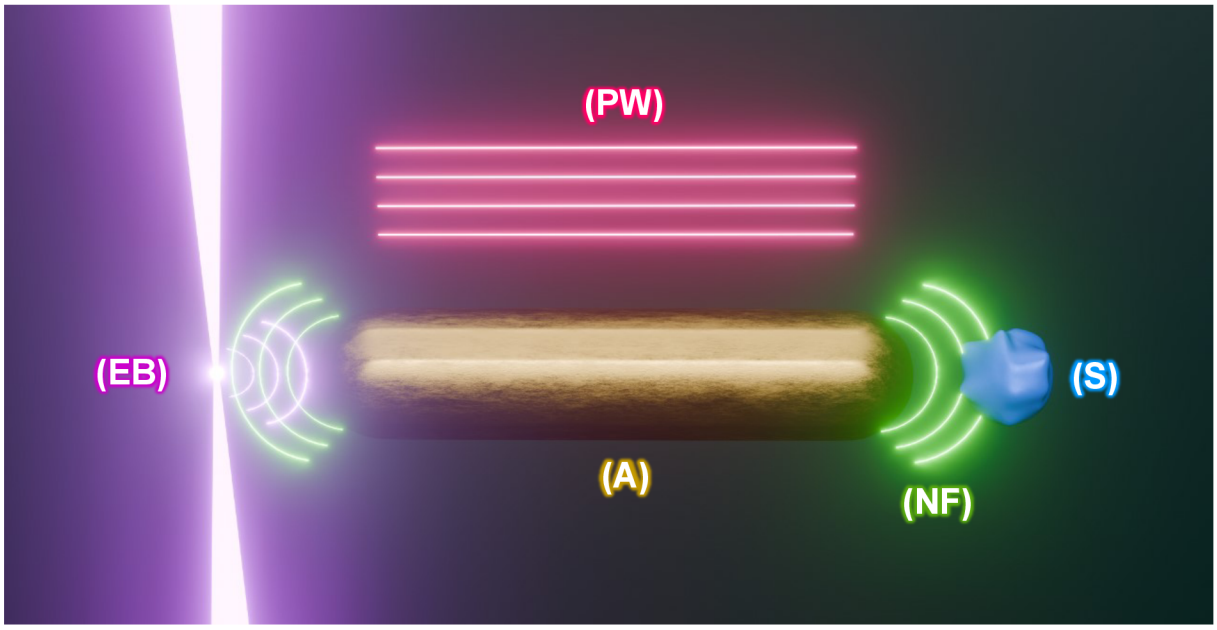

Figure 1: Scheme of an enhanced spectroscopy experiment. The system with which we will deal in the thesis consists of a nano-antenna (A) and a molecular sample (S). The external source of the electric field resulting in excitation of the system could either be a plane wave illumination tuned in frequency to the antenna resonance (PW) or the field of a swift electron beam (EB). The near-field interaction between the antenna and molecular sample (NF) results in the enhancement of the spectroscopic signal of the molecules.

subsequent inducement of the point dipole by a plane electromagnetic wave [(PW) in Fig. 1]. We introduce the concept of optical cross sections and show how they could be calculated numerically. Lastly, we consider the inelastic interaction of nanostructures with a fast electron beam [(EB) in Fig. 1], which represents a localized probe of the electric field.

In Chapter 3, we review vibrational spectroscopy and put the main focus on enhanced spectroscopy with photons and electrons. We follow up with Chapter 4, where we describe the near-field interaction of the antenna and molecular sample [(NF) in Fig. 1], resulting in the enhanced molecular signal. We describe the mechanism behind resonant SEIRA by using an approximation analytical model of multiple scattering processes between the nano-antenna and the sample. We consider both the case of probing the system with photons and with electrons. Lastly, we establish figures of merit (FOM) based on the analytical model. With the FOMs we can evaluate the performance of antennas of different shapes or materials in experiments where we study either the power lost during the interaction (transmission experiments or EELS) or the radiated power (scattering experiments).

1 Electromagnetic scattering

For aeons past, humanity was constantly interested in the nature of light and the possibilities of utilizing it in its favor. In this chapter, we present a brief overview of electrodynamics, introduce Green's function as a tool for solving differential equations, which will be utilized to solve scattering problems, and also introduce the formalism of electromagnetically interacting point dipoles. Lastly, we describe models of material response to the external electric field and introduce the concept of nano-antenna. The main sources are Refs. [12, 13], the reader may find deeper views into this topic in, for example, Refs. [14, 15].

1.1 Electrodynamics

In this section, we first introduce Maxwell's equations and constitutive relations accounting for the influence of the matter. Then we introduce the equations for the electromagnetic potentials.

1.1.1 Maxwell's equations and constitutive relations

Maxwell's equations are the cornerstone of electrodynamics. The sources, sinks, and temporal and spatial evolution of electromagnetic fields are contained in these equations. Even though the theory of electrodynamics, as published by Maxwell, is over 160 years old now, is still used for the description of countless electrodynamic phenomena. It can be used for the classical description of electromagnetic problems or implemented into newly emerging fields such as nanophotonics describing the behavior of electromagnetic fields at the nanoscale. The form in which we know Maxwell's equations nowadays was simplified from the original Maxwell's manuscript by Oliver Heaviside to the following form using the formalism of vector calculus

$$\nabla \cdot \mathbf{D}(\mathbf{r},t) = \rho_{\mathrm{f}}(\mathbf{r},t), \tag{1.1}$$

$$\nabla \cdot \mathbf{B}(\mathbf{r},t) = 0, \tag{1.2}$$

$$\nabla \times \mathbf{E}(\mathbf{r},t) = -\frac{\partial \mathbf{B}(\mathbf{r},t)}{\partial t}, \tag{1.3}$$

$$\nabla \times \mathbf{H}(\mathbf{r},t) = \mathbf{J}_{\mathrm{f}}(\mathbf{r},t) + \frac{\partial \mathbf{D}(\mathbf{r},t)}{\partial t}, \tag{1.4}$$

where $\mathbf{D}$ is the dielectric displacement field, $\mathbf{B}$ is the magnetic induction, $\mathbf{E}$ is the electric field, $\mathbf{H}$ is the magnetic field, $\mathbf{J}_{\mathrm{f}}$ is the free current density and ρ_{f} is the free charge density. The dielectric displacement can be expressed in terms of the electric field and the macroscopic polarization field

$$\mathbf{D}(\mathbf{r},t) = \varepsilon_0 \mathbf{E}(\mathbf{r},t) + \mathbf{P}(\mathbf{r},t), \tag{1.5}$$

where ε_0 is the vacuum permittivity. The polarization field $\mathbf{P}$ represents the density of electric dipole moments as $\mathbf{P}(\mathbf{r},t) = n_{\mathrm{e}}\mathbf{p}$, where n_{e} is the density of the electric dipoles

and $\mathbf{p}$ is the electric dipole moment. The magnetic induction and the macroscopic magnetization field contribute to the magnetic field as

$$\mathbf{H}(\mathbf{r},t) = \frac{1}{\mu_0}\mathbf{B}(\mathbf{r},t) - \mathbf{M}(\mathbf{r},t), \tag{1.6}$$

where μ_0 is the vacuum permeability. Similarly to the polarization field, we introduced the magnetization field as $\mathbf{M}(\mathbf{r},t) = n_\mathrm{m}\mathbf{m}$, with the density of the magnetic dipoles n_m and the magnetic dipole moment $\mathbf{m}$. With ε_0 and μ_0 we can define the speed of light as $c^2 = 1/(\varepsilon_0\mu_0)$.

We now plug the relations for $\mathbf{D}$ and $\mathbf{H}$ back into Eqs. (1.1) and (1.4), respectively, to obtain

$$\nabla \cdot \mathbf{E}(\mathbf{r},t) = \frac{\rho(\mathbf{r},t)}{\varepsilon_0}, \tag{1.7}$$

$$\nabla \times \mathbf{B}(\mathbf{r},t) = \mu_0\mathbf{J}(\mathbf{r},t) + \mu_0\varepsilon_0\frac{\partial\mathbf{E}(\mathbf{r},t)}{\partial t}, \tag{1.8}$$

where we defined the total charge density (ρ) and the total current density (J). The total charge and current densities consist of the contribution from the free charge and current densities, which can be adjusted externally, and the bound current and charge densities $\mathbf{J}_\mathrm{b}$ and ρ_b, respectively, emerging due to the polarization and magnetization of the matter.

$$\rho = \rho_\mathrm{f} + \rho_\mathrm{b} = \rho_\mathrm{f} - \nabla \cdot \mathbf{P}, \tag{1.9}$$

$$\mathbf{J} = \mathbf{J}_\mathrm{f} + \mathbf{J}_\mathrm{b} = \mathbf{J}_\mathrm{f} + \nabla \times \mathbf{M} + \frac{\partial\mathbf{P}}{\partial t}. \tag{1.10}$$

When considering the response of the matter to the electromagnetic fields, one must be cautious about the spatial and temporal non-locality of the response. It turns out to be convenient to express the so-called constitutive relations between the fields $\mathbf{D}$ and $\mathbf{H}$, which are dependent on the material response to the electric field $\mathbf{E}$ and magnetic induction $\mathbf{B}$, respectively, in the Fourier space as shown in Appendix A[1]. In so-called linear and translationally invariant media, the constitutive relations are linear. When considering non-linear media, higher-order terms would have to be considered in the relations. We express the constitutive as

$$\mathcal{D}(\mathbf{k},\omega) = \varepsilon_0\varepsilon_\mathrm{r}(\mathbf{k},\omega)\mathcal{E}(\mathbf{k},\omega), \tag{1.11}$$

$$\mathcal{H}(\mathbf{k},\omega) = \mu_0\mu_\mathrm{r}(\mathbf{k},\omega)\mathcal{B}(\mathbf{k},\omega), \tag{1.12}$$

where $\mathbf{k}$ is the angular wavevector, ω is the angular frequency, and the linear coefficients between the fields are the dielectric function ε_r and the relative permeability μ_r. An electromagnetic field in a linear medium can be expressed as a superposition of monochromatic fields that are called plane waves. We now consider just one sinusoidal plane wave

$$\mathbf{E}(\mathbf{r},t) = \frac{1}{2}\left[\mathcal{E}\mathrm{e}^{\mathrm{i}(\mathbf{k}\cdot\mathbf{r}-\omega t)} + \mathrm{c.c.}\right], \tag{1.13}$$

$$\mathbf{B}(\mathbf{r},t) = \frac{1}{2}\left[\mathcal{B}\mathrm{e}^{\mathrm{i}(\mathbf{k}\cdot\mathbf{r}-\omega t)} + \mathrm{c.c.}\right], \tag{1.14}$$

[1]For the Fourier transform, we use the notation $\mathcal{D}(\mathbf{k},\omega) = \mathrm{FT}\{\mathbf{D}(\mathbf{r},t)\}, \mathcal{E}(\mathbf{k},\omega) = \mathrm{FT}\{\mathbf{E}(\mathbf{r},t)\}, \mathcal{H}(\mathbf{k},\omega) = \mathrm{FT}\{\mathbf{H}(\mathbf{r},t)\}$, and $\mathcal{B}(\mathbf{k},\omega) = \mathrm{FT}\{\mathbf{B}(\mathbf{r},t)\}$.

where the electromagnetic fields have to be real, so we added the complex conjugate (c.c). Equivalently, we can write $\mathbf{E}(\mathbf{r},t) = \mathrm{Re}\left\{\mathcal{E}\mathrm{e}^{\mathrm{i}(\mathbf{k}\cdot\mathbf{r}-\omega t)}\right\}$.

One of the major results of the electromagnetic theory was the ascertainment that the electromagnetic fields carry energy. We now derive the equation for the conservation of electromagnetic energy. For clarity, we drop the spatial and temporal dependencies in parentheses. We start by applying the dot products $\mathbf{E}\cdot$ to Eq. (1.3) and $\mathbf{B}\cdot$ to Eq. (1.8). After subtracting these two equations and rearranging them, we obtain

$$\mathbf{B}\cdot(\nabla\times\mathbf{E}) - \mathbf{E}(\nabla\times\mathbf{B}) + \mathbf{B}\cdot\frac{\partial\mathbf{B}}{\partial t} + \varepsilon_0\mu_0\mathbf{E}\cdot\frac{\partial\mathbf{E}}{\partial t} = -\mu_0\mathbf{J}\cdot\mathbf{E}. \tag{1.15}$$

After using the vector identity $\nabla\cdot(\mathbf{u}\times\mathbf{v}) = \mathbf{v}\cdot(\nabla\times\mathbf{u}) - \mathbf{u}(\nabla\times\mathbf{v})$, expressing the dot product of vector and its derivative as $\mathbf{u}\cdot\frac{\partial}{\partial t}\mathbf{u} = \frac{1}{2}\frac{\partial}{\partial t}|\mathbf{u}|^2$, multiplying both sides of the equation by $1/\mu_0$, and rearranging the terms, we reach the following form

$$\nabla\cdot\left(\frac{1}{\mu_0}\mathbf{E}\times\mathbf{B}\right) = -\mathbf{J}\cdot\mathbf{E} - \frac{\partial}{\partial t}\frac{1}{2}\left(\varepsilon_0|\mathbf{E}|^2 + \frac{1}{\mu_0}|\mathbf{B}|^2\right). \tag{1.16}$$

We now integrate this equation over a volume Ω and apply the divergence theorem for the first term, where we interchange the volume integration of divergence of the vector to the integration over the closed boundary of the volume $\partial\Omega$ and get

$$\oiint_{\partial\Omega}\underbrace{\left(\frac{1}{\mu_0}\mathbf{E}\times\mathbf{B}\right)}_{\mathbf{S}}\cdot\hat{\mathbf{r}}\,\mathrm{d}\Omega = -\underbrace{\int_\Omega\mathbf{J}\cdot\mathbf{E}\,\mathrm{d}^3\mathbf{r}}_{\text{Dissipation}} - \frac{\partial}{\partial t}\int_\Omega\underbrace{\frac{1}{2}\left(\varepsilon_0|\mathbf{E}|^2 + \frac{1}{\mu_0}|\mathbf{B}|^2\right)}_{w}\mathrm{d}^3\mathbf{r}, \tag{1.17}$$

where $\mathrm{d}\Omega$ is a infinitesimal surface element and $\hat{\mathbf{r}}$ is a vector perpendicular to it. This identity tells us that the energy of the electromagnetic waves is conserved and is interpreted by Poynting's theorem. It states that the term on the left side of the equation describes the energy flowing inside or outside the volume, and we denoted it as the Poynting vector $\mathbf{S}$, which has the meaning of the energy flow density. The first term on the right side accounts for the dissipation losses by the heating of the material. The second term expresses the temporal change in the energy of the electromagnetic field, where we denoted the electromagnetic energy density as w.

In many cases, we are interested in a time average of the energy flow. We again consider plane electromagnetic wave, e.g. the fields are time-harmonic $\mathbf{E}(\mathbf{r},t) = \mathrm{Re}\left\{\mathbf{E}_\mathrm{r}(\mathbf{r})\mathrm{e}^{-\mathrm{i}\omega t}\right\}$ and $\mathbf{B}(\mathbf{r},t) = \mathrm{Re}\left\{\mathbf{B}_\mathrm{r}(\mathbf{r})\mathrm{e}^{-\mathrm{i}\omega t}\right\}$. The time-averaged Poynting vector then reads[2]

$$\langle\mathbf{S}_\mathrm{r}(\mathbf{r})\rangle = \frac{1}{2}\mathrm{Re}\left\{\frac{1}{\mu_0}\mathbf{E}_\mathrm{r}(\mathbf{r})\times\mathbf{B}_\mathrm{r}^*(\mathbf{r})\right\}. \tag{1.18}$$

With the help of Eq. (A.8), $\langle\mathbf{S}\rangle$ can be rewritten as

$$\langle\mathbf{S}_\mathrm{r}(\mathbf{r})\rangle = \frac{1}{2}\sqrt{\frac{\varepsilon_0}{\mu_0}}\left|\mathbf{E}_\mathrm{r}(\mathbf{r})\right|^2\hat{\mathbf{k}} = I_\mathrm{r}(\mathbf{r})\hat{\mathbf{k}}, \tag{1.19}$$

where $\hat{\mathbf{k}}$ is a unit vector in the direction of the wave propagation given by the wavevector $\mathbf{k}$, and we defined the intensity of the electromagnetic wave as $I_\mathrm{r}(\mathbf{r}) = \left|\langle\mathbf{S}_\mathrm{r}(\mathbf{r})\rangle\right|$.

[2]Time average of a product of two time-harmonic variables is usually defined as $\langle fg\rangle = 1/T\int_0^T(f\mathrm{e}^{-\mathrm{i}\omega t} + \mathrm{c.c.})\,(g\mathrm{e}^{-\mathrm{i}\omega t} + \mathrm{c.c.})\,\mathrm{d}t = 1/2\,\mathrm{Re}\{fg^*\}$. where $T = 2\pi/\omega$ is the period of the oscillation

1.1.2 Electromagnetic potentials

Important quantities, which can be useful in the description and computation of electromagnetic fields are the vector and scalar potentials. We may relate $\mathbf{B}$ to the vector potential

$$\mathbf{B}(\mathbf{r},t) = \nabla \times \mathbf{A}(\mathbf{r},t), \tag{1.20}$$

so that Eq. (1.2) is automatically fulfilled. By plugging this expression for magnetic induction into Eq. (1.3), and assuming that the spatial and temporal derivatives are interchangeable we get

$$\nabla \times \mathbf{E}(\mathbf{r},t) + \frac{\partial}{\partial t}\big(\nabla \times \mathbf{A}(\mathbf{r},t)\big) = \nabla \times \left(\mathbf{E}(\mathbf{r},t) + \frac{\partial \mathbf{A}(\mathbf{r},t)}{\partial t}\right) = \mathbf{0}. \tag{1.21}$$

We can attribute the term in parentheses to a divergence of some scalar field V, as the curl of divergence equals zero. We will call this newly defined quantity the scalar electrostatic potential. If we express the electric field in terms of the potentials we get

$$\mathbf{E}(\mathbf{r},t) = -\frac{\partial \mathbf{A}(\mathbf{r},t)}{\partial t} - \nabla V(\mathbf{r},t). \tag{1.22}$$

The minus sign before the electrostatic potential gradient V is convention having roots in the charge performing work against the field $\mathbf{E}$.

When dealing with electromagnetic potentials, the so-called Lorenz gauge comes in handy, notably when one wants to derive the wave equations for potentials. The gauge condition is in the form

$$\nabla \cdot \mathbf{A}(\mathbf{r},t) + \varepsilon_0 \mu_0 \frac{\partial V(\mathbf{r},t)}{\partial t} = 0, \tag{1.23}$$

and it will be used in the following section for the derivation of Green's function of the wave equation.

1.2 Dyadic Green's function

Green's function is a powerful tool for solving differential equations and many love it for its elegance. To introduce the concept of Green's function and its relation to the solutions of electromagnetic fields, we refer the reader to Appendix B. In this section, we derive the dyadic Green's function for the wave equation in the vacuum. The wave equation is very important because various physical phenomena can be described in terms of waves. The definition of the wave, as the solution of the wave equation, is intrinsically linked to it. For this part, we will consider time-harmonic fields $\mathbf{E}(\mathbf{r},t) = \mathrm{Re}\left\{\mathbf{E}_\mathrm{r}(\mathbf{r})\mathrm{e}^{-\mathrm{i}\omega t}\right\}$ and the current density $\mathbf{J}(\mathbf{r},t) = \mathrm{Re}\left\{\mathbf{J}_\mathrm{r}(\mathbf{r})\mathrm{e}^{-\mathrm{i}\omega t}\right\}$. If we apply the curl $\nabla\times$ to Eq. (1.3), interchange the spatial and temporal derivatives, and express the $\nabla \times \mathbf{B}$ with Eq. (1.8), we get inhomogeneous wave equation for the electric field in the form

$$-\nabla \times \nabla \times \mathbf{E}_\mathrm{r}(\mathbf{r}) + k^2 \mathbf{E}_\mathrm{r}(\mathbf{r}) = -\mathrm{i}\mu_0 \omega \mathbf{J}_\mathrm{r}(\mathbf{r}), \tag{1.24}$$

where we defined the free-space wavenumber k as $k = \omega/c$. The wavenumber is connected to the wavelength of the wave λ as $k = 2\pi/\lambda$. We now describe the electric field in form of

vector and scalar potentials and suppose the time harmonicity $\mathbf{A}(\mathbf{r},t) = \mathrm{Re}\left\{\mathbf{A}_\mathrm{r}(\mathbf{r})\mathrm{e}^{-\mathrm{i}\omega t}\right\}$ and $V(\mathbf{r},t) = \mathrm{Re}\left\{V_\mathrm{r}(\mathbf{r})\mathrm{e}^{-\mathrm{i}\omega t}\right\}$. The relation (1.22) will then take the subsequent form

$$\mathbf{E}_\mathrm{r}(\mathbf{r}) = \mathrm{i}\omega\mathbf{A}_\mathrm{r}(\mathbf{r}) - \nabla V_\mathrm{r}(\mathbf{r}). \tag{1.25}$$

By inserting this expression for the electric field back into the inhomogeneous wave equation (1.24) and by applying the Lorenz gauge (1.23), we get the wave equation for the vector potential

$$\nabla^2\mathbf{A}_\mathrm{r}(\mathbf{r}) + k^2\mathbf{A}_\mathrm{r}(\mathbf{r}) = -\mu_0\mathbf{J}_\mathrm{r}(\mathbf{r}), \tag{1.26}$$

which is in the form of the Helmholtz Eq. (B.5), and its solution can be written with the help of Green's function (B.3) as

$$\mathbf{A}_\mathrm{r}(\mathbf{r}) = \mu_0 \int G(\mathbf{r},\mathbf{r}')\mathbf{J}_\mathrm{r}(\mathbf{r}')\,\mathrm{d}^3\mathbf{r}'. \tag{1.27}$$

Again, by applying the Lorenz gauge, we get the equation for the scalar potential

$$V_\mathrm{r}(\mathbf{r}) = -\frac{\mathrm{i}\omega\mu_0}{k^2}\nabla\cdot\int G(\mathbf{r},\mathbf{r}')\mathbf{J}_\mathrm{r}(\mathbf{r}')\,\mathrm{d}^3\mathbf{r}'. \tag{1.28}$$

If we now insert the obtained relations for vector and scalar potentials back into Eq. (1.25) we get

$$\mathbf{E}_\mathrm{r}(\mathbf{r}) = \mathrm{i}\omega\mu_0\int\left(\overleftrightarrow{\mathbf{I}} + \frac{1}{k^2}\nabla\nabla\right)G(\mathbf{r},\mathbf{r}')\cdot\mathbf{J}_\mathrm{r}(\mathbf{r}')\,\mathrm{d}^3\mathbf{r}' = \mathrm{i}\omega\mu_0\int\overleftrightarrow{\mathbf{G}}(\mathbf{r},\mathbf{r}')\cdot\mathbf{J}_\mathrm{r}(\mathbf{r}')\,\mathrm{d}^3\mathbf{r}', \tag{1.29}$$

where $\overleftrightarrow{\mathbf{I}}$ is the unit dyad, and we defined the dyadic Green's dyadic function

$$\overleftrightarrow{\mathbf{G}} = \left(\overleftrightarrow{\mathbf{I}} + \frac{1}{k^2}\nabla\nabla\right)\frac{\mathrm{e}^{\mathrm{i}kR}}{4\pi R}, \tag{1.30}$$

where $R = \left|\mathbf{r}-\mathbf{r}'\right|$ is the magnitude of the vector $\mathbf{R} = \mathbf{r}-\mathbf{r}'$. After rewriting the dyadic Green's function into components, it can be seen that it is a symmetric dyad, in this case, $\overleftrightarrow{\mathbf{G}} = \overleftrightarrow{\mathbf{G}}^\mathrm{T}$, where $(\cdot)^\mathrm{T}$ means transposition.

It can be helpful to express the Green's dyadic in the Cartesian coordinates as [13]

$$\overleftrightarrow{\mathbf{G}} = \left[\left(1 + \frac{\mathrm{i}kR-1}{k^2R^2}\right)\overleftrightarrow{\mathbf{I}} + \frac{3-3\mathrm{i}kR-k^2R^2}{k^2R^2}\frac{\mathbf{R}\otimes\mathbf{R}}{R^2}\right]\frac{\mathrm{e}^{\mathrm{i}kR}}{4\pi R}. \tag{1.31}$$

Depending on the distance R, we can split the Green's dyadic in Cartesian coordinates into different terms. In the regime where the wavelength of the wave λ is much larger than the considered distances $\lambda >> R$, the part dependent on $(kR)^{-3}$ prevails. We label this region in the vicinity of the origin as the near field (NF). The near-field part of Green's dyadic then reads

$$\overleftrightarrow{\mathbf{G}}_\mathrm{NF} = \left[-\overleftrightarrow{\mathbf{I}} + 3\frac{\mathbf{R}\otimes\mathbf{R}}{R^2}\right]\frac{1}{k^2R^2}\frac{\mathrm{e}^{\mathrm{i}kR}}{4\pi R}. \tag{1.32}$$

If we think about very large distances from the origin, the major contribution is from the part of Green's dyadic, which is dependent on $(kR)^{-1}$. We label this distant region as the far field (FF), where $\lambda << R$. The far-field component of the Green's dyadic can be expressed as

$$\overleftrightarrow{\mathbf{G}}_\mathrm{FF} = \left[\overleftrightarrow{\mathbf{I}} - \frac{\mathbf{R}\otimes\mathbf{R}}{R^2}\right]\frac{\mathrm{e}^{\mathrm{i}kR}}{4\pi R}. \tag{1.33}$$

1.3 Dipole radiation

In Section 1.1, we introduced the macroscopic (averaged) description of polarized or magnetized matter with the help of the polarization and magnetization fields. We now move to the microscopic description, where we consider a system consisting of point charges randomly distributed in the matter. We can consider $\mathbf{E}$ and $\mathbf{B}$ emerging between the point charges, but from now on we won't assume magnetic fields. Such a system is schematically shown in Fig. 1.1 (a). The current density created by a system of point-like moving charges labeled q_n can be written as

$$\mathbf{J}(\mathbf{r},t) = \sum_n q_n \frac{\mathrm{d}\mathbf{r}_n(t)}{\mathrm{d}t}\delta(\mathbf{r}-\mathbf{r}_n), \tag{1.34}$$

where $\mathbf{r}_n$ is the position vector of the charge q_n. By developing the current density into the Taylor series with origin $\mathbf{r}_0$, which is usually considered to be in the center of the charge distribution, and keeping only the first term of the series, we get

$$\mathbf{J}(\mathbf{r},t) = \frac{\mathrm{d}\mathbf{p}(\mathbf{r},t)}{\mathrm{d}t}\delta(\mathbf{r}-\mathbf{r}_0). \tag{1.35}$$

With this, we approximated the response of the matter to the response of a point dipole located in its center. If we now assume time harmonicity of the current density $\mathbf{J}(\mathbf{r},t) = \mathrm{Re}\{\mathbf{J}_\mathrm{r}(\mathbf{r})\mathrm{e}^{-\mathrm{i}\omega t}\}$ and the dipole moment $\mathbf{p}(\mathbf{r},t) = \mathrm{Re}\{\mathbf{p}_\mathrm{r}(\mathbf{r})\mathrm{e}^{-\mathrm{i}\omega t}\}$, we can write $\mathbf{J}_\mathrm{r}(\mathbf{r}) = -\mathrm{i}\omega\mathbf{p}_\mathrm{r}(\mathbf{r})\delta(\mathbf{r}-\mathbf{r}_0)$. After inserting this current in Eq. (1.29), we get

$$\mathbf{E}_\mathrm{r}(\mathbf{r}) = \omega^2\mu_0 \overleftrightarrow{\mathbf{G}}(\mathbf{r},\mathbf{r}_0)\cdot\mathbf{p}_\mathrm{r}(\mathbf{r}_0). \tag{1.36}$$

We next assume linear dependency between the induced dipole model and the electric field driving the dipole mediated by a diagonal polarizability tensor $\overleftrightarrow{\boldsymbol{\alpha}}$ with components α_{ii} where $i = x, y, z$ as

$$\mathbf{p}_\mathrm{r}(\mathbf{r}) = \overleftrightarrow{\boldsymbol{\alpha}}\cdot\mathbf{E}_\mathrm{r}(\mathbf{r}). \tag{1.37}$$

The polarizability accounts for the material properties and the geometry of the structure and in this thesis we will always assume that the tensor is diagonal.

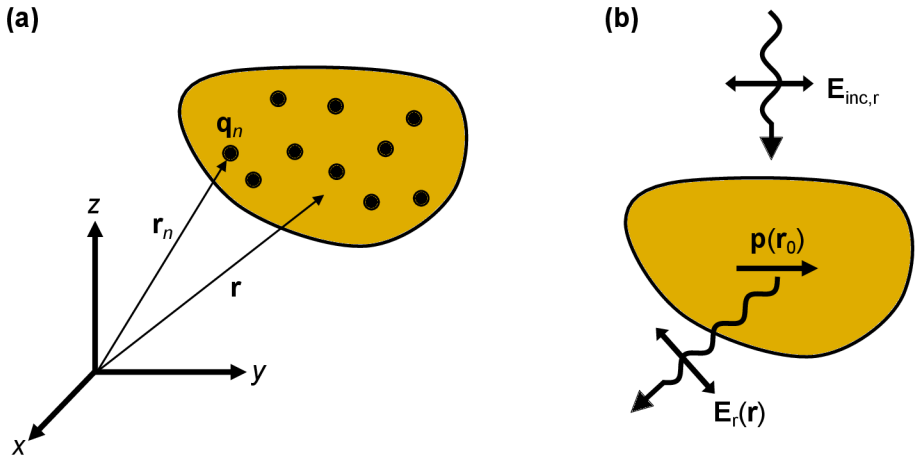

Figure 1.1: (a) Scheme of n discrete charges forming a medium. (b) Scattering of the incoming light from the medium, which is approximated by a point dipole in the center.

By expressing the dipole in terms of the polarizability, we can write

$$\mathbf{E}_{\mathrm{r}}(\mathbf{r}) = \frac{k^2}{\varepsilon_0} \overleftrightarrow{\mathbf{G}}(\mathbf{r}, \mathbf{r}_0) \cdot \overleftrightarrow{\boldsymbol{\alpha}} \cdot \mathbf{E}_{\mathrm{inc,r}}(\mathbf{r}_0), \tag{1.38}$$

we can see that the electric field of a dipole located at the position $\mathbf{r}_0$ is fully described by the Green's dyadic. We now introduce the field enhancement tensor as

$$\overleftrightarrow{\boldsymbol{f}} = \frac{k^2}{\varepsilon_0} \overleftrightarrow{\mathbf{G}}(\mathbf{r}, \mathbf{r}_0) \cdot \overleftrightarrow{\boldsymbol{\alpha}}. \tag{1.39}$$

The field enhancement describes how large (or small, depending on the distance from the dipole) is the electric field in the vicinity of the dipole compared to the incoming field.

In the following sections, we will use this approach to approximate the field radiated from the nanostructure by a point dipole, described by the polarizability tensor $\overleftrightarrow{\boldsymbol{\alpha}}$ driven by the incoming field $\mathbf{E}_{\mathrm{inc,r}}$. The situation is schematically sketched in Fig. 1.1 (b). The incoming field can be a propagating electromagnetic wave, an evanescent electromagnetic field (for example of a nanostructure or of a focused electron beam), or even a second dipole. We describe the driving of an electric dipole by different external fields and its subsequent radiation in Chapter 2.

1.4 Material response

To model the material response to the external electric field, we assume that the material consists of discrete charges, which under the influence of the field form electric dipoles. The dipole can be thought of as a positive charge and a negative charge connected by a bond. When the external field is dynamic, this dipole oscillates and it can be modeled via a harmonic oscillator model. We assume that the movement of the positive charge (i.e. heavy positive ion) can be neglected, and the negative charge (i.e. electron or a positive ion) oscillates on the spring representing the bond. We can see the scheme of this approximative model in Fig. 1.2 (a). We consider force proportional to the strength of the bond $\mathbf{F}_{\mathrm{bond}}$, which acts oppositely to the oscillator displacement, the damping force $\mathbf{F}_{\mathrm{damp}}$, proportional to the electron's velocity, and the driving external force $\mathbf{F}_{\mathrm{drive}}$, represented by the external electric field. We can then write the equation of motion as

$$m\ddot{\mathbf{r}} = \underbrace{-k\mathbf{r}}_{\mathbf{F}_{\mathrm{bond}}} \underbrace{-m\gamma\dot{\mathbf{r}}}_{\mathbf{F}_{\mathrm{damp}}} \underbrace{-e\mathbf{E}(\mathbf{r}, t)}_{\mathbf{F}_{\mathrm{drive}}}, \tag{1.40}$$

where $\mathbf{r}$ is the displacement of the oscillator from equilibrium, m is the oscillator mass, k is a constant that depends on the strength of the bond, e is the elementary charge, and γ is the damping parameter. The resonant frequency of the oscillator can be described by its properties as $\omega_0 = \sqrt{k/m}$. If we assume time harmonic external field $\mathbf{E}(\mathbf{r}, t) = \mathrm{Re}\left\{\mathbf{E}_{\mathrm{r}}(\mathbf{r})\mathrm{e}^{-\mathrm{i}\omega t}\right\}$ the displacement in the steady state is

$$\mathbf{r} = \frac{-e}{m(\omega_0^2 - \omega^2 - \mathrm{i}\gamma\omega)} \mathbf{E}_{\mathrm{r}}(\mathbf{r}). \tag{1.41}$$

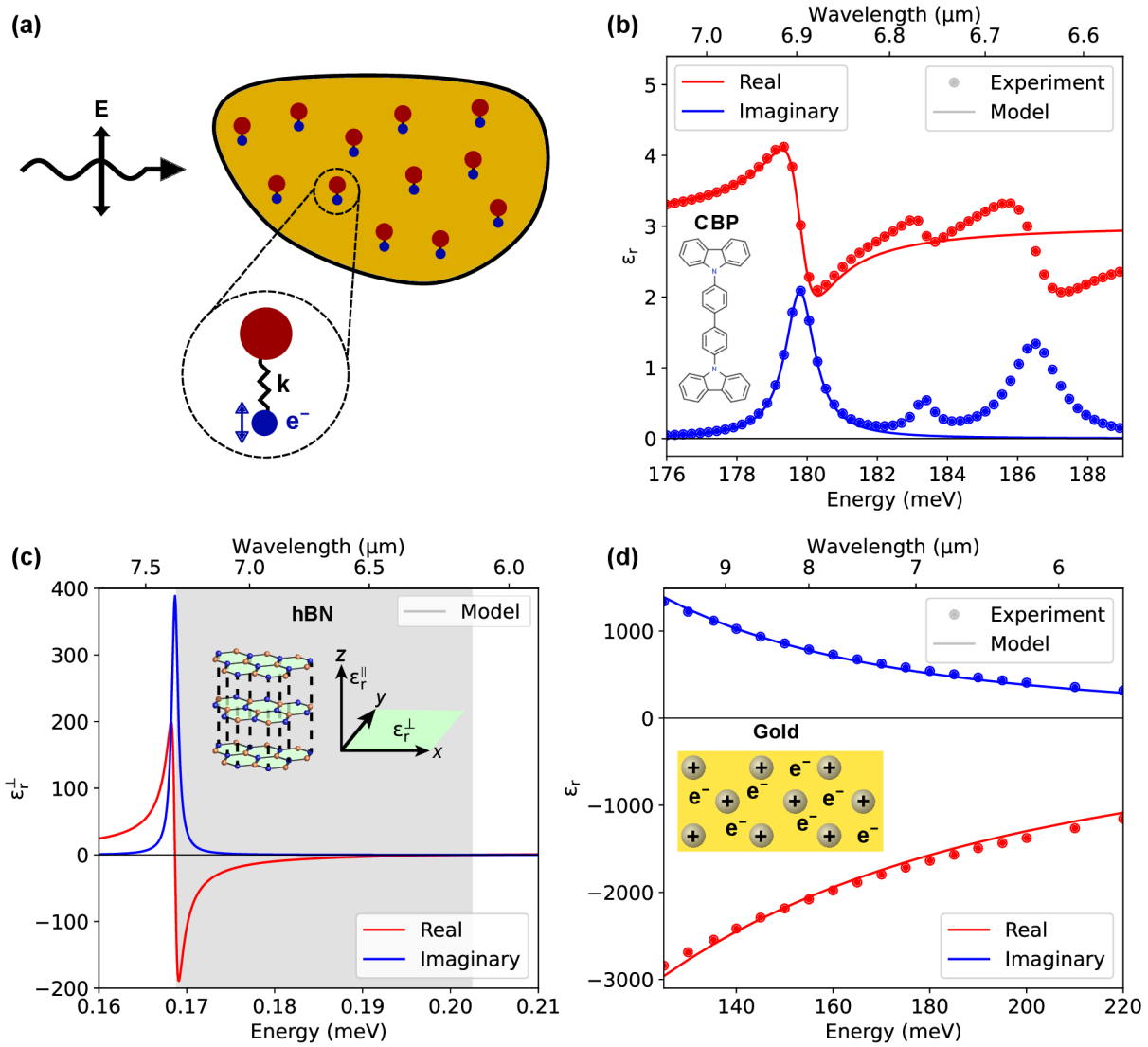

Figure 1.2: (a) Schematic sketch of a structure consisting of discrete electric dipoles induced by an external electric field. The response can be modeled with a harmonic oscillator model, where we assume negative charges, bound to stationary nuclei oscillate. (b) Dielectric function of a CBP molecule (shown in the inset, which is taken from [16]). With the dots, we plot experimentally measured dielectric function taken from Ref. [17]. We can recognize three vibrational resonances at approximately 179.5, 183.5, and 187 meV. With the full line, we plot the fit of the Lorentz model (1.44). We assume one oscillator with parameters $\varepsilon_\infty = 3.05$, $F_1 = 382.683\,\mathrm{meV}^2$, $\omega_{0,1} = 179.777\,\mathrm{meV}$ and $\gamma_1 = 1.029\,\mathrm{meV}$. We can see that the real part is always positive, thus yielding weak oscillator behavior. (c) Dielectric function in the upper Reststrahlen band of hBN $\varepsilon_\perp$. We again use the Lorentz model with the parameters $\varepsilon_\infty = 4.52$, $F_1 = 56\,910.331\,\mathrm{meV}^2$, $\omega_{0,1} = 168.634\,\mathrm{meV}$ and $\gamma_1 = 0.868\,\mathrm{meV}$. The transverse optical phonon is situated at around 168 meV, and the real part of the dielectric function is negative from this point until approximately 202 meV (gray area), thus exhibiting strong oscillator behavior. In the inset (taken from [18]) we plot the structure of a hBN crystal and the in-plane schematic. (d) Dielectric function of gold. Dots represent experimental data for gold by Palik [19], extracted from FDTD. With the full line, we plot the fit of the data with the Drude model from Eq. (1.45). The parameters are $\varepsilon_\infty = 3.931$, $\omega_\mathrm{p} = 7517\,\mathrm{meV}$ and $\gamma = 59\,\mathrm{meV}$.

We can assume that the system has an induced electric dipole moment $\mathbf{p}$, because of the charge displacement

$$\mathbf{p}_\mathrm{r}(\mathbf{r}) = -e\mathbf{r}. \tag{1.42}$$

Thus with $\mathbf{p}_\mathrm{r}(\mathbf{r})$ we can express the polarization field $\mathbf{P}_\mathrm{r}(\mathbf{r})$ as the dipole moment density $\mathbf{P}_\mathrm{r}(\mathbf{r}) = n_\mathrm{e}\mathbf{p}_\mathrm{r}(\mathbf{r})$ and consider Eq. (1.11) to write the dielectric function as

$$\varepsilon_\mathrm{r}(\omega) = 1 + \frac{n_\mathrm{e}e^2}{m\varepsilon_0}\frac{1}{\omega_0^2 - \omega^2 - \mathrm{i}\gamma\omega}. \tag{1.43}$$

This model of dielectric function based on the harmonic oscillator is called the Lorentz model. It offers the description of several types of resonances in matter, most notably the vibrational and electronic. We can generalize the Lorentz model for the case of more oscillators, accounting for resonant contributions to the response at different frequencies and write

$$\varepsilon_\mathrm{r}(\omega) = \varepsilon_\infty + \sum_j \frac{F_j}{\omega_{0,\mathrm{j}}^2 - \omega^2 - \mathrm{i}\gamma_j\omega}, \tag{1.44}$$

where we introduced background permittivity $\varepsilon_\infty \equiv \varepsilon_\mathrm{r}(\omega \to \infty)$, accounting for the non-resonant contributions to the polarization [20], $\omega_{0,\mathrm{j}}$ is the resonance frequency and γ_j is the damping parameter of the j-th oscillator, which has the strength F_j. The oscillator strength conceals oscillator mass and the charge density and depending on its magnitude, two regimes of the oscillations emerge. When the real part of the dielectric function is always positive, the oscillator is denoted as weak. For example, it can be used to model response due to vibrations in molecular samples, as we can see in Fig. 1.2 (b). Here we plot the experimentally measured dielectric function of 4,4-bis(N-carbazolyl)-1,1-biphenyl (CBP) molecules [17]. We fit the data of the C-H bond stretching resonance at approximately 180 meV with the Lorentz model. For larger oscillator strengths, we get a strong oscillator regime, the real part of the dielectric function has a band where it is negative and is responsible for polaritonic behavior. If the light with frequency lying inside this band impinges on the material, it gets mostly reflected. We can see such a band in Fig. 1.2 (c) where we plot the dielectric function of hexagonal boron nitride (hBN). This material is part of the family of van der Waals materials, which are formed by two-dimensional atomic crystals, stacked on each other as shown in a scheme of the hBN layers in the inset of Fig. 1.2 (c). The individual layers are bound by the van der Waals interaction [21]. Hence, the materials exhibit strong anisotropy. The response of hBN is given by dielectric tensor $\overleftrightarrow{\boldsymbol{\varepsilon}} = (\varepsilon_\perp, \varepsilon_\perp, \varepsilon_\parallel)$, where we denote the parallel $\parallel$ and perpendicular $\perp$ components with respect to the anisotropy (optical) axis, in this case, the z-axis. In Fig. 1.2 (c), we plot $\varepsilon_\perp$ in the so-called upper Reststrahlen band.

A special form of the harmonic oscillator model expressed by Eq. (1.44) arises if we consider the response of free electrons, i.e. we assume no bonds between electrons and the positive ion cores. Therefore there are no restoring forces, the electrons move freely as the electron gas [see inset in Fig. 1.2 (d)], which results in $\omega_0 = 0$. This model is named the Drude model and reads

$$\varepsilon_\mathrm{r}(\omega) = \varepsilon_\infty - \frac{\omega_\mathrm{p}^2}{\omega^2 + \mathrm{i}\gamma\omega}, \tag{1.45}$$

where we again suppose the background permitivity ε_∞ and we have defined the bulk plasma frequency $\omega_\mathrm{p} = \sqrt{n_\mathrm{e} e^2 / m_\mathrm{e} \varepsilon_0}$, where n_e is the concentration of free electrons and m_e is the electron mass. Plasma frequency is the eigenfrequency of the longitudinal oscillations of the electron gas in matter. In the definition, m_e is the electron mass, and n_e is the electron density. We plot the experimentally obtained dielectric function of gold in Fig. 1.2 (d) and fit it with the Drude model.

1.5 Optical and infrared antennas

As the definition states, an optical antenna is a device designed to efficiently convert freely propagating optical radiation to localized energy, and vice versa [22]. While radio-frequency (RF) antennas are widely spread in today's communication, one of the main goals of nanophotonics and adjacent fields is to make use of optical analog to the RF antennas. Nano-antennas and other resonant nanostructures have the ability to squeeze incident light into the nanoscale, which offers a large variety of potential applications, such as photodetection [23], photovoltaics [24, 25], lasing [26], utilizing them as probes for nanoimaging or a single-photon sources [27]. Recently, the use of plasmonic nano-antennas in heat-assisted magnetic recording (HAMR) was proposed, where the design would be used in the next generation of hard disk drives [28, 29]. Another current use is in the field of biosensing, for example, pregnancy tests [30] or tests of SARS-CoV-2 based on plasmonic nanoparticles designed during recent COVID-19 pandemic [31, 32]. The enhanced spectroscopies such as plasmon-enhanced fluorescence, tip-enhanced and surface-enhanced Raman spectroscopy, and surface-enhanced infrared absorption spectroscopy make use, we will discuss the latter two in more detail in Chapter 3.

One of the main differences between optical and RF antennas is that the optical antenna dimensions are in a fraction of the optical wavelength (tens to hundreds of nanometers). The optical antennas are typically made of materials that can support different types of resonant excitations when exposed to an external electromagnetic field. Optical antennas mostly rely on the excitation of the localized surface plasmons, or Mie-type dielectric resonances. When considering the infrared region, metallic antennas can still support plasmonic resonances, but the dimensions of such infrared antennas need to be much larger than those of optical antennas. Another suitable candidate for infrared antennas[3] made of phononic materials, which have resonances in IR natively and which can support localized surface phonons. Now we describe the general properties of the optical and infrared antennas, which we will refer to as nano-antennas, even though, the infrared antennas could be of micrometer lengths.

One of the most important aspects of antennas are their resonant properties [34]. The traditional perfectly conductive metallic RF dipole antennas can be thought of as resonators supporting standing electromagnetic waves. We consider the simplest case of a half-wavelength antenna made of perfectly reflective metal and an incoming electromagnetic wave of resonant wavelength illuminating it. The electromagnetic field displaces the electrons in the antenna back and forth, while generating standing waves of free charges, the amplitude of the waves is maximized at the resonance. As the name states,

[3]For plural of the word *antenna*, there are two possibilities. Throughout this thesis, we use the form *antennas*, as we are dealing with nano-analogs to the electric RF aerials. The form *antennae* is typically associated with the protuberances on the heads of insects [33].

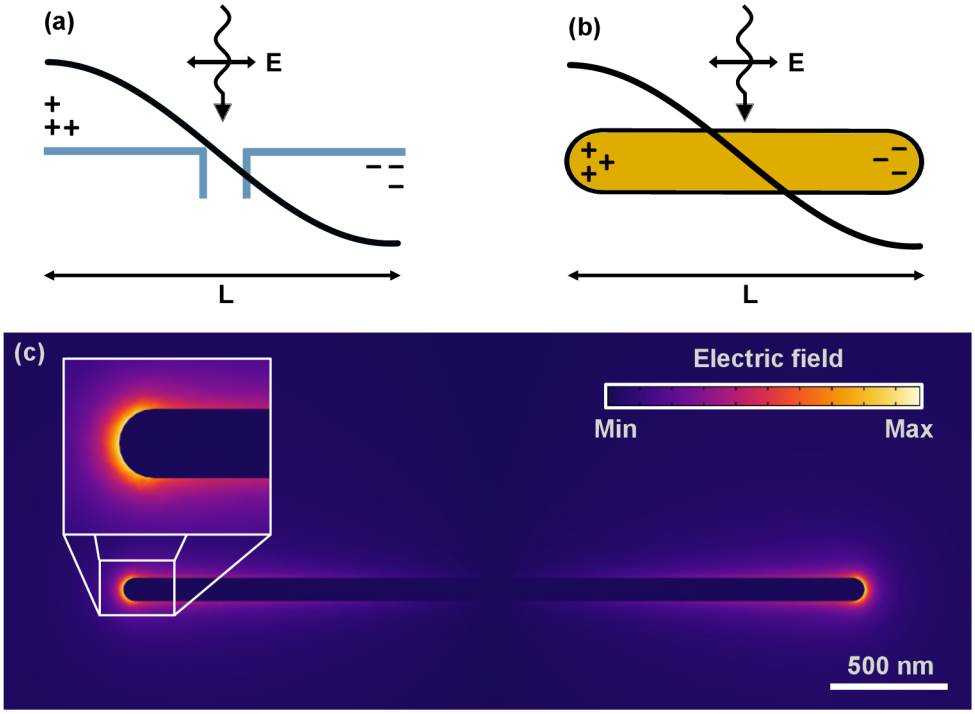

Figure 1.3: (a) Radio-frequency antenna (blue) consisting of two metallic wires. The incident electric field induces charge oscillations in the wires, schematically marked with positive and negative signs. The resonance frequency of the oscillations is linked to the antenna length L. (b) Metallic nanorod, acting as a nano-analog to the RF antenna. The incident electric field again induces charge oscillations, and the antenna supports localized plasmon polariton resonance. (c) Electric field magnitude around cylinder-shaped infrared antenna with round edges. The length L of the antenna is 3190 nm, and the diameter D is 100 nm. The antenna's material is defined by Palik's experimental data for gold [19]. The displayed field is induced after the excitation with a plane wave of energy 160 meV (wavelength 7750 nm) and calculated in COMSOL. We can see that the electric field is highly localized near the antenna tips and exponentially decays further on.

the antenna length is linked to the resonance wavelength as $\lambda = 2L$ [27]. We can see a scheme of dipolar resonance in an RF antenna in Fig. 1.3 (a). This simple formula can not be used for the nano-antennas, because the electromagnetic is not perfectly reflected from the metal, as in the case of RF antennas, but instead penetrates the material [34]. For the simplest case, we can consider rod-shaped nano-antenna shown schematically in Fig. 1.3 (b). The resonance wavelength of the nano-antenna λ_{res} can be written as [35]

$$\lambda_{\mathrm{res}} = \frac{2L}{m} n a_1 + a_2, \tag{1.46}$$

where L is the length of the antenna's long axis, in the direction where oscillations take place, n is the refractive index of the surrounding medium, a_1 is a parameter accounting for the antenna geometry and material, a_2 is a parameter accounting for the phase associated with reflections at the ends of the antenna and m is the order of mode. In comparison to the RF antennas, we also assume that the antenna can support higher order modes than just the dipole, for which $m = 1$. We can see dipolar resonance in nano-antenna in Fig. 1.3 (b). From Eq. (1.46), we can deduce that by elongating the antenna, the resonance

red-shifts to the lower energies. This aspect of antenna behavior is very important and will be exploited in the next sections to tailor nano-antennas to the desired resonance.

Another paramount aspect of nano-antenna is the enhancement of the electromagnetic fields. Numerical simulations [36, 37] can predict this enhancement and show that it could be in orders of tens to hundreds. This near-field is highly confined within the vicinity of the antenna sharpnesses, as is again shown by the numerical simulations and by near-field experiments [38]. When supposing rod-shaped nano-antenna, where the dipolar resonance is induced, the field is particularly intense near the sharp apexes, as shown in Fig. 1.3 (c), creating so-called hot-spots. In this thesis, we will not deal with higher-order modes, which can have hot-spots in other parts of the antenna. We can attribute the field enhancement to the induced charge density, displaced by the external electric field, which is the largest near the sharpnesses. On the other hand, we can look at the field enhancement in the context of the field scattered by an object described with Green's dyadic (1.36), and the field-enhancement tensor (1.39).

2 Point-dipole model of electromagnetic scattering

In this chapter, we describe the interaction of previously derived point dipole with external sources and show how we can describe the electric field scattered from the dipole. We consider interaction with a field of a second dipole, electromagnetic plane wave, and field of a beam of swift electrons. We complete the overview with results of numerical simulations for an interaction of nano-antennas with plane wave and electron beam and compare them to the analytically obtained results.

2.1 Interaction between two point dipoles

We now introduce the description of the interaction between two point dipoles. This theoretical model be used for describing a general system consisting of two entities with dipole moments, for example, it is used for modeling scattering-type scanning near-field optical microscopy (s-SNOM) experiments, with a tip probing a sample, each represented by one dipole [39, 40]. We will use the coupled dipoles formalism in the derivations of formulas for enhanced spectroscopies in Chapter 4, where we will study the system of a nano-antenna and object, representing a molecular sample. We now summarize the formalism of the equations for coupled dipoles.

The first dipole will represent the antenna and we will denote all variables accompanying its description with $(\cdot)^{\mathrm{A}}$, second dipole $(\cdot)^{\mathrm{O}}$ will represent the object. Each of the dipoles, is situated at $\mathbf{r}^{\mathrm{A(O)}}$ and has a dipole moment $\mathbf{p}_{\mathrm{r}}^{\mathrm{A(O)}}\left(\mathbf{r}^{\mathrm{A(O)}}\right)$, which we will simply denote as $\mathbf{p}^{\mathrm{A(O)}}$. The dipole produces the electric field given by Eq. (1.38)

$$\mathbf{E}_{\mathrm{dip,r}}^{\mathrm{A(O)}}(\mathbf{r}) = \frac{k^2}{\varepsilon_0}\overleftrightarrow{\mathbf{G}}\left(\mathbf{r},\mathbf{r}^{\mathrm{A(O)}}\right)\cdot\mathbf{p}^{\mathrm{A(O)}}. \tag{2.1}$$

Each dipole is driven by a total field, consisting of an incoming external field $\mathbf{E}_{\mathrm{r,inc}}\left(\mathbf{r}^{\mathrm{A(O)}}\right)$, and by the incoming field of the second dipole $\mathbf{E}_{\mathrm{r,dip}}^{\mathrm{O(A)}}\left(\mathbf{r}^{\mathrm{A(O)}}\right)$. The total field inducing each dipole then reads

$$\mathbf{E}_{\mathrm{inc,r}}^{\mathrm{tot}}\left(\mathbf{r}^{\mathrm{A(O)}}\right) = \mathbf{E}_{\mathrm{inc,r}}\left(\mathbf{r}^{\mathrm{A(O)}}\right) + \mathbf{E}_{\mathrm{dip,r}}^{\mathrm{O(A)}}\left(\mathbf{r}^{\mathrm{A(O)}}\right). \tag{2.2}$$

The induced dipole moment of each dipole can be written as[1]

$$\mathbf{p}^{\mathrm{A(O)}} = \overleftrightarrow{\boldsymbol{\alpha}}^{\mathrm{A(O)}}\cdot\left(\mathbf{E}_{\mathrm{inc}}^{\mathrm{A(O)}} + \frac{k^2}{\varepsilon_0}\overleftrightarrow{\mathbf{G}}^{\mathrm{AO(OA)}}\cdot\mathbf{p}^{\mathrm{O(A)}}\right). \tag{2.3}$$

The dipole moment can be expressed with its polarizability $\overleftrightarrow{\boldsymbol{\alpha}}^{\mathrm{A(O)}}$ via Eq. (1.37) as $\mathbf{p}^{\mathrm{O(A)}} = \overleftrightarrow{\boldsymbol{\alpha}}^{\mathrm{A(O)}}\cdot\mathbf{E}_{\mathrm{inc}}^{\mathrm{tot,A(O)}}$. The situation of the two dipoles induced by the respective incoming external field and the fields acting between them is schematically shown in Fig. 2.1 (a). The system of equations (2.3) yields the following solution

[1] We will use the notation $\mathbf{E}_{\mathrm{inc}}^{\mathrm{tot,A(O)}} = \mathbf{E}_{\mathrm{inc,r}}^{\mathrm{tot}}\left(\mathbf{r}^{\mathrm{A(O)}}\right)$ for the total field inducing each dipole, $\mathbf{E}_{\mathrm{inc}}^{\mathrm{A(O)}} = \mathbf{E}_{\mathrm{inc,r}}\left(\mathbf{r}^{\mathrm{A(O)}}\right)$ for the incoming external field and $\mathbf{E}_{\mathrm{dip}}^{\mathrm{OA(AO)}} = \mathbf{E}_{\mathrm{dip,r}}^{\mathrm{O(A)}}\left(\mathbf{r}^{\mathrm{A(O)}}\right)$ for the field of the second dipole. We denote the Green's dyadic which propagates the field from a dipole situated at $\mathbf{r}^{\mathrm{O(A)}}$ to the position of the second dipole $\mathbf{r}^{\mathrm{A(O)}}$ as $\overleftrightarrow{\mathbf{G}}^{\mathrm{AO(OA)}} = \overleftrightarrow{\mathbf{G}}\left(\mathbf{r}^{\mathrm{A(O)}},\mathbf{r}^{\mathrm{O(A)}}\right)$.

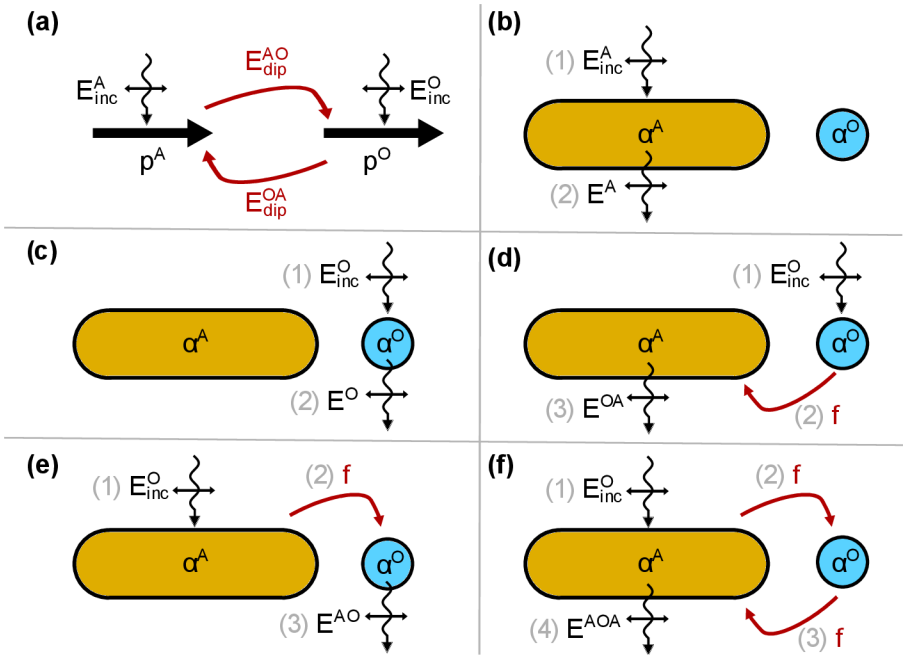

Figure 2.1: (a) Scheme of coupled dipole interaction. Each dipole has its dipole moment $\mathbf{p}^{\mathrm{O(A)}}$ driven by an external incoming field $\mathbf{E}^{\mathrm{A(O)}}_{\mathrm{inc}}$ and by the field of the second dipole $\mathbf{E}^{\mathrm{OA(AO)}}_{\mathrm{dip}}$ (b)-(f) Individual terms in Eq. (2.9) b) Field directly scattered by the antenna $\mathbf{E}^{\mathrm{A}}$ after illumination by $\mathbf{E}^{\mathrm{A}}_{\mathrm{inc}}$. (c) Field directly scattered by the object $\mathbf{E}^{\mathrm{O}}$ after being illuminated by $\mathbf{E}^{\mathrm{O}}_{\mathrm{inc}}$. (d) Incoming field $\mathbf{E}^{\mathrm{O}}_{\mathrm{inc}}$ induces the object dipole which acts with its field on the antenna, enhanced with the field enhancement $\overleftrightarrow{\boldsymbol{f}}$. The antenna then radiates field $\mathbf{E}^{\mathrm{AO}}_{\mathrm{inc}}$. (e) Same as in (d), but now the antenna field induces the object dipole, which then scatters the field $\mathbf{E}^{\mathrm{OA}}_{\mathrm{inc}}$. (f) Last term considered in Eq. (2.9): the antenna dipole is driven by the external field, the antenna induces a dipole in the object with its field, and the object then acts back, resulting in the field radiated by the antenna $\mathbf{E}^{\mathrm{AOA}}_{\mathrm{inc}}$.

$$\mathbf{p}^{\mathrm{A(O)}} = \overleftrightarrow{\boldsymbol{\alpha}}^{\mathrm{A(O)}} \cdot \left(\overleftrightarrow{\mathbf{I}} - \frac{k^4}{\varepsilon_0^2} \overleftrightarrow{\mathbf{G}}^{\mathrm{OA(AO)}} \cdot \overleftrightarrow{\boldsymbol{\alpha}}^{\mathrm{O(A)}} \cdot \overleftrightarrow{\mathbf{G}}^{\mathrm{AO(OA)}} \cdot \overleftrightarrow{\boldsymbol{\alpha}}^{\mathrm{A(O)}} \right)^{-1} \cdot \left(\mathbf{E}^{\mathrm{A(O)}}_{\mathrm{inc}} + \frac{k^2}{\varepsilon_0} \overleftrightarrow{\boldsymbol{\alpha}}^{\mathrm{O(A)}} \cdot \overleftrightarrow{\mathbf{G}}^{\mathrm{OA(AO)}} \cdot \mathbf{E}^{\mathrm{O(A)}}_{\mathrm{inc}} \right), \tag{2.4}$$

where $\overleftrightarrow{\mathbf{I}}$ is a unit dyad. This general formula can be used for the description of a weak and strong interaction between the two point dipoles. In this thesis we will consider only the weak interaction, e.g. one of the dipoles is very weakly polarizable compared to the other, or both dipoles are sufficiently apart from each other. With the weak interaction in consideration, the total field inducing each of the two dipoles $\mathbf{E}^{\mathrm{tot,A(O)}}_{\mathrm{inc}} = \mathbf{p}^{\mathrm{A(O)}} / \overleftrightarrow{\boldsymbol{\alpha}}^{\mathrm{A(O)}}$ can be developed into the Taylor series, under the assumption that norm of the operator $(k^4/\varepsilon_0^2) \overleftrightarrow{\mathbf{G}}^{\mathrm{OA(AO)}} \cdot \overleftrightarrow{\boldsymbol{\alpha}}^{\mathrm{O(A)}} \cdot \overleftrightarrow{\mathbf{G}}^{\mathrm{AO(OA)}} \cdot \overleftrightarrow{\boldsymbol{\alpha}}^{\mathrm{A(O)}}$ is less than unity [41]. We can then write

$$\mathbf{E}^{\mathrm{tot,A(O)}}_{\mathrm{inc}} = \mathbf{E}^{\mathrm{A(O)}}_{\mathrm{inc}} + \frac{k^2}{\varepsilon_0} \overleftrightarrow{\mathbf{G}}^{\mathrm{OA(AO)}} \cdot \overleftrightarrow{\boldsymbol{\alpha}}^{\mathrm{O(A)}} \cdot \mathbf{E}^{\mathrm{O(A)}}_{\mathrm{inc}} + \frac{k^4}{\varepsilon_0^2} \overleftrightarrow{\mathbf{G}}^{\mathrm{AO(OA)}} \cdot \overleftrightarrow{\boldsymbol{\alpha}}^{\mathrm{O(A)}} \cdot \overleftrightarrow{\mathbf{G}}^{\mathrm{OA(AO)}} \cdot \overleftrightarrow{\boldsymbol{\alpha}}^{\mathrm{A(O)}} \cdot \mathbf{E}^{\mathrm{A(O)}}_{\mathrm{inc}} + \dots . \tag{2.5}$$

The field scattered from each dipole $\mathbf{E}_{\mathrm{sca}}^{\mathrm{A(O)}}(\mathbf{r})$ evaluated at some observation point $\mathbf{r}$ can be again written with Eq. (1.38), We denote the Green's dyadic $\overleftrightarrow{\mathbf{G}}\left(\mathbf{r}, \mathbf{r}^{\mathrm{A(O)}}\right)$ which propagates the scattered field as $\overleftrightarrow{\mathbf{G}}_{\mathrm{sca}}^{\mathrm{A(O)}}$ and obtain

$$\mathbf{E}_{\mathrm{sca}}^{\mathrm{A(O)}}(\mathbf{r}) = \frac{k^2}{\varepsilon_0} \overleftrightarrow{\mathbf{G}}_{\mathrm{sca}}^{\mathrm{A(O)}} \cdot \overleftrightarrow{\boldsymbol{\alpha}}^{\mathrm{A(O)}} \cdot \mathbf{E}_{\mathrm{inc}}^{\mathrm{tot,A(O)}}. \tag{2.6}$$

After rewriting $\mathbf{E}_{\mathrm{inc}}^{\mathrm{tot,A(O)}}$ with Eq. (2.5) we get

$$\begin{aligned} \mathbf{E}_{\mathrm{sca}}^{\mathrm{A(O)}} = \frac{k^2}{\varepsilon_0} \overleftrightarrow{\mathbf{G}}_{\mathrm{sca}}^{\mathrm{A(O)}} \cdot \overleftrightarrow{\boldsymbol{\alpha}}^{\mathrm{A(O)}} \cdot \Big(\mathbf{E}_{\mathrm{inc}}^{\mathrm{A(O)}} + \frac{k^2}{\varepsilon_0} \overleftrightarrow{\mathbf{G}}^{\mathrm{AO(OA)}} \cdot \overleftrightarrow{\boldsymbol{\alpha}}^{\mathrm{O(A)}} \cdot \mathbf{E}_{\mathrm{inc}}^{\mathrm{O(A)}} \\ + \frac{k^2}{\varepsilon_0} \overleftrightarrow{\mathbf{G}}^{\mathrm{AO(AO)}} \cdot \overleftrightarrow{\boldsymbol{\alpha}}^{\mathrm{O(A)}} \cdot \frac{k^2}{\varepsilon_0} \overleftrightarrow{\mathbf{G}}^{\mathrm{OAAO)}} \cdot \overleftrightarrow{\boldsymbol{\alpha}}^{\mathrm{A(O)}} \cdot \mathbf{E}_{\mathrm{inc}}^{\mathrm{A(O)}} + \ldots \Big). \end{aligned} \tag{2.7}$$

We recognize the field enhancement tensor from Eq. (1.39) as

$$\overleftrightarrow{\boldsymbol{f}} = \frac{k^2}{\varepsilon_0} \overleftrightarrow{\mathbf{G}}^{\mathrm{AO}} \cdot \overleftrightarrow{\boldsymbol{\alpha}}^{\mathrm{A}}, \tag{2.8}$$

where the field produced by an antenna is evaluated at the position of the object.

The total scattered field of the antenna-object system is the sum of the scattered fields (2.7). From the reciprocity theorem and the symmetry of Green's dyadic in free space we can write $\overleftrightarrow{\mathbf{G}}^{\mathrm{AO}} = \overleftrightarrow{\mathbf{G}}^{\mathrm{OA}}$ [42], which allows us to evaluate Green's dyadic when the source and observation points are interchanged. After rearranging, where we use the fact, that polarizability tensors are considered to be diagonal, thus commutative, and expressing the field enhancement, we can write the total scattered field in the form resembling the Born series

$$\begin{aligned} \mathbf{E}_{\mathrm{sca}}^{\mathrm{tot}} = \underbrace{\frac{k^2}{\varepsilon_0} \overleftrightarrow{\mathbf{G}}_{\mathrm{sca}}^{\mathrm{A}} \cdot \overleftrightarrow{\boldsymbol{\alpha}}^{\mathrm{A}} \cdot \mathbf{E}_{\mathrm{inc}}^{\mathrm{A}}}_{\mathbf{E}^{\mathrm{A}}} + \underbrace{\frac{k^2}{\varepsilon_0} \overleftrightarrow{\mathbf{G}}_{\mathrm{sca}}^{\mathrm{O}} \cdot \overleftrightarrow{\boldsymbol{\alpha}}^{\mathrm{O}} \cdot \mathbf{E}_{\mathrm{inc}}^{\mathrm{O}}}_{\mathbf{E}^{\mathrm{O}}} + \underbrace{\frac{k^2}{\varepsilon_0} \overleftrightarrow{\mathbf{G}}_{\mathrm{sca}}^{\mathrm{A}} \cdot \overleftrightarrow{\mathbf{f}} \cdot \overleftrightarrow{\boldsymbol{\alpha}}^{\mathrm{O}} \cdot \mathbf{E}_{\mathrm{inc}}^{\mathrm{O}}}_{\mathbf{E}^{\mathrm{AO}}} \\ + \underbrace{\frac{k^2}{\varepsilon_0} \overleftrightarrow{\mathbf{G}}_{\mathrm{sca}}^{\mathrm{O}} \cdot \overleftrightarrow{\boldsymbol{\alpha}}^{\mathrm{O}} \cdot \overleftrightarrow{\mathbf{f}} \cdot \mathbf{E}_{\mathrm{inc}}^{\mathrm{A}}}_{\mathbf{E}^{\mathrm{OA}}} + \underbrace{\frac{k^2}{\varepsilon_0} \overleftrightarrow{\mathbf{G}}_{\mathrm{sca}}^{\mathrm{A}} \cdot \overleftrightarrow{\boldsymbol{f}} \cdot \overleftrightarrow{\boldsymbol{\alpha}}^{\mathrm{O}} \cdot \overleftrightarrow{\boldsymbol{f}} \cdot \mathbf{E}_{\mathrm{inc}}^{\mathrm{A}}}_{\mathbf{E}^{\mathrm{AOA}}} + \ldots, \end{aligned} \tag{2.9}$$

where we denoted the individual terms of series with superscripts, to emphasize the number of scattering events. A similar expansion of the scattered field was already done in Ref. [43]. The individual terms are described and schematically depicted in Fig. 2.1 (b-f).

2.2 Interaction with photons

When probing bulk materials with electromagnetic waves (or when emphasizing the particle nature of light, photons), we can detect the scattered waves in the forward direction, and measure the transmitted portion of the waves or in the backward direction, utilizing reflection schemes. We can then determine the material absorption, caused by the dissipation, from the energy conservation, where the sum of reflected, transmitted, and absorbed light should provide us with the total energy of the incoming light. From energy conservation, extinction is commonly defined as the decrease of the transmitted light

with respect to the initial intensity. When considering small structures, the scattering into several directions is now possible, instead of just forward transmission and backward reflection, nevertheless, we can still observe the light transmitted through in the primary direction and obtain transmission. A way to describe the interaction of small structures with incoming light is by means of optical cross sections. Cross sections represent an effective area in which the electromagnetic wave interacts with the studied object. In this context, it will be the probability that a part of the incoming power will be absorbed, scattered, or transmitted, and we obtain them by dividing the respective power (absorbed, scattered, transmitted) by the incoming power. In the next section, we derive the relations for the optical cross sections using point-dipole formalism. After that, we show numerically calculated results and compare them with the analytical ones.

2.2.1 Optical cross sections

One of the most important formulas in the description of scattering from a target is the optical theorem. It contains the conservation of energy and can be used in the description of several phenomena, for example from the description of waves (electromagnetic, acoustic). The optical theorem relates the extinguished power of an incoming plane wave impinging on an object to the scattering amplitude in the forward direction of the incoming field, and its general form is [44]

$$\sigma_{\text{ext}} = \frac{4\pi}{k}\text{Im}\{A_{\text{sca}}\}, \tag{2.10}$$

where σ_{ext} is the extinction cross section, k is free space wavenumber and A_{sca} is the scattering amplitude in the forward direction $\widehat{\mathbf{k}} = \mathbf{k}/k$. For the scattering of the electromagnetic wave, we can express A_{sca} as [12]

$$A_{\text{sca}} = \frac{\mathbf{E}^*_{\text{inc}} \cdot \mathbf{F}(\widehat{\mathbf{k}})}{\left|\mathbf{E}_{\text{inc}}\right|^2}, \tag{2.11}$$

where $\mathbf{E}_{\text{inc}}$ is the incoming field in the direction $\widehat{\mathbf{k}}$ and $\mathbf{F}(\widehat{\mathbf{k}})$ is the far-field scattering amplitude in the direction of the incoming field. The polarization of the incident field can be written by means of the field amplitude E_{inc} and the polarization vector $\hat{\boldsymbol{\epsilon}}$ as $\mathbf{E}_{\text{inc}} = E_{\text{inc}}\hat{\boldsymbol{\epsilon}}$. We now write the scattered field (1.36) in the direction $\widehat{\mathbf{k}}$ and express it with the far-field Green's dyadic (1.33) as

$$\mathbf{E}_{\text{sca}}\left(\widehat{\mathbf{k}}\right) = \frac{k^2}{\epsilon_0}\left[\overleftrightarrow{\mathbf{I}} - \frac{\mathbf{R}\otimes\mathbf{R}}{R^2}\right]\frac{\mathrm{e}^{\mathrm{i}kR}}{4\pi R}\cdot\overleftrightarrow{\boldsymbol{\alpha}}\cdot E^{\text{inc}}\hat{\boldsymbol{\epsilon}} = \frac{\mathrm{e}^{\mathrm{i}kR}}{R}\underbrace{\frac{k^2}{4\pi\varepsilon_0}\overleftrightarrow{\boldsymbol{\alpha}}\cdot E^{\text{inc}}\hat{\boldsymbol{\epsilon}}}_{\mathbf{F}(\widehat{\mathbf{k}})}, \tag{2.12}$$

where we expressed the scattered field in the direction of the incoming light $\widehat{\mathbf{k}}$, which we chose as the z-direction, and then the second term in brackets vanished, as the polarization vector $\hat{\boldsymbol{\epsilon}}$ is perpendicular to the propagation direction. We also defined the far-field scattering amplitude $\mathbf{F}(\widehat{\mathbf{k}})$. If we express A_{sca} from Eq. (2.11) with $\mathbf{F}(\widehat{\mathbf{k}})$ from Eq. (2.12) and plug it into the optical theorem in Eq. (2.10) we get the formulation of the extinction cross section

$$\sigma_{\text{ext}} = \frac{k}{\varepsilon_0}\text{Im}\{\hat{\boldsymbol{\epsilon}}^*\cdot\overleftrightarrow{\boldsymbol{\alpha}}\cdot\hat{\boldsymbol{\epsilon}}\}. \tag{2.13}$$

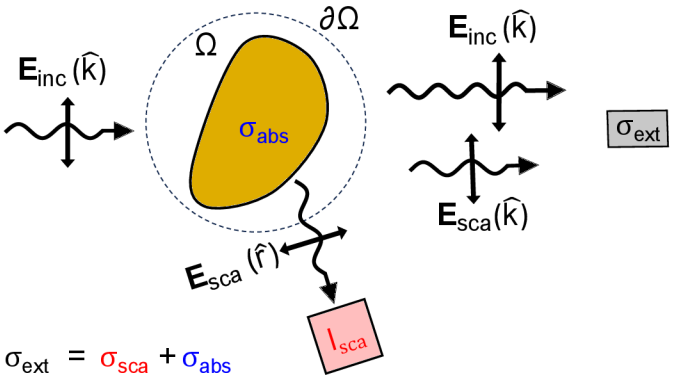

Figure 2.2: Schematic representation of light scattering on a structure. The incoming light propagates in a direction given by $\widehat{\mathbf{k}}$. After the interaction with an object, light can be absorbed or scattered. By integrating over a spherical boundary enclosing the sample, we get the scattering cross section. By placing a detector in the direction $\widehat{\mathbf{k}}$, we get the transmitted light, which is diminished by the extinction, summing the scattered and absorbed portions of the incoming light.

The extinction cross section has the unit of area. We schematically depict the extinction measurement in Fig. 2.2. It is measured by placing a detector after the object in the direction of the incoming wave and tells us, how was the incoming power attenuated by the interaction of incoming light with an object it impinges on. There are two possible channels through which the power can be lost. It can be scattered in different directions than that of the passing incoming light or it can get absorbed in the object.

Now we express the scattering cross section, which tells us about the total power scattered from the object. It is usually defined by considering outwards power flow through an imaginary border enclosing an object which radiates, which is then integrated over the imaginary border and normalized to the incoming power. As we expressed by the Eq. (1.17), the energy flow of the electromagnetic field can be expressed via the Poynting vector $\langle \mathbf{S} \rangle$. By integrating the time-averaged Poynting vector of the scattered field $\langle \mathbf{S}_{\mathrm{sca}} \rangle$ over the imagined boundary $\partial\Omega$ enclosing the volume Ω and dividing by the magnitude of the time-averaged Poynting vector of the incoming field $\langle \mathbf{S}_{\mathrm{inc}} \rangle$ we get the scattering cross section

$$\sigma_{\mathrm{sca}} = \frac{1}{\langle \mathbf{S}_{\mathrm{inc}} \rangle} \oint_{\partial\Omega} \langle \mathbf{S}_{\mathrm{sca}} \rangle \cdot \hat{\mathbf{r}} \mathrm{d}\Omega, \tag{2.14}$$

where $\mathrm{d}\Omega$ is an infinitesimal element of the boundary and $\hat{\mathbf{r}}$ is a unit vector normal to this element. After expressing the Poynting vector from Eq. (1.19) we get

$$\sigma_{\mathrm{sca}} = \frac{1}{\left|\mathbf{E}_{\mathrm{inc}}\right|^2} \oint_{\partial\Omega} \left|\mathbf{E}_{\mathrm{sca}}\right|^2 \mathrm{d}\Omega. \tag{2.15}$$

By inserting the far-field formulation of $\mathbf{E}_{\mathrm{sca}}$ for oscillating dipole as in Ref. [12] we get the scattering cross section in the form

$$\sigma_{\mathrm{sca}} = \frac{k^4}{6\pi\varepsilon_0^2} \left| \overleftrightarrow{\boldsymbol{\alpha}} \cdot \hat{\boldsymbol{\epsilon}} \right|^2. \tag{2.16}$$

We again schematically show a scattering experiment, where the scattered intensity I_{sca} is measured in Fig. 2.2.

From the optical theorem, we know that the extinction cross section contains the total extinguished power. The power that is taken from the incoming wave can also be lost due to the dissipation in the structure and is labeled as the absorption cross section, which is expressed as

$$\sigma_{\text{abs}} = \sigma_{\text{ext}} - \sigma_{\text{sca}}. \tag{2.17}$$

For small or weakly polarizable absorbing structures with small $\overleftrightarrow{\boldsymbol{\alpha}}$, the scattering cross section becomes negligible and the absorption cross section becomes the major contributor to the extinction $\sigma_{\text{abs}} \approx \sigma_{\text{ext}}$ [45].

2.2.2 Numerical calculations of optical cross sections

Numerical simulations of the response of nanostructures to the impinging electromagnetic waves are one of the major contributors to explaining the response. They provide information about the field magnitudes, phases, and other quantities usually unattainable in standard far-field experiments, although some near-field techniques can measure them [38, 46], and they can be afterward directly compared with numerical simulations. In this thesis, we use two commercial numerical solvers, finite-difference time-domain (FDTD) Ansys Lumerical software for the computations of the response of nanostructures to plane-wave illumination, and finite-element-method based COMSOL MULTIPHYSICS for the computations of plane-wave and electron-beam excitation.

In this section, we will show numerically calculated optical cross sections and compare them with the analytical results, using formalism for the extinction and scattering cross sections introduced in the previous section. We will be specifically interested in the computation of the far-field response of infrared (IR) antennas, for which we will use FDTD Lumerical (the methodology is described in Appendix C.1). In comparison to the optical antennas, the metallic infrared antennas are much larger, as was discussed in Sec. 1.5. Because of the size of the IR antennas, the scattering emerges as a non-negligible contribution to the total extinction and, in some cases, even dominates it. We now show the calculations of the response of nano-antennas of the same shape and similar dimensions to ones previously used and thoroughly discussed in Ref. [47], as they will be used in the next chapter for the modeling of the enhanced spectroscopies. The antennas are hemispherically ended cylinders with varying diameters D. By changing the diameter, the resonance for an antenna of a certain length shifts towards shorter wavelengths, as we can see in Fig. 2.3 (a). The antenna dimensions are also in Tab. D.2.

For the later application in enhanced spectroscopy, which we discuss in Chap. 4, the resonance of the antennas has to be tuned to approximately 7.9 µm, which roughly corresponds to the Si-CH_3 vibration in polydimethylsiloxane (PDMS) molecule. The antenna had to be elongated, to shift the resonance towards a longer wavelength [the resonance wavelength scales linearly with the antenna length, as we can see from Eq.(1.46)]. The lengths and sizes of the antennas are plotted together with a schematic depiction of the shape in Fig. 2.3 (b) with green dots.

We can see the numerically calculated cross sections for gold nano-antenna of 100 nm diameter in Fig. 2.4 (a). The extinction and scattering cross sections were obtained from the FDTD monitors, their sum provides the extinction cross section. In Fig. 2.4 (b) with circles and full lines, we plot the maxima of the three numerically calculated cross sections maxima for the different sizes of nano-antennas from Fig. 2.3 (b). As was already

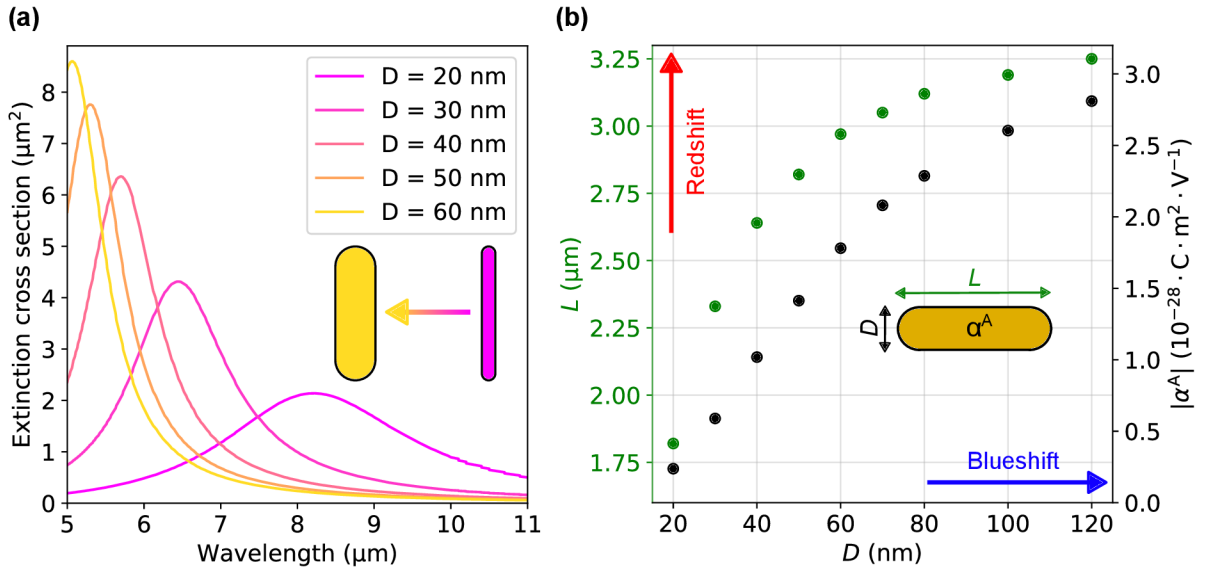

Figure 2.3: (a) Simulated extinction cross sections for gold antennas of length 1.82 µm and varying diameter. When broadening the nano-antenna, the resonance energy shifts toward shorter wavelengths (blueshift). (b) Lengths and diameters (green dots) of gold nano-antennas, whose resonances are tuned to approximately $\lambda_{\mathrm{res}} = 7.9\,\mu\mathrm{m}$. With the black dots, we plot the dependence of the magnitude of the x-component of the antenna polarizability (evaluated at the λ_{res}). To maintain the same resonance frequency while increasing the diameter D (blueshift of the resonance) of the nano-antennas, they had to be elongated as well (redshift of the resonance). Optical response of the gold antennas in (a) and (b) is modeled with the dielectric function from Ref. [19], plotted in Fig. 1.2 (d).

discussed in Ref. [47], we can distinguish three antenna regimes as the ratio between the magnitude of absorption and scattering cross sections changes as a function of the antenna size. We can see that for the smallest antennas, the majority of the contribution to extinction is from the antenna absorption, yielding $\sigma_{\mathrm{ext}} \approx \sigma_{\mathrm{abs}}$.As we increase the antenna size, the scattering and absorption increase, too, until the diameter of 60 nm. For this antenna, the absorption cross section has a maximal value and matches the scattering in its magnitude. From this point on, the absorption decreases. On the other hand, the scattering keeps increasing, and with the larger antennas, we enter the last regime, where the major contribution to the extinction is from scattering. Absorption appears to be asymptotically approaching zero, so for larger antennas, the contribution to the extinction would be given mainly by the scattering $\sigma_{\mathrm{ext}} \approx \sigma_{\mathrm{sca}}$.

This behavior has been previously discussed in terms of the theory of resonators, where depending on the ratio between the internal (dissipation) and external (radiation) losses, we can distinguish three coupling regimes [48]. When the external-to-internal ratio (e.g. the ratio between the scattering and absorption) is below one, when the antenna is dominantly absorbing, the regime is called under-coupled. When the external-to-internal ratio is equal to one, the resonator is denoted as critically-coupled, for larger antennas, where the external losses prevail, the regime is called over-coupled. These three regimes play an important role in the enhanced spectroscopies, and they will be discussed in the next chapter.

Now we compare the numerically calculated cross sections with the analytical relations from Sec. 2.2. We can substitute the calculated antenna polarizability in equations for

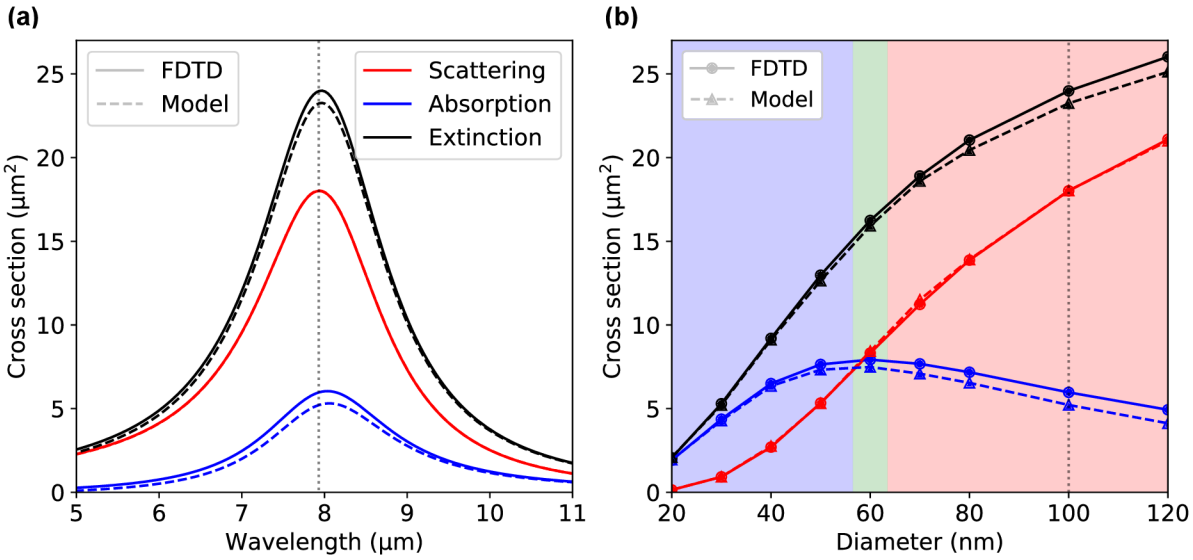

Figure 2.4: (a) Comparison of the optical cross sections calculated numerically by FDTD (full lines) and semi-analytically obtained using Eqs. (2.18-2.20) (dashed line) for a gold nano-antenna which is cylindrically shaped with hemispherical apexes. The antenna diameter is $D = 100\,\text{nm}$ and length is $L = 3190\,\text{nm}$. The numerical and analytical calculations match fairly well when evaluating the scattering, the extinction and absorption shows a discrepancy. (b) Cross section values at resonance wavelength λ_{res} plotted as a function of the antenna diameter D for different antenna sizes from Fig. 2.3 (b). With the vertical dashed line, the points for the antenna from (a) are highlighted. With the blue background (nano-antenna diameters under about 50 nm), we mark the under-coupled regime, with the green background (diameter 60 nm) the critically coupled regime, and with the red background (diameters over about 70 nm) the over-coupled regime.

the extinction (2.13) and scattering (2.16) and calculate the cross sections. We obtain the absorption cross section from the energy conservation (2.17).

We will use computed polarizabilities obtained using multipole expansion for nanophotonics (MENP) package as described in Appendix C.1. We consider incoming electromagnetic plane wave with x-polarization, so that $\mathbf{E}_{\text{inc}} = E_{\text{inc}}\hat{\boldsymbol{x}}$, where $\hat{\boldsymbol{x}}$ is a unit vector in the x-direction. The antenna's long axis is oriented along the x-axis, so the response would come only from the x-component of the polarizability $\alpha^{\text{A}}_{\text{xx}}$. In the next we simply denote $\alpha^{\text{A}}_{\text{xx}} = \alpha^{\text{A}}$. In Fig. 2.3 (b), we plot the obtained magnitude of the scalar polarizabilities $\left|\alpha^{\text{A}}\right|$ for different dimensions of nano-antennas, whose resonances are tuned to approximately $\lambda_{\text{res}} = 7.9\,\mu\text{m}$. Both antenna length and polarizability are seemingly saturating and have decreasing slopes for larger antennas. This behavior can be interpreted by an interplay between the dependences of polarizability on the antenna length and the diameter. When considering the scalar polarizabilities, Eqs. (2.13),(2.16) and (2.17) can be simplified

$$\sigma^{\text{A}}_{\text{ext}} = \frac{k}{\varepsilon_0}\text{Im}\{\alpha^{\text{A}}\}, \tag{2.18}$$

$$\sigma^{\text{A}}_{\text{sca}} = \frac{k^4}{6\pi\varepsilon_0^2}\left|\alpha^{\text{A}}\right|^2, \tag{2.19}$$

$$\sigma^{\text{A}}_{\text{abs}} = \sigma^{\text{A}}_{\text{ext}} - \sigma^{\text{A}}_{\text{sca}}. \tag{2.20}$$

We plot these expressions, into which we plugged the computed polarizability of the antenna of 50 nm with dashed lines in Fig. 2.4 (a). We can see that the scattering obtained from the model matches almost perfectly with the numerically calculated result, but in extinction and absorption, there is a slight discrepancy. We again take the maxima of the calculated cross sections and plot them into Fig. 2.4 (b), with triangles and dashed lines. We can see that the scattering cross sections match well, the relative error is smaller than 2.5% for all antennas except for the smallest one with diameter 10 nm, where the error is about 5%. This could be because of too coarse mesh of the simulation.

The extinction shows a discrepancy between the numerically and analytically obtained spectra, and the error is about 2.5%. The absorption cross sections show a discrepancy, which is similar in size to the extinction (as the absorption is obtained from the energy conservation), although as it diminishes, the error grows. The discrepancy shall be a focus of future study, although we assume it arises as a consequence of the dipole approximation.

Up to this point, we have only dealt with nano-antennas of a cylindrical rod shape with hemispherical apexes. After inducing a dipolar resonance within the nano-antenna, the electric field is greatly enhanced at the antenna apexes. We now describe the case of two neighboring nano-antennas separated by a nanometric gap. When the resonance is induced in the nano-antennas, they can interact via their near-fields in the gap dividing them and can be coupled [49].

The lower-energy mode emerging due to the dipolar coupling is associated with the dipoles within the nano-antennas that oscillate in phase and is called a bright mode (sometimes denoted as bonding). The net dipole moment of such mode is non-zero, thus the interaction with the plane electromagnetic wave is efficient [50]. This mode is relatively redshifted to the dipolar resonance of just one antenna forming the dimer. The charges at the ends forming the gap are attracted, thus deforming the symmetry which was in the isolated nano-antenna. When we compare the field enhancement near the antenna apex for isolated nanorods, much stronger field enhancement is obtained in the gap [37]. We illustrate the dimer nano-antenna by simulation results in Fig. 2.5 (a), where we illuminated the nano-antenna with a plane wave which is polarized along the long antenna axis. We can see that the near field is enhanced at the far tips of the dimer nano-antenna, similarly to the isolated nano-antenna [Fig. 1.3 (c)], but we also see the stronger field localized in the gap. The field enhancement strongly depends on the size of the gap and grows when we shrink it [51]. As the computations were performed for an antenna with flat ends forming the gap, we can see that the field is largest near the outer rim of the cylinder, because of the sharp edge.

The second coupled-antenna mode, which has higher energy, is formed by two anti-parallel dipoles. Therefore, it has zero net dipole moment and it cannot be excited by the plane wave and also does not radiate. For this reason, it is sometimes called dark (or anti-bonding) mode. Albeit when studying nano-antennas with, for example, fast electrons (which we discuss in Sec. 2.3) or sharp illuminated tips producing near-fields, we can excite even these dark modes and higher-order modes.

We show numerically calculated optical cross sections for bright-mode in gold dimer antenna in Fig. 2.5 (b) with the full line. The antenna diameter is 20 nm and its length is 2795 nm. We tuned the antenna resonance by adjusting the length of the rods to approximately 7.9 µm. As the dipoles are coupled, we cannot simply model the response as the sum of the individual polarizabilities of the isolated nanorods [37]. Nevertheless, we explore the possibility of approximative analytical calculation of the cross sections via

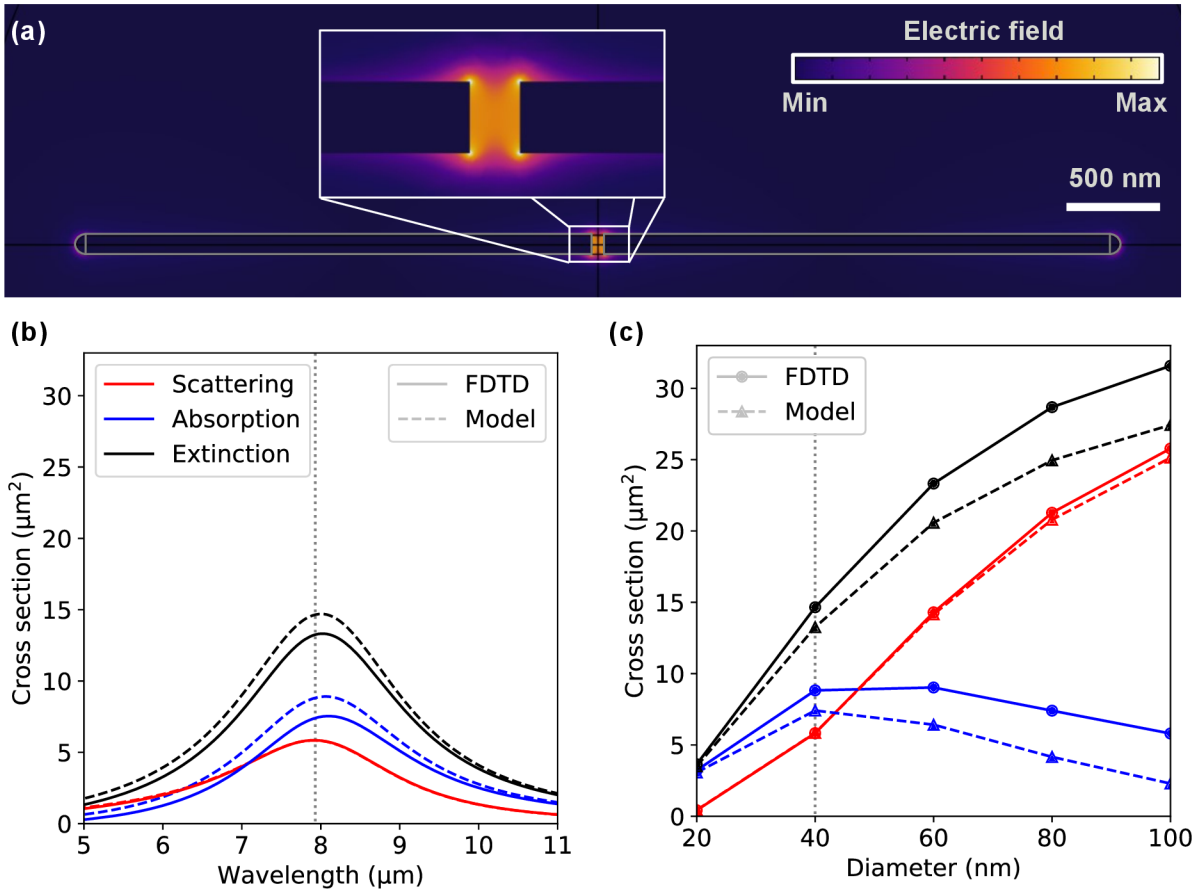

Figure 2.5: (a) Electric field of a bright mode within plasmonic dimer nano-antenna consisting of two cylindrical nanorods, with one flat end (in the gap) and one hemispherical end. The gap between the nano-rods is 70 nm, the diameter of rods is 100 nm, and each rod has a length of 2795 nm. The dimer is illuminated by a plane wave with orientation aligned with the dimer's long axis. We can see that the largest near-field enhancement is localized in the gap. (b) Calculated optical cross section of dimer antenna of diameter 40 nm. We compare the results of FDTD simulations (full lines) with the results of a point dipole approximation (dashed lines). With the vertical dotted line, we mark the resonance wavelength $\lambda_{\text{res}} = 7.9\,\mu\text{m}$. (c) Cross sections maxima at the resonance. With the dotted line, we denote the values from (b).

Eqs. (2.18-2.20), with which we assume that we can model the behavior of two coupled dipoles by an effective polarizability of a single dipole centered in the center of the gap. We show the results of such approximative dipole expansion in Fig. 2.5 (b) with the dashed lines. We can see that the scattering cross section is described fairly well, but the extinction has an error of about 10% and absorption 20%. To obtain correct values of the cross section from the dipole expansion, the expansion would have to be done for one antenna forming the dimer and then the dipole moment of the coupled antennas would need to be modeled via coupled dipole model described in Sec. 2.1.

We again change the nano-antenna diameter (while changing its length to keep the same resonance frequency) and show the calculated cross sections in Fig. 2.5 (c). The dimensions of the antennas are in Tab. D.2. We obtain similar behavior as for the isolated nano-antennas in Fig. 2.4 (b) For smaller diameters (20 nm and 40 nm), the dimer is in the under-coupled regime, where the extinction is given mainly by the absorption cross section.

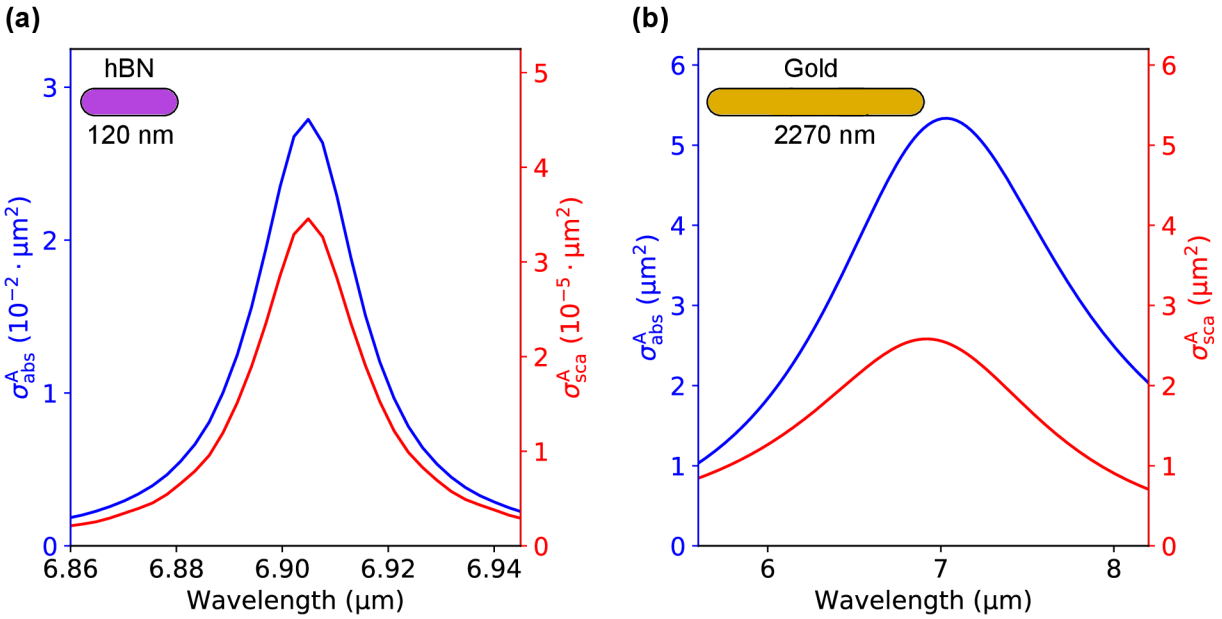

Figure 2.6: (a) Absorption (blue) and scattering (red) cross section of hBN antenna of diameter $D = 40\,\text{nm}$ and length $L = 120\,\text{nm}$. The antenna is cylindrical with hemispherical apexes. The antenna is tuned to the vibrational resonance of the C-H bond in a CBP molecule at approximately 6.91 µm [Fig. 1.2 (c)]. (b) Absorption and scattering cross sections of gold nano-antenna of the same shape as hBN antenna in (a), with $D = 40\,\text{nm}$ and length $L = 2270\,\text{nm}$. Compared to the hBN antenna, we can see that the cross sections of the gold antenna are much broader, and about two orders of magnitude larger for absorption and five orders for scattering. Cross section were numerically calculated in FDTD.

For larger antennas, with diameters larger than 60 nm, we have the over-coupled regime, where the scattering prevails and the absorption cross section is diminishing. Somewhere between diameters 40 nm and 60 nm, we would expect the critically coupled nano-antenna, which has maximal absorption and has the same magnitude as the scattering. We again compare the numerically simulated cross sections with the analytical model of one dipole approximating the response, for which we plot the results with triangles and dashed lines in Fig. 2.5 (c). We can see the scattering cross sections are predicted fairly well for all antenna diameters, the relative error is always under 5%. The error in the extinction and absorption cross sections grows from about 5% for the smallest antennas up to 15% for the largest antennas. We can also compare the values of optical cross sections with Fig. 2.4 (a), and see that the dimer antennas which are larger have larger cross sections.

We now focus back on isolated rod-shaped nano-antennas, whose resonances are of a different nature than localized plasmons in gold. It was already shown, that nano-antennas made of hexagonal boron nitride (hBN) can support localized phonon polariton resonances [52, 53]. The gold nano-antennas previously considered in this section were tuned approximately 7.9 µm, e.g. the resonance frequency of Si-CH_3 vibration in PDMS. The upper reststrahlen band of hBN, where localized surface phonon polaritons can be supported within the nano-antenna, lies between 6.12 µm and 7.35 µm, thus the antenna resonance can not be tuned to the PDMS resonance. Because of this, we choose CBP molecule with vibrational resonance around 6.91 µm [shown in Fig. 1.2 (b)], which was previously considered in Refs. [54, 55, 56], as the resonance is within the reststrahlen band

of hBN. We plot the numerically calculated scattering and absorption cross sections in Fig. 2.6 (a). The hBN antenna has length 120 nm and diameter 40 nm. We can see that the absorption cross section is approximately 3 orders larger than the scattering, thus the antenna is in the under-coupled regime.

We can immediately recognize, that the cross sections are several orders smaller than previously considered golden nano-antennas [Fig. 2.4 (b)]. For a fair comparison, we computed scattering and absorption cross sections of golden nano-antennas of different dimensions, whose resonances are tuned to that of CBP at 6.9 µm [Fig. 1.2 (b)]. We plot the result of the antenna of diameter 40 nm in Fig. 2.6 (b). We can recognize that the antenna is in the under-coupled regime (absorption is larger than scattering), but for larger diameters of gold antennas, we were again able to achieve the critically-coupled and over-coupled regimes.

2.3 Interaction with electrons

In contrast to photons, where the incoming excitation can be spatially much larger compared to the dimensions of the studied nanostructures, the use of localized probes offers better spatial resolution and the possibility for spatially resolved probing and spectroscopy. Such localized probes could be tips used in scanning probe microscopy or focused beams of electrons. In this section, we will develop the basics of the theory of investigating excitations in nanostructures with a beam of swift electrons with electron energy-loss spectroscopy (EELS). For further reading, we refer to the enchiridion of the description of the field of an electron beam interaction with the sample, which is Ref. [57].

2.3.1 EELS and the loss probability

EELS can be performed in a scanning transmission electron microscope (STEM) while studying the energy lost by the electrons transmitted through a sample. We now describe the experimental setup and depict it schematically in Fig. 2.7 (a). Electrons are extracted from the gun and accelerated with a high voltage (typically ranging from 60 kV to 300 kV), thus moving at relativistic speeds. The electron beam then passes through focusing optics and a monochromator, so the beam spot size and energy spread are greatly reduced. The beam then passes through or in the vicinity of the studied sample. Most of the electrons interact elastically or do not interact at all, thus they preserve their initial energy. Some of the electrons can interact inelastically and lose a part of their initial energy in the process. The electrons that do not lose any energy give rise to a so-called zero-loss peak (ZLP), which usually prevails over all the other contributions in magnitude and produces (an unwanted) background and, thus typically needs to be subtracted from the spectra. The full-width at half maximum (FWHM) of the zero-loss peak gives us information about the energy resolution. When analyzing the inelastically scattered electrons, we usually distinguish two spectral ranges. The low-loss region ranges from the lowest energies accessible by the energy resolution, which is for state-of-art microscopes having around 10 meV [58] and extends to tens of eV. The core-loss region of EELS encompasses energy losses of tens to hundreds of eV, which are associated with transitions of electrons from core-level states to valence states, giving information about elemental and chemical composition. In this thesis, we focus only on the low-loss region of the EEL spectra. This

region contains losses due to vibrational excitations, excitations of valence electrons, or interband electronic transitions, as well as quasiparticle excitations. Such excitations can be bulk and surface plasmons, phonons, or optical waveguide modes. Many of these excitations are normally undetectable by standard optical spectroscopic techniques because of energy-momentum mismatch with freely propagating photons. As we will show later in this section, the field of the electron beam is evanescent and thus can provide enough momentum and in turn induce such excitations. When the sample is nanostructured, localized plasmons or phonons can be excited. Again, contrary to the standard photon investigation, due to the high localization of the electron beam and the symmetry of its field, we can probe even the dark modes, which are not radiative [59]. When the excitation is radiative, cathodoluminescence (CL) can be measured on a detector, we will discuss cathodoluminescence theoretically in the section. Some of the processes triggered by the field of swift electrons are depicted in Fig. 2.7 (b).

After the interaction, the beam passes through a magnetic prism, acting as an electron spectrometer, where it is distributed by energies with the act of Lorentz force. After that, the spectrally distributed electrons land on the detector, where after integration of all the electrons we obtain the loss spectrum. The samples can be studied spatially, as STEM offers a scanning regime, where we scan over the sample. From each scanned point we obtain the EEL spectrum, while looking at one particular energy loss and imaging the whole scanned region, one can obtain a so-called EELS map, gaining spatial information about the loss event.

We now move to the theoretical description of the interaction between the fast electron and the sample. The moving electron can be represented as a point charge traversing along trajectory $\mathbf{r}_\mathrm{B}$. We can express the moving charge by means of the current density which can be rewritten via the charge density $\rho_\mathrm{e}(\mathbf{r},t) = -e\delta(\mathbf{r}-\mathbf{r}_\mathrm{B})$ as

$$\mathbf{J}_\mathrm{e}(\mathbf{r},t) = \rho_\mathrm{e}\mathbf{v} = -e\mathbf{v}\delta(\mathbf{r}-\mathbf{r}_\mathrm{B}). \tag{2.21}$$

We assume that the electron moves in the straight line positive z-direction, through the point $\mathbf{R}_\mathrm{B} = (x_\mathrm{B}, y_\mathrm{B})$, the geometry is depicted in the inset of Fig. 2.7 (c). By transforming the current density into ω-space, changing the derivation over t with derivation over z and using the filtration ability of the δ-function we get

$$\mathbf{J}_\mathrm{e}(\mathbf{r},\omega) = -e\hat{\mathbf{v}}\delta(\mathbf{R}-\mathbf{R}_\mathrm{B})\mathrm{e}^{\mathrm{i}\omega z/\mathrm{v}}. \tag{2.22}$$

With the help of the current density, we can express the components of the electromagnetic field produced by the moving electron. We now express the perpendicular and parallel components of the electric field of a swift electron $\mathbf{E}(\mathbf{r},\omega) = (\mathbf{E}_R, E_z)$ traversing in the z-direction. The field components perpendicular to the electron trajectory are

$$\mathbf{E}_R(\mathbf{R},\omega) = \frac{2e\omega}{4\pi\varepsilon_0\gamma_\mathrm{L}v^2}e^{i\omega z/v}K_1\left(\frac{\omega\left|\mathbf{R}-\mathbf{R}_\mathrm{B}\right|}{v\gamma_\mathrm{L}}\right)\frac{\mathbf{R}-\mathbf{R}_\mathrm{B}}{\left|\mathbf{R}-\mathbf{R}_\mathrm{B}\right|}, \tag{2.23}$$

where $\gamma_\mathrm{L} = \sqrt{1/(1-v^2/c^2)}$ is the Lorentz factor, v is the electron velocity, and K_1 is the first-order modified Bessel function of the second kind. We can see that the field is polychromatic. In contrast to the spatially broad monochromatic electromagnetic plane wave, the electron beam represents a localized field source covering a broad range of energies. We plot the parallel components of the electric field of the moving electron for

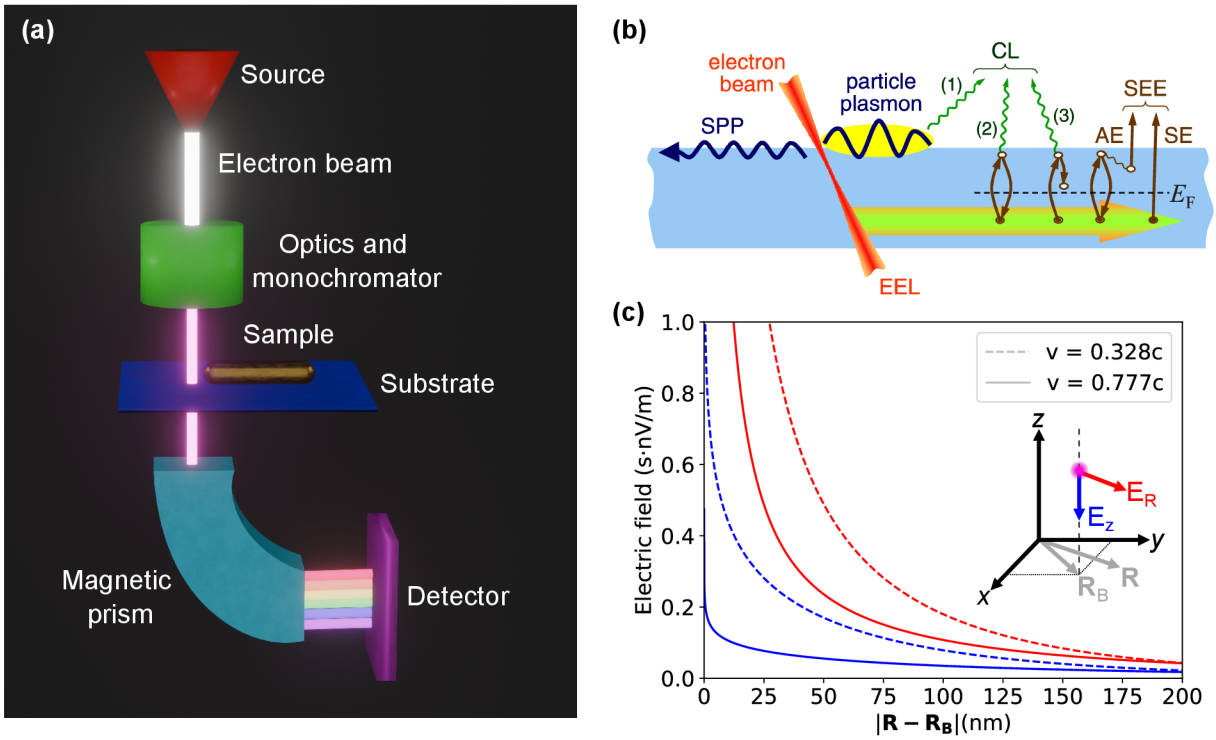

Figure 2.7: a) Schematic representation of the EELS experiment. b) Some processes emerging after the interaction of the matter with a beam of swift electrons. On planar surfaces, propagating surface plasmon polaritons (SPP) can be excited, when the beam interacts with a tailored structure, localized (particle) surface plasmons (LSP). Energy can be lost in favor of electron transitions. For radiative processes we can detect the emitted photons as cathodoluminiscence (CL). Secondary electrons (SE) leaving the sample can be detected, as well as Auger electrons (AE). Adapted from [57] c) Electric field of a swift electron in parallel and perpendicular direction for two electron velocities $0.328c$ and $0.777c$, corresponding to accelerating voltages 30 kV and 300 kV respectively, which is the range typically used in STEM. In the inset, the geometry is depicted.

two velocities at Fig 2.7 (c) with red curves. The field decays with the distance, and we can see that the decay is greater for the larger velocity. At larger distances, both curves approach an exponential asymptote [57], and the field is thus evanescent. This is in contrast to the field of freely propagating plane waves. For the component of the field parallel to the electron movement, we get

$$E_z(z,\omega) = \frac{2e\omega \mathrm{i}}{4\pi\varepsilon_0\gamma_\mathrm{L}^2 v^2} e^{i\omega z/v} K_0\left(\frac{\omega|\mathbf{R}-\mathbf{R}_\mathrm{B}|}{v\gamma_\mathrm{L}}\right), \tag{2.24}$$

where K_0 is the zeroth-order modified Bessel function of the second kind. We plot the z-component of the electric field with blue curves in Fig. 2.7 (c), again for two different velocities. Similarly to the perpendicular components, the field is evanescent and decays with distance from the electron.

Straightforward interpretation of experimental EEL spectra is often impossible due to the finite spectral resolution, and possible distortions due to microscope and spectrometer aberrations. Furthermore, the highly localized nature of the EEL signal and its spatial variations require theoretical models to provide further insights and explanations. We can

derive a formula for calculating the loss probability Γ_{EELS}, that electron loses a quantum of energy $\hbar\omega$ while interacting with the sample. We start by expressing the dissipated power from the Eq. (1.17), and we integrate it over time to obtain the change in energy ΔE due to dissipation in the sample as

$$\Delta E = -\int_{-\infty}^{\infty} \mathrm{d}^3\mathbf{r} \int_{-\infty}^{\infty} \mathbf{J}_{\mathrm{e}}^{*} \cdot \mathbf{E}^{\mathrm{ind}}(\mathbf{r}, t)\mathrm{d}t, \tag{2.25}$$

where $\mathbf{J}_{\mathrm{e}}^{*}$ is complex conjugate of the driving current density of the electron beam and $\mathbf{E}^{\mathrm{ind}}$ is the field induced in the sample. Now we express the energy loss in the frequency space, to assign each frequency a probability of the event. By using the Rayleigh-Parseval theorem (A.5) we get

$$\Delta E = -\frac{1}{\pi}\int_{-\infty}^{\infty} \mathrm{d}^3\mathbf{r} \int_{0}^{\infty} \mathrm{Re}\Big\{\mathbf{J}_{\mathrm{e}}^{*} \cdot \mathbf{E}^{\mathrm{ind}}(\mathbf{r}, \omega)\Big\}\mathrm{d}\omega = \int_{0}^{\infty} \hbar\omega\Gamma_{\mathrm{EELS}}(\omega)\mathrm{d}\omega, \tag{2.26}$$

where we defined the loss probability Γ_{EELS} as

$$\Gamma_{\mathrm{EELS}}(\omega) = -\frac{1}{\pi\hbar\omega}\int_{-\infty}^{\infty} \mathrm{Re}\Big\{\mathbf{J}_{\mathrm{e}}^{*} \cdot \mathbf{E}^{\mathrm{ind}}(\mathbf{r}, \omega)\Big\}\mathrm{d}^3\mathbf{r}. \tag{2.27}$$

If we now plug in the current density from Eq. (2.22) we get

$$\Gamma_{\mathrm{EELS}}(\omega) = \frac{e}{\pi\hbar\omega}\int_{-\infty}^{\infty} \mathrm{Re}\Big\{\hat{\mathbf{v}} \cdot \mathbf{E}^{\mathrm{ind}}(\mathbf{R}_{\mathrm{b}}, z, \omega)\mathrm{e}^{-\mathrm{i}\omega z/v}\Big\}\mathrm{d}z, \tag{2.28}$$

which is the loss probability formula obtained from the solution concerning the work performed on the electron by the induced field as first formulated in [60]. The loss probability can be directly compared with experimentally measured normalized spectra from STEM experiments. We can see that to obtain the loss probability, we only need to find the induced electric field. For bulk, surface, and some simple geometries, we can express the induced field and calculate the loss probability analytically. For more complex geometries, implementation of this formalism into some numerical solver is necessary. We describe the calculations of EELS in COMSOL MULTIPHYSICS in Appendix section C.2.2 and show results of the numerical calculations in Sec. 2.3.3.

2.3.2 Loss probability in the interaction with the point dipole

When considering the excitation of a dipole in an arbitrarily shaped nanostructure, we will use the formalism of a point dipole. We now derive the loss probability, that an electron loses energy by inducing a dipole moment of the point dipole with its field. We start by plugging for the current density of the electron beam from Eq. (2.22) into Eq. (2.27) for the loss probability. The induced field of a point dipole located at $\mathbf{r}_{\mathrm{p}}$ can be written with Eq. (1.36) and we get

$$\Gamma_{\mathrm{EELS}}(\omega) = \frac{e}{\pi\hbar\omega}\int_{-\infty}^{\infty} \mathrm{Re}\Big\{\delta(\mathbf{R} - \mathbf{R}_{\mathrm{B}})\mathrm{e}^{-\mathrm{i}\omega z/\mathrm{v}}\omega^2\mu_0 \overleftrightarrow{\mathbf{G}}(\mathbf{r}, \mathbf{r}_{\mathrm{p}}) \cdot \overleftrightarrow{\boldsymbol{\alpha}} \cdot \mathbf{E}^{\mathrm{el}}(\mathbf{r}_{\mathrm{p}})\Big\}\mathrm{d}^3\mathbf{r}. \tag{2.29}$$

We now multiply the loss probability with $-\mathrm{i}^2$ and interchange the real and imaginary parts of the integrand and use the delta function. The loss probability is then

$$\Gamma_{\mathrm{EELS}}(\omega) = -\frac{e}{\pi\hbar\omega}\int_{-\infty}^{\infty} \mathrm{Im}\Big\{\mathrm{e}^{-\mathrm{i}\omega z/\mathrm{v}}\mathrm{i}\omega^2\mu_0 \overleftrightarrow{\mathbf{G}}(\mathbf{R}_{\mathrm{B}}, z, \mathbf{r}_{\mathrm{p}}) \cdot \overleftrightarrow{\boldsymbol{\alpha}} \cdot \mathbf{E}^{\mathrm{el}}(\mathbf{r}_{\mathrm{p}})\Big\}\mathrm{d}z. \tag{2.30}$$

We again exploit the symmetry of the Green's dyadic $\overleftrightarrow{\mathbf{G}}(\mathbf{R}_\mathrm{B}, z, \mathbf{r}_\mathrm{p}) = \overleftrightarrow{\mathbf{G}}(\mathbf{r}_\mathrm{p}, \mathbf{R}_\mathrm{B}, z)$ and we can recognize $(-e)\mathrm{i}\omega\mu_0 \int_{-\infty}^{\infty} \overleftrightarrow{\mathbf{G}}(\mathbf{r}_\mathrm{p}, \mathbf{R}_\mathrm{B}, z)\mathrm{e}^{-\mathrm{i}\omega(z)/\mathrm{v}}\mathrm{d}z$ as the complex conjugate of the field produced by the electron at the position of the dipole $\mathbf{E}^{\mathrm{el},*}(\mathbf{r}_\mathrm{p})$ and write

$$\Gamma_\mathrm{EELS}(\omega) = \frac{1}{\pi\hbar}\mathrm{Im}\Big\{\mathbf{E}^{\mathrm{el},*}(\mathbf{r}_\mathrm{p}) \cdot \overleftrightarrow{\boldsymbol{\alpha}} \cdot \mathbf{E}^{\mathrm{el}}(\mathbf{r}_\mathrm{p})\Big\}. \tag{2.31}$$

We can see that this formulation of the loss probability resembles the relation for the extinction cross section in Eq. (2.13), which is however normalized to the incoming intensity and scaled with k and different prefactor. Extinction is also normalized to the incoming light intensity I, while in loss probability, the frequency dependence embedded in the electric field of the fast electrons still plays a role. We can also write the loss probability using the dipole moment and arrive at the expression

$$\Gamma_\mathrm{EELS}(\omega) = \frac{1}{\pi\hbar}\mathrm{Im}\Big\{\mathbf{E}^{\mathrm{el},*}(\mathbf{r}_\mathrm{p}) \cdot \mathbf{p}\Big\}. \tag{2.32}$$

2.3.3 Numerical calculations of EELS

In Sec. 2.2.2, we presented the results of simulations of nano-antennas illuminated with electromagnetic plane waves. We compared the numerically calculated optical cross sections with the semi-analytical results of the dipole model, in which we used numerically calculated polarizability. In this section, we show results obtained from numerical calculations of electron-energy loss spectroscopy performed in COMSOL, studying nano-antennas interacting with a focused beam of fast electrons. The EELS simulations are described in Appendix C.2.2. Firstly, we show that we can obtain the polarizability even from the EELS simulations in COMSOL, and then we employ the polarizability within the EELS dipole model. We follow the procedure described in [61], which is similar to the dipole expansion performed in FDTD using the MENP package. Albeit the methods should match, we want to compare the antenna polarizability obtained from COMSOL and how we can perform the dipole expansion with EELS and replicate the loss-probability spectra. We also want to evaluate the field enhancement of the antennas near-field. With the obtained polarizabilities and field enhancements, we will compare the performance of enhanced spectroscopies with photons and electrons in Chapter 4. We show the considered system in Fig. 2.8 (a).

As we have shown in Sec. 2.3.2, the field of the electron beam can induce a dipole moment in the structure. We can express the dipole moment from Eq. (1.42), where we assume that the induced charge is distributed as a charge density $\rho_\mathrm{ind,r}(\mathbf{r})$. In this manner, we can obtain the dipole moment by multiplying charge density at each point with the displacement vector $\mathbf{r}$ and integrating over considered volume Ω of the structure as

$$\mathbf{p}_\mathrm{car} = \int_\Omega \rho_\mathrm{ind,r}(\mathbf{r})\mathbf{r}\,\mathrm{d}^3\mathbf{r} = \frac{\mathrm{i}}{\omega}\int_\Omega \mathbf{J}_\mathrm{ind,r}(\mathbf{r})\mathrm{d}^3\mathbf{r}, \tag{2.33}$$

where we expressed the charge density with the induced current density $\mathbf{J}_\mathrm{ind,r}$. We also denoted "r" in the subscript to emphasize, that we deal with a cartesian electric dipole moment. In this expression, we assume the long-wavelength (quasistatic) approximation, where we neglect the ω-dependence of the induced currents, and assume that the wavelength of the electromagnetic field inducing the dipole moment is much larger than the

structure. Thus, all the charges in the structure experience the same driving field and are driven homogenously. For structures comparable in dimensions or even larger than the wavelength, retardation effects take part, and quasistatic approximation can not be used.

For comparison, we also use the implementation of exact multipole moment expansion into COMSOL, as is described in [61]. The electric spherical dipole moment can be expressed as [62]

$$\mathbf{p}_{\text{sph}} = \frac{i}{\omega}\left\{ \int_{\Omega} \mathbf{J}_{\text{ind,r}}(\mathbf{r}) j_0(kr) \mathrm{d}^3\mathbf{r} + \frac{k^2}{2} \int_{\Omega} \left[3\Big(\mathbf{r}\cdot\mathbf{J}_{\text{ind,r}}(\mathbf{r})\Big)\mathbf{r} - r^2 \mathbf{J}_{\text{ind,r}}(\mathbf{r}) \right] \frac{j_2(kr)}{(kr)^2} \mathrm{d}^3\mathbf{r} \right\}, \tag{2.34}$$

where $\mathbf{r}$ is the position vector with magnitude $|\mathbf{r}| = r$, $j_0(kr)$ and $j_2(kr)$ are the zeroth and the second order spherical Bessel functions, respectively[2]. We plot them spherical Bessel functions for three different values of r in Fig. 2.8 (b). We can see that depending on the r, and an energy region considered, the functions oscillate more rapidly. For the long-wavelength regime where $kr << 1$, we can break the approximate expression down into $\mathbf{p}_{\text{sph}} \approx \mathbf{p}_{\text{car}} + \mathrm{i}k\mathbf{T}_{\text{car}}$, where we recognize the cartesian electric dipole moment from Eq. (2.33), while the second term is the cartesian electric toroidal moment [62]. We can see that for the considered geometry of the hBN antenna and energies around 180 meV, $j_0(kr) \approx 1$, while $j_0(kr) \approx 0$ [Fig. 2.8 (b)], thus yielding $\mathbf{p}_{\text{sph}} \approx \mathbf{p}_{\text{car}}$. For gold antennas with dimensions in order of micrometres, we can see that the Bessel functions start to oscillate more rapidly, therefore the need for the calculation of the $\mathbf{p}_{\text{sph}}$ is necessary.

The induced current density can be directly obtained from COMSOL, where it is computed as

$$\mathbf{J}_{\text{ind,r}}(\mathbf{r}) = i\omega\varepsilon_0(\varepsilon_{\text{r}} - 1)\mathbf{E}_{\text{ind,r}}(\mathbf{r}), \tag{2.35}$$

where ε_{r} is dielectric function of the medium and $\mathbf{E}_{\text{ind,r}}(\mathbf{r})$ the induced electric field.

We can evaluate the polarizability $\overleftrightarrow{\boldsymbol{\alpha}}$ from Eq. (1.42) using the dipole moment $\mathbf{p}$. For this, we also need to evaluate the field of the electron beam which drives the dipole. We can obtain the field analytically from Eqs. (2.23-2.24) or directly from COMSOL as we described in Appendix C.2.2. We will be using the latter, albeit they match fairly well [C.3 (c)]. We assume that for this geometry of the beam-antenna-object system [Fig. 2.8 (a)] the polarization of the antenna is mainly in the x-direction, and we can then again consider just the xx-component of the polarizability tensor which we denote as $\alpha^{\text{A}}_{\text{xx}} = \alpha^{\text{A}}$. It is then calculated as

$$\alpha = \frac{p_x}{E_x^{\text{el}}(x^{\text{A}})}, \tag{2.36}$$

where E_x^{el} is the x-component of the electric field of the electron beam evaluated in the antenna center x^{A}, where the induced point dipole is located. We plot the cartesian and spherical polarizability obtained from Eqs. (2.33-2.34) for an hBN nano-antenna in Fig. 2.8 (c). We can see that the cartesian and spherical polarizabilities are indeed the same for the considered geometry and energy region. We also compare the polarizabilities obtained from COMSOL simulation, where the dipole within the nanostructure is induced

[2]The zeroth order spherical Bessel function is commonly known as the sinc function and yields expression $j_0(x) = \frac{\sin(x)}{x}$. Spherical Bessel function of the second order is $j_2(x) = \left(\frac{3}{x^2} - 1\right)\frac{\sin(x)}{x} - \frac{3\cos(x)}{x^2}$.

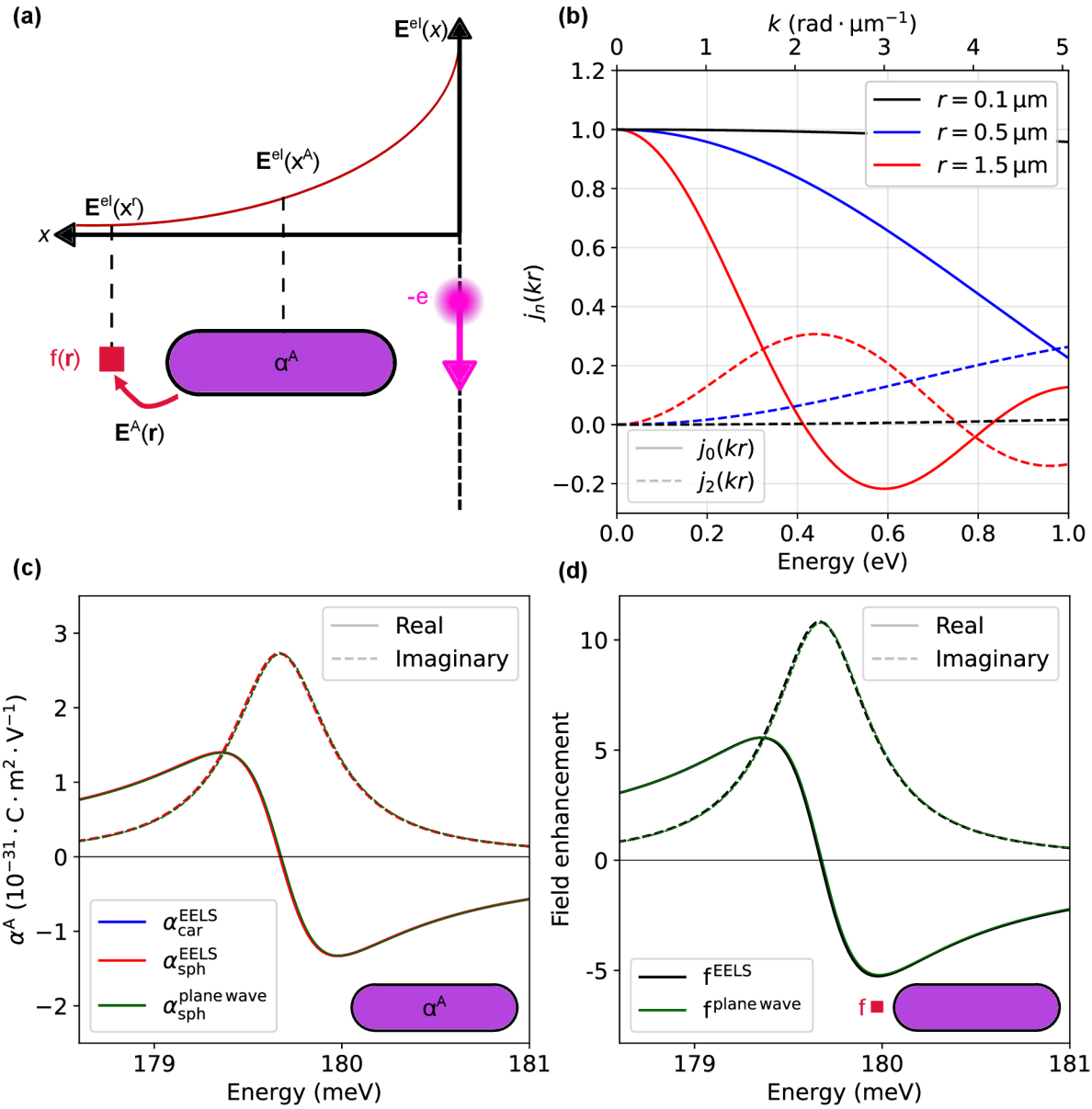

Figure 2.8: (a) Scheme of the considered geometry. An electron beam induces a dipole moment in the nanostructure. We evaluate field enhancement of the nanostructure at a point r. We assume that all polarization is dominantly in the x-direction. (b) The zeroth and the second-order spherical Bessel functions are plotted for three values of r. (c) Polarizability of a cylindrical hBN of antenna with hemispherical apexes (see inset) of radius 20 nm and length 120 nm. With blue lines, we plot the quasistatic (cartesian) polarizability obtained from the dipole moment computed in COMSOL after performing integration of currents induced by the field of the electrons (Eq. (2.33)). With red lines, we plot the exact (spherical) polarizability of Eq. (2.34). We can see that for the considered geometry and energies, the α_{car} is almost the same as α_{sph}. With green lines, we plot α_{sph} obtained plane-wave illumination of the same hBN nano-antenna for comparison. (d) Field enhancement evaluated 30 nm from the antenna apex. With the black line, we plot the field enhancement of Eq. (2.37) and with green line, we plot the field enhancement calculated by plane-wave illumination.

by the field of an electron beam, with polarizability obtained from a simulation, where we consider the nano-antenna illuminated by a plane wave. The methodology is described in Appendix C.2.1. We recognize that we obtain nearly the same values, confirming that the dipole expansion performed in EELS works fairly well.

In the following chapters, we discuss enhanced spectroscopic techniques, where an enhancement of a signal is caused by the field enhancement. For this reason, we also evaluate the field enhancement produced by a nano-antenna excited by an electron beam. At our x-position of interest x^{r}, where we want to obtain the field enhancement, we observe a superposition of the field of the electron beam and the induced field of the antenna, as schematically depicted in Fig. 2.8 (a). We can express the field enhancement from the field enhancement tensor. As we again suppose that xx-component prevails over all the others, we assume the scalar field enhancement denoted as $f = f_{xx}$. The incoming field inducing the dipole moment would be the field of an electron beam at the position of the center of the nano-antenna. From the simulations in COMSOL we are able to obtain the total field $E_x^{\mathrm{tot}}(x^{\mathrm{r}}) = E_x^{\mathrm{A}}(x^{\mathrm{r}}) + E_x^{\mathrm{el}}(x^{\mathrm{r}})$. The field enhancement can then be expressed from Eqs. (1.38-1.39) as

$$f_{xx}(x^{\mathrm{r}}) = \frac{E_x^{\mathrm{A}}(x^{\mathrm{r}})}{E_x^{\mathrm{el}}(x^{\mathrm{A}})}. \tag{2.37}$$

The field enhancement does not depend on the external source of the field, but only on the antenna polarizability and Green's function [see Eq.1.39], so it should be the same for the case of an antenna dipole excited by a plane electromagnetic wave or by the field of a focused electron beam, which is confirmed in Fig. 2.8 (d).

Now, we show the results of simulations of electron energy-loss spectroscopy in COMSOL. We again assume hBN nano-antenna, of the same shape and dimensions as in the simulations of plane-wave illumination [Fig. 2.6 (a)]. We consider the electron beam to be positioned at $x = 400\,\mathrm{nm}$ from the antenna center (340 nm from the antenna apex) with velocity of $0.446c$ (Tab. D.1). We plot the loss probability spectrum, obtained by calculating Eq. (C.7). We plot the calculated EEL spectrum in Fig. 2.9 (a). We can compare the EEL spectrum with optical cross sections of the same antenna [Fig 2.6 (a)], after which we can see that we again obtain resonance peak at the resonance energy 179.7 eV (wavelength 6.9 µm), which gives us information about the energy loss of the electron due to inducing a resonance within the nano-antenna.

As we have shown in Sec. 2.3.2, we can also compute the loss probability due to an induced dipole. We again assume that the antenna is polarized in the x-direction (we again replace the polarizability tensor by the xx-component and write $\alpha_{xx}^{\mathrm{A}} = \alpha^{\mathrm{A}}$). Eq. (2.31) for the dipole model then becomes

$$\Gamma_{\mathrm{EELS}}^{\mathrm{A}}(\omega) = \frac{1}{\pi\hbar}\mathrm{Im}\Big\{E_x^{\mathrm{el},*}(x^{\mathrm{A}})\alpha^{\mathrm{A}}E_x^{\mathrm{el}}(x^{\mathrm{A}})\Big\} = \frac{1}{\pi\hbar}\big|E_x^{\mathrm{el}}(x^{\mathrm{A}})\big|^2\mathrm{Im}\big\{\alpha^{\mathrm{A}}\big\}. \tag{2.38}$$

For the evaluation, we can use the cartesian or spherical polarizabilities obtained from COMSOL [Fig. 2.8 (c)]. We plot the spectra calculated with different polarizabilities in Fig. 2.9 (a) and compare them with the EEL spectrum calculated via Eq. (C.7). In Fig. C.3 (e), we can see that the relative error is under 2% for the cartesian polarizability and about 1.5%. for the spherical.

We now show how the loss probability maximum (acquired at resonance as highlighted in Fig. 2.9 (a) with the vertical dotted line) depends on the impact parameter (the distance

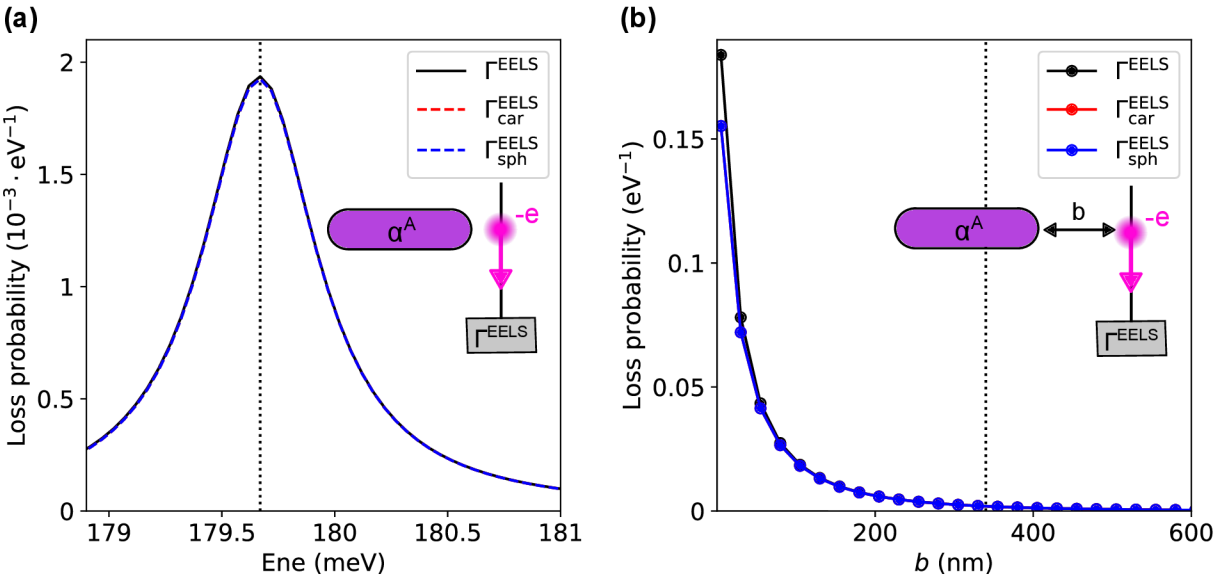

Figure 2.9: (a) Simulated EEL spectra of an hBN nano-antenna (diameter $D = 40\,\text{nm}$ and length $L = 120\,\text{nm}$). The electron beam is positioned 340 nm from the antenna apex. With the black line, we plot the spectrum calculated from Eq. (C.7), obtained by integrating the field induced by the nano-antenna along the electron trajectory. With red and blue lines we plot loss probability obtained from Eq. (2.38), into which we plugged computed dipole moments $\alpha^{\text{A}}_{\text{car}}$ (red dashed line) and $\alpha^{\text{A}}_{\text{sph}}$ (blue dashed line) respectively. With the dotted line, we denote the energy of the dipole resonance. (b) Loss probabilities at the energy of the dipole resonance were evaluated for different impact parameters b of the electron beam. We can recognize that near the antenna, the dipole model stops being valid. With the vertical dotted line we mark the values from (a).

of the electron beam and the nanostructure). In Fig. 2.9 (c), we plot the numerical results, starting with impact parameter 5 nm from the antenna apex (e.g. 65 nm from the center) until 605 nm. We can see that according to Eq. (2.23) the electric field of fast electrons decreases with distance. As the field induced within the nanostructure, from which we calculate the loss probability, depends on the external field, we can see that the loss probability decreases rapidly for larger impact parameters. For the largest EELS signal, it is thus beneficial to have the beam as close to the nanostructure as possible. In Fig. 2.9 (c), we again compare the loss probability obtained from Eq. (C.7) with the one calculated using the model of the loss probability for an induced dipole in Eq. (2.38). We can see that the loss probabilities of the induced dipole are smaller compared to the numerical simulations. In Fig. C.3 (f), we recognize that the relative error is about 20% when the beam is posistioned 5 nm from the antenna tip and then decreases. The error could be caused by the limits of the dipole approximation, as we are assuming that the dipole is induced at the center of the nano-antenna. If the beam is too close, because of the strong and rapidly changing field, the dipole becomes distorted. Also, higher-order modes could get excited and cause signal distortion due to partial spectral overlap with the dipolar mode.

With these results, we conclude this chapter. We showed that we can obtain polarizabilities of nanostructures and near-field distributions in their vicinity, from simulations of both plane-wave illumination and electron beam excitation. We will use these quantities in Chapter 4 for model of the enhanced spectroscopies.

3 Vibrational spectroscopy

Infrared (IR) spectroscopy is a powerful tool for studying molecular samples active in the IR region. Molecules support vibrational resonances, which are in the IR region, and by finding out the energy of such resonance, we can distinguish vibrations and describe our sample. From them, one can obtain information about constituents present in the sample, their configuration, and the chemical bonds between them [1]. The obtained spectral information can be used in the study of organic and inorganic molecules [63], analysis of polymers [64]l, and for applications in medicine, for example for diagnosing of cancer [65, 66, 67]. Applications in very different fields are also plausible, revealing counterfeit paintings [68], examining the age and the degradation of heritage items, such as paintings and statues [69] or even gaining and studying forensic evidence in crimininal investigations [70].

In the following chapter, a brief overview of IR spectroscopy and adjacent techniques used for the study of organic molecules is described. We then focus on surface-enhanced infrared spectroscopy (SEIRA) and the possibility of studying vibrational samples with focused electron beams.

3.1 Infrared and visible spectroscopy techniques

From quantum mechanics, we get very important results regarding the energy of a quantum system. The energy, of, for example, electrons, bound in atom shells is discretized and can have only certain values E_n, where n is a positive integer. In the equilibrium, all of the electrons are in the ground state, but when energy is added to the system, for example, in the form of an absorbed photon of energy $E = \hbar\omega$, the electrons can be excited to higher-energy states E_{n+1}, on which they can stay or from which they can relax back while emitting the energy. Only certain transitions are allowed, the absorbed energy must overlap with the difference between two states, and many selection rules govern the possibility of transition.

The transition from one energy state to another can be induced in many ways. We mentioned the excitation of electrons to a higher energy state and the subsequent radiative decay of the excited electrons, luminescence. In the previous chapter, we introduced cathodoluminescence, which is a luminescent process induced by an electron beam. When a photon induces the transition, we talk about photoluminescence. Based on the decay time (time between absorption of photon and emission of the new one), we can divide photoluminescence into two regimes. The first one is fluorescence, where the photon is emitted almost immediately (typically about 10^{-6} s and shorter) after the absorption, the second is phosphorescence, where the lifetime can be in the units of seconds or longer [71]. Fluorescence microscopy is often used to study organic molecules, either the ones that show autofluorescence or by using markers (fluorophores) that connect to certain parts of particular molecules [72]. From the measurement, we can obtain the lifetime of the excited states [73], and it can also provide information about the concentration, mobility, or configuration of the molecules. The mechanism of fluorescence is shown in the energy diagram in Fig. 3.1. Impinging photon is absorbed by the sample and its energy $\hbar\omega$ is given to the electron and raises it from the ground state S_0 to a higher electronic band S_1. It can then relax by non-radiative processes, going to a lower vibrational state

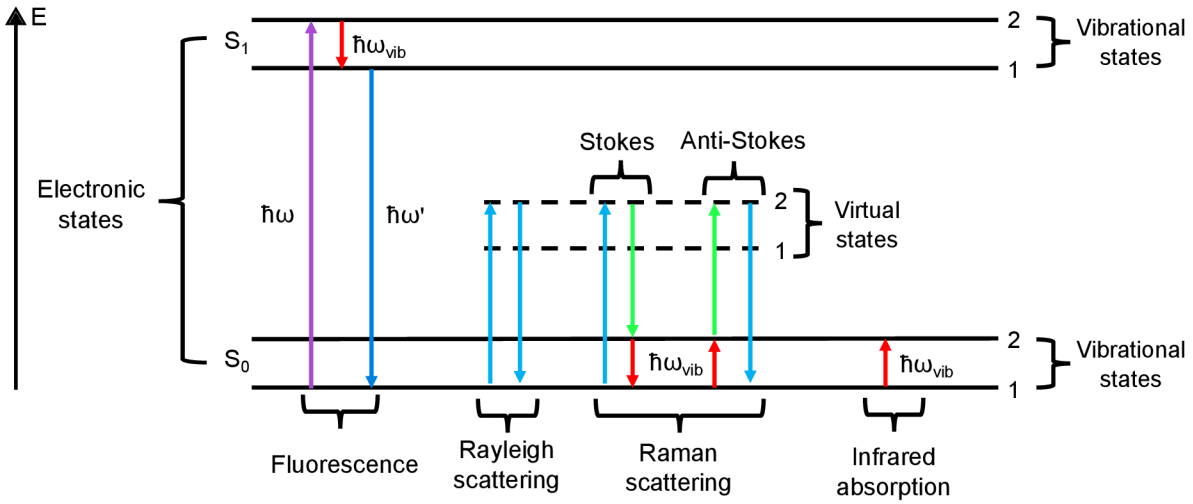

Figure 3.1: Jablonski diagram representing transitions of electrons between discrete energy states. When a photon induces the transition between two electronic states, we talk about fluorescence. If we consider scattering, when the polarization state of our sample can be changed, and new, short-lived virtual states can emerge for electrons, we talk about Rayleigh (elastic) and Raman (inelastic) scattering. Transition between two vibrational states is called the infrared absorption, because of the energy of the transition.

and giving energy $\hbar\omega_{\text{vib}}$ to molecular vibration or phonons in solid matter. After the relaxation, the electron goes back to the ground state, and a visible photon of lower energy $\hbar\omega' = \hbar\omega - \hbar\omega_{\text{vib}}$ is emitted. Because the fluorescence is based on electronic transitions, the emitted photon energies typically correspond to the visible spectral range. When considering absorption processes, photon impinging on studied sample needs to have exactly the energy of the difference between two energy levels to be absorbed and we gain the information about the studied sample from the absorbed photons. That is not the case for scattering spectroscopy, where we can study the change in energy of photons re-emitted after absorption. Raman spectroscopy is one of the most common scattering techniques for examining vibrational sample response. Fig 3.1 schematically shows three cases of scattering, where an electron can be raised to a virtual energy state after absorbing a photon. Such virtual energy states have short lifetimes [75]. After the decay of the electron back to the real electronic state, a photon is emitted. The first case of the scattering is Rayleigh (elastic) scattering, where the radiated photon has the same energy as the photon which induced the transition. Inelastic processes in this scenario are called Raman scattering. Electron, after being raised to the virtual state, can relax back into a higher-energy vibrational state, than where it was before, thus the emitted photon has a smaller energy. Such energy discrepancy is labeled as the Stokes shift. If the electron is already excited from the higher vibrational state, after being raised to the virtual state and the relaxation, it can relax to the ground state. The radiated photon then has a larger energy, and the energy shift is labeled as the anti-Stokes shift. Because of the condition of already excited electrons, of which the majority are in the ground state at room temperature, the anti-Stokes shift peak in spectra is typically less intense than the Stokes one. We can see a typical Raman spectrum in Fig. 3.2 (a). The quantity on the x-axis of Raman spectra is typically labeled as the Raman shift, meaning the change in photon energy compared to the source photons.

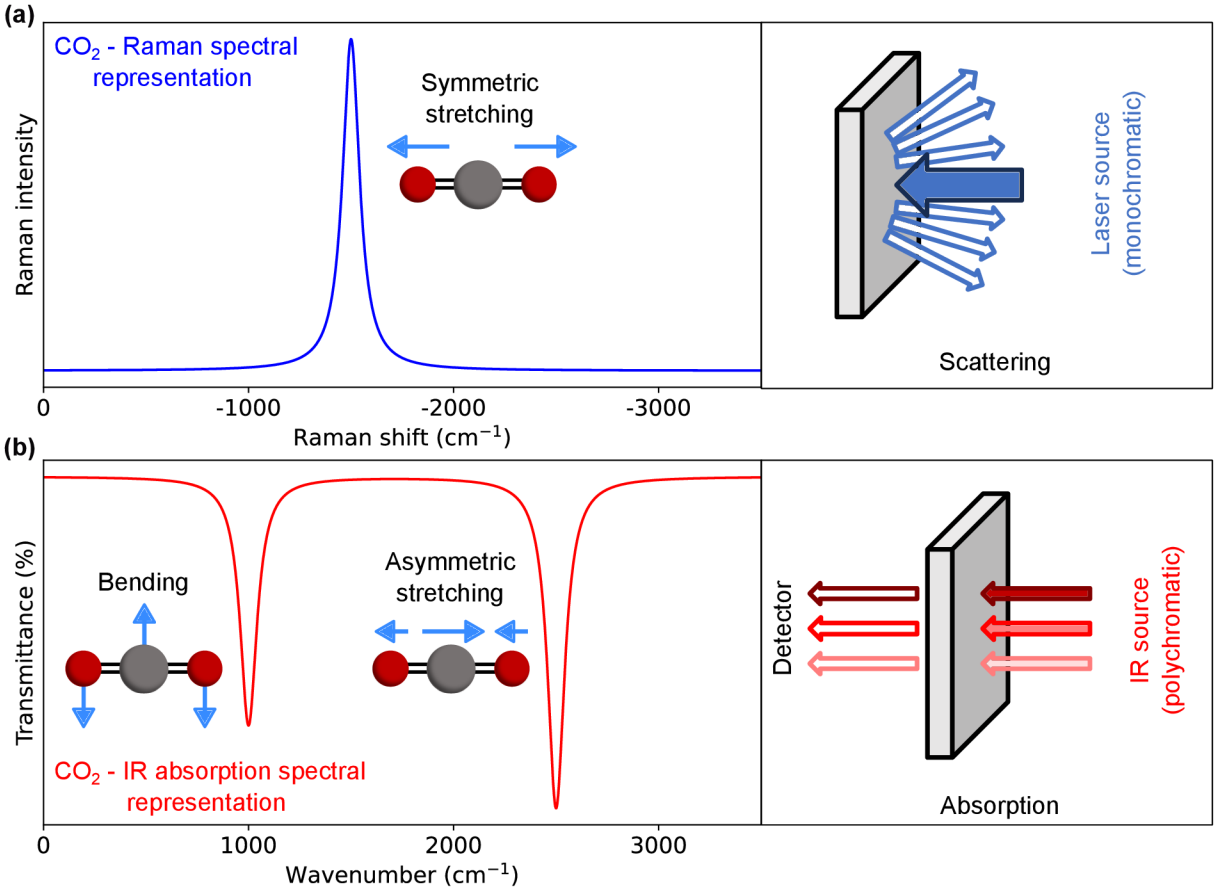

Figure 3.2: Comparison of (a) theoretical Raman spectroscopy spectrum (sensitive to changes of the sample polarizability) and (b) transmittance spectrum for obtaining infrared (IR) absorption (sensitive to the change of the dipole moment in sample) for CO_2 molecule. In Raman spectroscopy, we illuminate the sample with a monochromatic photon source (e.g. laser) and measure the shift of the frequency of emitted photons due to inelastic scattering. We can see that the Raman peak corresponds to the excitation of symmetric stretching mode, where the total dipole moment is zero, but the polarizability is changing. In IR absorption, we illuminate the sample with a polychromatic IR source and study absorption on different frequencies, we can see that the two dips correspond to the excitation of vibrations depicted on the schemes, for which the dipole moment of the molecule is changing. Inspired by Ref. [74].

When investigating samples with infrared light, we can directly induce vibrational transitions. With the photons of the energy corresponding to the transition energy missing from the measured spectra, we can tell which transitions took place. This infrared absorption process is again depicted in Fig. 3.1. Infrared absorption measurement is most commonly performed as a transmission experiment, for example, in Fourier transform infrared spectroscopy (FTIR). A typical transmittance spectrum is shown in Fig. 3.2 (b), where we can also see the complementarity of IR absorption and Raman spectroscopy. Different vibrations can have different symmetry, resulting in change of either the polarizability of the sample or its dipole moment. Raman scattering is sensitive to the change of the polarizability during vibrations, and infrared absorption is sensitive to the changes in the dipole moment [1], which makes both techniques useful for different vibrational resonances.

3.2 Surface-enhanced spectroscopies

One of the main advantages of Raman spectroscopy and IR absorption spectroscopy is that both techniques are label-free and non-destructive, which makes them ideal for studying even sensitive molecular samples. One particular problem arises when one deals with small amounts of analyte. Both spectroscopies suffer from the subsequent loss of the signal, which can be lost in the noise during the measurement. This hindrance can be overcome by placing our sample into a strong near field (e.g. near a resonant nano-antenna), which can be because of their evanescent nature strongly enhanced, as we discussed in Sec. 1.5. resulting in the detected IR vibrational signal being magnified significantly.

In a 1974 article, Fleischmann et al reported an unusually large Raman signal of organic molecules adsorbed on a rough metallic layer [76]. This new spectroscopic method was labeled as surface-enhanced Raman Spectroscopy (SERS), as it was carried out on a rough planar surface. Many contributed to the explanation of this phenomenon and successfully attributed it to the electromagnetic effect of the near field produced by the substrate roughness and also to the chemical effect [77], which arises due to the chemical interactions between the sample and a metallic surface. The signal enhancement factor of SERS, defined as the ratio between the enhanced signal and the sole sample signal, was estimated to be maximally about 10 orders of magnitude [78].

Just six years after the first observation of SERS, a similar enhancement of the signal was discovered for infrared absorption, and surface-enhanced infrared absorption (SEIRA) was founded [79]. Similarly to SERS, the enhancement in SEIRA strongly depends on the surface morphology and the material used. These enhancements were reported as about 1-3 orders of magnitude. This phenomenon was later re-labeled as non-resonant SEIRA[1]. For the case of randomly sized and placed islands on the surface, the distribution of the resonances contributing to the IR extinction/transmission merges into a smooth background. Such background provides a signal enhancement for a large region of the IR spectrum. On the other, only some of the particles have resonance and ensuing maximal field enhancement at the particular energy of the vibration. The independence of the signal enhancement on the energy can be helpful in some applications, particularly when looking at broader spectral ranges, with molecules with many resonances. The contributing effects were again identified as the electromagnetic and chemical effects [80].

In 2008, Neubreuch et al. showed, that much greater signal enhancement is obtained when one uses arrays of nanostructures of the same size and shape, which all support resonance on the same energy, as the molecular vibration [7]. Such nanostructures can be, for example, nano-antennas described in Sec. 1.5, and they labeled this enhancement process as the resonant SEIRA. This effect can be viewed as a mere consequence of the spectral dependence of the near-field magnitude of the nanostructure, which has been

[1] Few words shall be said about the nomenclature of the surface-enhanced techniques. As they were first observed on rough metallic surfaces, the enhancement origin was assumed to come from the rough surface, thus the label as surface-enhanced. A similar enhancing phenomenon was reported in the presence of a sharp metallic tip, for example, for tip-enhanced Raman spectroscopy (TERS). Both of these mechanisms take the main advantage of the same physical process, which is the magnification of the signal caused by the presence of the near field produced by nanostructures. We will talk about the origin of the signal enhancement in the next section. The label to be suggested could be generally the field-enhanced spectroscopies, but in the rest of this thesis, the classic nomenclature of "surface-enhanced" will be used for the enhanced infrared absorption.

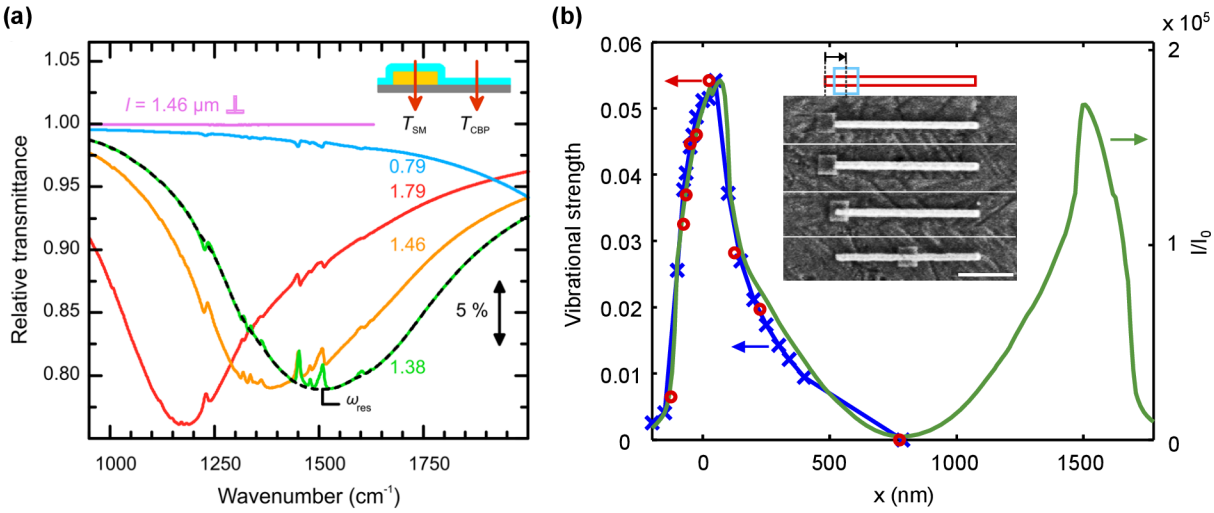

Figure 3.3: (a) Relative transmittance spectra of nano-antenna arrays covered by a molecular layer. Different colors correspond to different nano-antenna lengths, as can be seen from the shift of the resonance peak. Peak (dip) features can be observed in the broad plasmonic peaks, giving us an enhanced signal of the molecular layer. Depending on the tuning of the antenna resonance (extremes of the broad plasmonic peaks) to the energies of the molecular vibrations, different strengths of the enhancement were observed. The light was polarized in accordance with the long antenna axis in all cases except for the pink curve. In that case, polarization is perpendicular, thus the dipolar resonance is not excited and there is no enhancement of the signal. This curve then factually represents the response of the bare molecular layer. Adapted from [4]. (b) Experimentally measured vibrational signal strengths (magnitudes of the molecular features) for nano-antennas of length approximately 1500 nm (red-dots) for different positions x of the molecular sample (narrow deposited patches) at the nano-antennas. With the blue line, simulated vibrational strengths are plotted. With the green line, numerically calculated near-field intensity enhancement dependence on the x-position is plotted. Adapted from [81].

shown, that it is the largest near its resonance [37], and we discuss the role of the field enhancement in SEIRA in the next chapter.

In Fig. 3.3 (a), we can see how the resonance tuning influences the signal enhancement. Transmittance spectra of nano-antenna arrays with four different lengths, which were illuminated by light polarized in the respect of the long antenna axis, so the dipolar resonance was excited, are plotted. The enhanced molecular signature grows stronger as it is closer to the antenna resonance. Because of the spectral dependence of the field enhancement, we can also see that even the off-resonance molecular signatures are enhanced slightly. For comparison, the same array of nano-antennas of length 1.46 μm was illuminated by light polarized perpendicularly to the antenna axis, so the longitudinal dipole was not excited and no enhanced signal arose. Such a vanishing signal would be obtained from the standard transmittance experiment without the nano-antennas.

Scaling of the signal enhancement also depends on the location of the molecular sample and the near-field distribution. In Fig. 3.3 (b) the magnitude of the enhanced vibrational signal is plotted for different positions of the molecular sample in regards to the nano-antenna. This was achieved by considering tailored molecular patches placed at different antenna positions. With the green curve on the second axis, the field enhancement squared (near-field intensity divided by the incoming light intensity $f^2 = I/I_0$) is plotted. We can

see that the strength of the signal depends on the field enhancement squared and we obtain the largest signal for samples positioned near the tip of the nano-antenna, where at the dipolar resonance, the field is the largest [Fig. 1.3 (c)].

3.3 Infrared spectroscopy with focused electron beams

While infrared absorption spectroscopy can give reasonable spectral information about the sample, and with the field enhancement, we are able to study minute amounts of analytes, spatial information often gives us another valuable degree of freedom. With standard light-based spectroscopies, discussed in previous sections, the spatial resolution is diffraction-limited, therefore yielding micrometer spatial resolution in infrared [82]. The desired signal of the studied sample can also be lost in the background signal, obtained after illumination of a large area [(Fig. 3.4 (a))]. Albeit by introducing a sharp metallic tip [Fig. 3.4 (b)], in scanning near-field optical microscopy, the diffraction limit can be suppressed and spatial resolution can be in order tens of nanometers [83]. Electron energy-loss spectroscopy (EELS) performed in scanning transmission electron microscope (STEM) with a localized electron probe, described in Sec. 2.3, however, yields much better spatial resolution compared to the light-based techniques [(Fig. 3.4 (c))]. Spectroscopic information of individual atoms can be obtained [84, 85].

Until recent years, the STEM-EELS was confined only to near-infrared and higher energies regions, where it was not possible to study for example molecular vibrations, IR plasmons and phonons, which are typically situated in regions below 500 meV. The restrictions arose mainly due to insufficient technological equipment. With the recent development in TEM instrumentation, particularly in the monochromators, cold field emission electron guns, and spectrometers, the feasibility of performing infrared measurement appeared [58]. The FWHM of the zero-loss peak was narrowed down to a few tens of meVs [Fig. 3.4 (d)]. On the other hand, one major problem that emerged while studying organic vibrational samples is beam-induced damage. The sample can be degraded either by direct irradiation of the field of the electron beam, by the bombardment, heating, charging, and other processes [86, 87].

Several recent studies showed that by exploiting the feasibilities of state-of-the-art transmission electron microscopes, EELS of sensitive vibrational samples is possible [89, 90, 91]. Probing low-energy excitations in for example hexagonal boron nitride [Fig. 1.2 (c)] is nowadays accessible in EELS [18]. Liquids and liquid interfaces, play a central role in many research fields. Recently, a novel approach to studying liquids in STEM-EELS by encapsulating water between two thin sheets was shown. Stretching of the O-H phonon of water at approximately 400 meV was detected [(Fig. 3.4 (e))], changes of the structure of water near solid surface, solidification fronts and different isotopes were studied [88].

Similarly to light-based vibrational measurements, when examining small amounts of analytes by EELS, the signal can be hindered behind the background noise and lost. As was proposed by Konečná et al [55], and was also discussed in Ref. [92], surface-enhanced molecular EELS can be the way to overcome this [(Fig. 3.4 (f))]. Similarly to SERS and SEIRA, the molecular signal is enhanced by the presence of a strong near field generated e.g. by a nano-antenna.

We now recapitulate some results from Ref. [55]. In Fig. 3.4 (g), we can see spectra for a silver plasmonic nanorod and in Fig. 3.4 (h) spectra for a hexagonal boron nitride

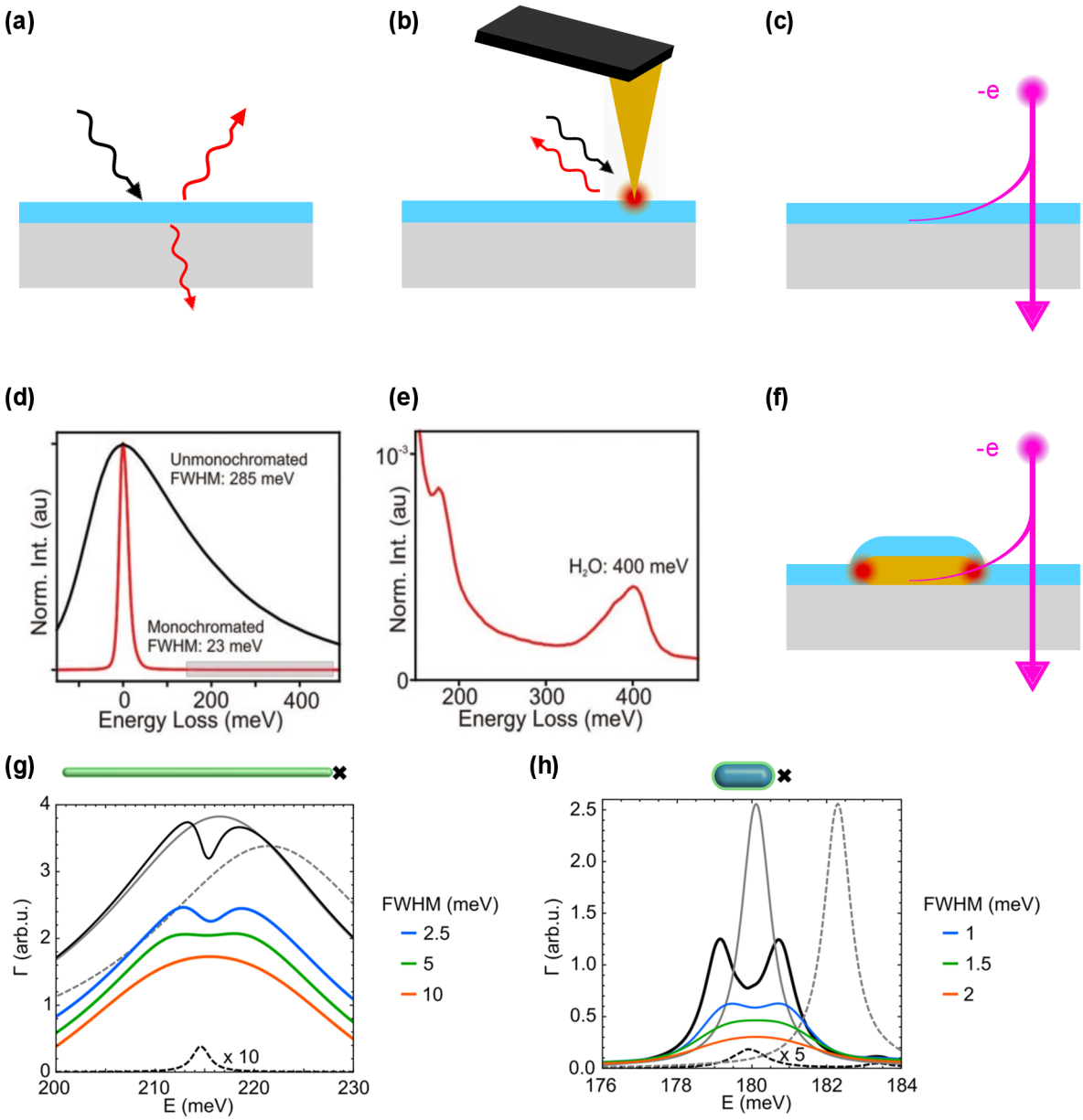

Figure 3.4: (a) Standard photon-based IR measurement. The sample layer (blue) is placed on the substrate (gray). The light gets either absorbed or scattered by the sample and we can then measure the transmitted or reflected intensity. (b) Scanning near-field optical microscopy, utilizing a metallic probe, The sharp tip can localize the incoming electromagnetic field in its vicinity. (c) Electron energy-loss spectroscopy utilizes a focused beam of fast electrons. The electron can interact inelastically with the sample and lose some energy, which can then be quantified. (d) Comparison between experimental zero-loss peaks obtained with an unmonochromated electron beam (black) and with a monochromated one (red). (e) With the monochromated beam, much better energy resolution can be achieved, enabling the detection of vibrational signals. (f) Scheme of field-enhanced electron energy-loss spectroscopy. The electron beam induces a resonance within the nano-antenna, which then interacts with its strong near-field with the studied sample. (g) Numerically calculated EEL spectra of a silver nanorod covered by a layer of PMMA. Different zero-loss peak FWHMs are considered. (h) Numerically calculated EEL spectra of a hBN nanorod. (d-e) Adapted from Ref. [88]. (g-h) Adapted from Ref. [55].

phononic nanorod obtained from numerical simulations. The silver nanorod was covered by poly(methyl methacrylate) (PMMA). In the paper, they approximated the response of the PMMA by a carbonyl (C=O bond) stretching at about 215 eV. With the gray dashed line, bare silver nanorod spectra are plotted. When the nanorod is covered by a layer characterized by the background permittivity of the PMMA, we can see that the resonance is red-shifted. With a black line the simulated spectrum, where we can see that the molecular feature is present, caused by the interaction between the antenna field and the molecules. We can recognize that the molecular features are similar to the ones obtained by photon-based SEIRA [Fig. 3.3 (a)]. The signal of the sole molecular shell is plotted with the black dashed line and multiplied by a factor of 10 for better visibility. The simulated spectra were then convolved with a Gaussian curve, approximating the broadening of the spectra in the experiment and mimicking instrumental resolution. As we can see in the figure (spectra were scaled and vertically shifted for better visibility), the degree of monochromation matters greatly, as for broader ZLP the molecular features start to disappear.

The hexagonal boron nitride antenna was functionalized with a CBP. The dashing and color legend is kept the same as in Fig. 3.3 (g). We can see that the the peak, which informs us about energy lost due to the excitation of localized phonon polariton resonance, is much narrower than the plasmon in silver. Compared to the molecular feature in the plasmonic peak of the silver nanorod, which is in the form of a weak perturbation, splitting occurs, and two hybridized modes emerge in the case of the hBN antenna coupled to the molecular layer. Nevertheless, the consequent convolution with a Gaussian curve showed, that for the molecular feature to be observable, the FWHM of the zero-loss peak would need to be below 1 meV, which is not yet achieved even in the state-of-the-art systems.

With EELS, ultra-remote sensing was proposed. The electron beam is considered to be positioned at one end of the nano-antenna, while the molecular sample is covering the other end. With this, after the beam interacts with the nano-antenna, in which it can excite a resonance. The near-field then interacts with the molecular sample on the other end, which acts back on the antenna, changing its response and providing enhanced spectral information about the sample. Ultra-remote sensing could be beneficial regarding the sample degradation caused by the direct interaction with the electron beam, as the only damage would come from the strong near-field generated in the vicinity of the tip of the nano-antenna.

Several other aspects, such as coupling of the molecular resonance with the higher-order modes within the nano-antennas, which can be directly probed by the electron beam, the decay of the signal regarding the distance of the beam, and evaluation of the strong coupling, were also studied in Ref. [55].

In Ref. [92], semi-infinite foil and some other shapes of nano-structures (oblate spheroid, sphere, prolate spheroid, and cylinder) were theoretically studied in the context of surface-enhanced EELS. By modeling the response of the antenna-molecule system, the proportionality of the enhanced signal on the square of the electric field acting on the molecules, similarly as in SEIRA. Signal enhancements in order of hundreds or even thousands were predicted using the formalism, showing the possibility of studying vibrational samples in STEM-EELS with unprecedented sensitivity.

4 Enhanced spectroscopy with photons and electrons

In contrast to the previous interpretations of SEIRA, where the molecular scattering was neglected, for example, in [47] it was shown, that the molecular signature appears even in the scattering cross-section. This goes against the previous interpretation of SEIRA as uniquely an absorption process, where the molecular scattering is neglected, due to the small amounts of the analyte and, therefore small scattering cross sections. SEIRA was already discussed in terms of coupled dipoles in Refs. [9, 10]. From the coupled dipole formalism, we are able to obtain molecular signatures in SEIRA as a consequence of an interference process. In this study, we continue in modeling SEIRA via model from Ref. [11] where SEIRA was explained by means of elastic light scattering between the antenna and the object, yielding the interference. We also explore the similarities of the molecular signatures appearing in SEIRA spectra and the ones in the surface-enhanced EELS and continue in work begun in Ref. [55]. We also establish several figures of merit, with which we can design optimal nano-antenna for enhanced spectroscopy experiments regarding the type of the collected signal, and emphasize, that for both electrons and light, we obtain similar equations and results.

4.1 Enhanced molecular absorption

Firstly, we focus on plane-wave illumination, and for the simulations of SEIRA, we choose golden round-rod antennas with hemispherical apexes aforementioned in Sec. 2.2.2. For the molecular sample, we choose polydimethylsiloxane (PDMS) molecules. As we consider a study of a small amount of the molecules, we approximate the sample by a 20 nm diameter sphere located in the vicinity of the antenna apex. We define the sphere with the Lorentz model of Eq. (1.44) with one oscillator, mimicking Si-CH_3 vibration at approximately 0.157 eV. We assume that the sphere is isotropic and its response is characterized by a quasistatic polarizability α^{O} from Eq. (C.1). We plot the dielectric function of PDMS and polarizability of the PDMS nanosphere in Fig. 4.1 (a).

To simulate the SEIRA experiment, we performed FDTD calculations of a system consisting of a nano-antenna and two nanospheres, as described in Appendix C.1. The nanosphere's centers are located 30 nm from each apex of the nano-antenna. We consider the same gold cylindrical nano-antennas, with hemispherical caps at the ends that were described in Sec. 2.2.2, where we calculated optical cross sections of the bare antenna. To obtain the signatures of the molecular sample in the antenna cross sections, we performed simulations with an object characterized by the Lorentz dielectric function from the Eq. (1.44) and labeled it as "resonant particle" (RES) simulation. By subtracting simulations of the antennas without resonant nanoparticles from the simulations of antennas coupled with resonant nanoparticles, we obtain the molecular signatures $\Delta\sigma$. Molecular signatures yield the baselined feature in the spectra caused by the presence of the object. To obtain molecular signatures, we can take two approaches: (1) we subtract simulation with the object characterized with $\varepsilon_{\mathrm{r}} = 1$, which we label as "no particle" (NP). We plot the difference in Fig. 4.1 (b) with the dashed line. Because of the background molecular permittivity, the simulation with the resonant object is redshifted against the

NP simulation. We see that this redshift distorts the lineshape, and instead of just the dip, we obtain a complex lineshape resembling a Fano shape. For the other case (2), we consider simulation with an object defined by the background permittivity of the PDMS $\varepsilon_\mathrm{r} = \varepsilon_\infty$ and we label this simulation as "background" (BG). Because of the background permittivity, the antenna cross sections are red-shifted. We then subtract BG from the RES simulation, after which we obtain a lineshape in the simple form of a dip. From now on, we will use baselined spectra obtained by subtracting BG simulation for easier interpretation to avoid the redshift distortion of the lineshape.

We consider plane wave illumination of the antenna-object system, with x-polarized electric field $\mathbf{E}^\mathrm{inc} = E^\mathrm{inc}\hat{\boldsymbol{x}}$. The antenna's long axis is oriented with respect to the x-axis [inset sketch in Fig. 4.1 (c)]. The response then depends on the xx-component of the polarizability, which we will denote simply as $\alpha^\mathrm{A} = \alpha^\mathrm{A}_{xx}$. We plot α^A for the model-case gold nano-antenna from Fig. 2.4 in Fig. 4.1 (c). The polarizability is generally a complex quantity, and we can write $\alpha^\mathrm{A} = \left|\alpha^\mathrm{A}\right|\mathrm{e}^{\mathrm{i}\arg(\alpha^\mathrm{A})}$. As we can see in Fig. 4.1 (c), at the resonance frequency of the molecule ω_res, the polarizability of the antenna is purely imaginary, so we can write $\arg(\alpha^\mathrm{A}(\omega_\mathrm{res})) = \pi/2$. We will later use this equality for simplification of terms in the SEIRA analytical model.

We also consider that the field enhancements near the antenna apexes are the largest in the x direction. We then assume $\left|f_{xx}\right|$ would be the dominant contribution among all the others and simply denote $f = f_{xx}$. We obtained the field enhancements for nano-antennas from the FDTD simulations as we describe in Appendix C.1. From Eq. (1.39), we can see that the field enhancement depends on the polarizability. We plot the field enhancement f at 30 nm from the antenna apex (where the center of the nanosphere is located) with crimson lines in Fig. 4.1 (c). There is a clear similarity between the spectral dependence of the polarizability and the field enhancement. The field enhancement is a complex quantity and reads $f = \left|f\right|\mathrm{e}^{\mathrm{i}\arg(f)}$. We can again see in Fig. 4.1 (c), that at the molecular resonance, field enhancement is purely imaginary, which yields $\arg(f(\omega_\mathrm{res})) = \pi/2$.

As we discussed in Chapter 3, and as the name states, surface-enhanced infrared absorption was assumed to be an absorption process. When considering small absorbing molecular samples, the scattering is negligible because of the weak polarizability and small dimensions of the samples. The whole contribution to the molecular extinction is then from the absorption. In the extinction spectra of the SEIRA system, a magnified signature was identified and attributed to the field-enhanced object absorption cross section as it scaled with $\left|f\right|^2$ [4, 81] which was demonstrated in Fig. 3.3. The magnitude of the dip was also assumed to be negative of object absorption cross section (the scattering cross section of a small object is negligible; absorption cross section is then the unique contributor to the extinction) multiplied by the square of the field enhancement amplitude $\left|f\right|^2$:

$$\sigma^{\mathrm{O,enh}}_\mathrm{abs} = \left|f\right|^2\sigma^\mathrm{O}_\mathrm{abs} = \left|f\right|^2\frac{k}{\varepsilon_0}\mathrm{Im}\{\alpha^\mathrm{O}\}. \tag{4.1}$$

In the FDTD calculations of the antenna-object system, we placed an absorption monitor around the object [inset in Fig. 4.1 (d)]. With this monitor, we obtained the absorption cross section, which is enhanced by the antenna near-field. We plot the enhanced object absorption in Fig. 4.1 (d) and compare it with enhanced absorption obtained from the Eq (4.1). We used quasistatic object polarizability and field enhancement at the point of the object center, plotted in Fig. 4.1 (a) and (c), respectively. We can see that the analytical formula predicts the enhanced absorption fairly well, even by using the quasistatic

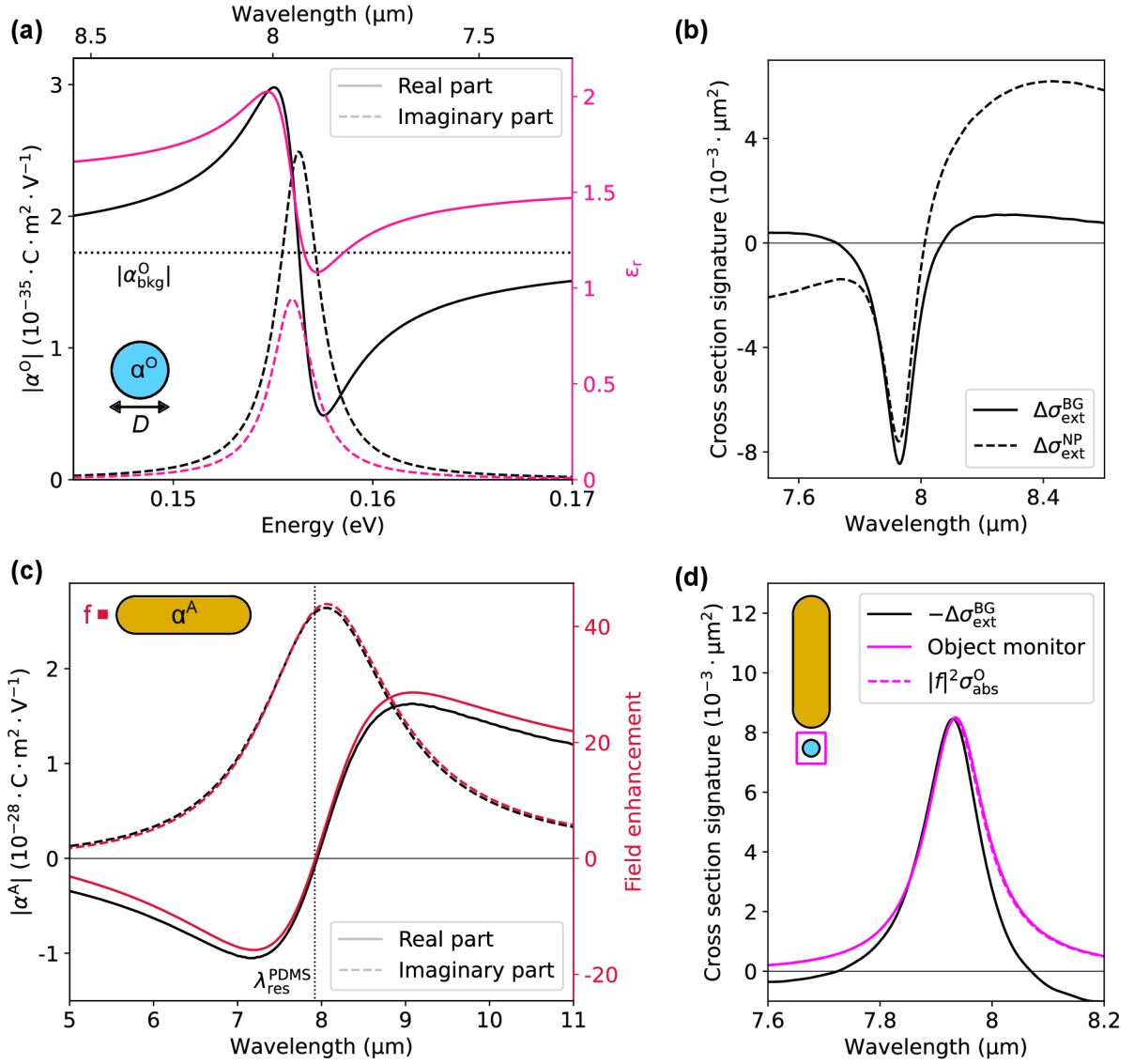

Figure 4.1: (a) Quasistatic polarizability of a nanosphere (black line), obtained from Eq. (C.1). The nanosphere has a diameter $D = 20\,\text{nm}$ and is characterized by PDMS dielectric function (pink lines). We can see the resonance of Si-CH_3 at about 0.157 meV, for which we used Lorentz model from Eq. (1.44) with parameters $\varepsilon_\infty = 1.55$, $F_1 = 364.838\,\text{meV}^2$, $\omega_{0,1} = 155.957\,\text{meV}$ and $\gamma_1 = 2.480\,\text{meV}$. With the dotted line, we plot the background polarizability α^O_∞ of the same sphere from Eq. (C.1), characterized just by $\varepsilon_\infty = 1.55$. (b) Baselined extinction cross section, bearing information about the molecular signature in two cases: (1) after subtraction of the simulation of a bare golden antenna with no object (NP) and (2) after subtraction of simulation with a sphere characterized by the background polarizability α^O_∞ (BG) from the simulation of the golden antenna with the resonant particle (RES). (c) Polarizability of the nano-antenna (black lines) and field enhancement at the point of the object, 30 nm from the apex (crimson lines). (d) Absorption cross section obtained from FDTD simulation of the antenna and the object, when placing the monitor just around the object (full pink line) compared to the field-enhanced object absorption of Eq. (4.1). We compare the lineshape to the negative of the baselined extinction cross section to demonstrate that the field-enhanced object absorption does not describe the lineshape.

approximation and point field enhancement. We can see that for this particular antenna, the field enhancement at the position of the object center at the resonance is about 40 times greater than the field of the incoming wave. The enhancement of the molecular signal for the case of this particular antenna is $\left|f\right|^2 \approx 1600$, as we can see from the field enhancement magnitude at resonance plotted in Fig. 4.1 (c).

Nevertheless, when comparing the signature obtained after subtracting BG simulation from RES simulation with field-enhanced molecular absorption, it does predict the magnitude of the molecular signal at the resonance, but not the lineshape, as we can see in Fig. 4.1 (d).

4.2 Detecting the antenna scattering in SEIRA

We now recapitulate part of the results from Ref. [11] and build on them.

4.2.1 Molecular signatures

First, we show molecular signatures obtained from FDTD simulations. We plot baselined molecular signatures (obtained after subtraction of the BG simulation) for the system of gold nano-antenna from Fig. 2.4 with two PDMS spheres in Fig. 4.2 (a).

We will now study the dependency of molecular signatures on antenna size. We numerically calculated magnitudes of extinction, scattering, and absorption molecular signatures for cylindrical gold antennas of varying diameter and length (which we previously described in Sec. 2.2.2). All antennas are resonantly tuned approximately to the frequency of the PDMS oscillator at 7.9 µm. We can see the results in Fig. 4.2 (b), for which we obtained the same results as in [47]. The extinction signature was obtained by summing the scattering and absorption signatures. Depending on the antenna coupling regime (blue, green, and red regions in Fig. 2.4) we can distinguish three different types of signatures. For under coupled regime (small antennas) both the absorption and scattering are negative. That is until the point of the critical coupling, where the total antenna scattering and absorption cross sections are equal. While looking at the molecular signature for the critically coupled regime, the whole contribution to extinction is given by scattering, as the absorption is approximately zero. For larger antennas (over-coupled regime) absorption signature flips sign and is positive from now on. This behavior results in a decrease of the extinction signature magnitude compared to scattering, which means that by looking at the scattering signature, we would obtain a larger signal. We will deal with the process behind the flip of the absorption signature sign later in this section. Now we move to describing the cross section signatures with an analytical model.

Firstly, we suppose that the antenna has much larger components of the polarizability tensor $\overleftrightarrow{\boldsymbol{\alpha}}^{\mathrm{A}}$ than the object $\overleftrightarrow{\boldsymbol{\alpha}}^{\mathrm{O}}$. This condition can be fulfilled for example for gold IR antennas [x-component of polarizability in Fig. 4.1) (c)], and for small sphere representing the molecules as we can see for example in Fig. 4.1) (a). The ratio between the magnitudes of the antenna polarizability and the polarizability of the small molecular sample is $\alpha^{\mathrm{A}}/\alpha^{\mathrm{O}} \approx 10^7$. With this in mind, we make an approximation in the scattered field of Eq. (2.9) and we neglect all terms multiplied with $\overleftrightarrow{\boldsymbol{\alpha}}^{\mathrm{O}} \cdot \overleftrightarrow{\boldsymbol{\alpha}}^{\mathrm{O}}$ and the terms with multiplications repeated more times. We can also neglect the field scattered directly by the object after being illuminated by the incoming field $\mathbf{E}^{\mathrm{O}}$. When we consider large field

enhancement $\overleftrightarrow{\boldsymbol{f}} \gg \overleftrightarrow{\boldsymbol{I}}$, the terms $\mathbf{E}^{\mathrm{AO}}$ and $\mathbf{E}^{\mathrm{OA}}$ are negligible compared to the $\mathbf{E}^{\mathrm{AOA}}$ and can be neglected, too [43]. The approximate expression for the scattered field then reads

$$\mathbf{E}^{\mathrm{tot}}_{\mathrm{sca}} \approx \underbrace{\frac{k^2}{\varepsilon_0}\overleftrightarrow{\mathbf{G}}^{\mathrm{A}}_{\mathrm{sca}} \cdot \overleftrightarrow{\boldsymbol{\alpha}}^{\mathrm{A}} \cdot \mathbf{E}^{\mathrm{A}}_{\mathrm{inc}}}_{\mathbf{E}^{\mathrm{A}}} + \underbrace{\frac{k^2}{\varepsilon_0}\overleftrightarrow{\mathbf{G}}^{\mathrm{A}}_{\mathrm{sca}} \cdot \overleftrightarrow{\boldsymbol{f}} \cdot \overleftrightarrow{\boldsymbol{\alpha}}^{\mathrm{O}} \cdot \overleftrightarrow{\boldsymbol{f}} \cdot \mathbf{E}^{\mathrm{A}}_{\mathrm{inc}}}_{\mathbf{E}^{\mathrm{AOA}}}. \tag{4.2}$$

Similarly, as in Section 2.2, where we derived the optical cross section for structures defined by their polarizability, we can derive the optical cross section for the antenna-object system. For obtaining the cross section SEIRA system, we have to plug the approximate expression for the scattered field of the antenna-object system of Eq. (4.2), into the optical theorem of Eqs. (2.10-2.12) for extinction and into Eq. (2.15) for scattering, as was done in Ref. [11]. From this derivation, the spectral signatures were interpreted in terms of interference, the $\mathbf{E}^{\mathrm{AOA}}$ carries the information about the molecule, and it is labeled as the field-enhanced molecular scattering. In case of extinction, where we look at the scattered light in the direction of the incoming field $\mathbf{E}^{\mathrm{A}}_{\mathrm{inc}}$, the field enhanced molecular scattering $\mathbf{E}^{\mathrm{AOA}}$ interferes with the incident field $\mathbf{E}^{\mathrm{A}}_{\mathrm{inc}}$. For the case of scattering $\mathbf{E}^{\mathrm{AOA}}$ interferes with the field scattered directly by the antenna $\mathbf{E}^{\mathrm{A}}$. The interference in both the extinction and scattering then yield the molecular features observed in the SEIRA spectra. For the derivation used in this thesis, we take a slightly different path, with which we obtain the same results. We use the fact, that $\mathbf{E}^{\mathrm{A}}$ and $\mathbf{E}^{\mathrm{AOA}}$ are propagated by the Green's dyadic of the antenna. We write the approximate of the total scattered field in the form $\mathbf{E}^{\mathrm{tot}}_{\mathrm{sca}} \approx \frac{k^2}{\varepsilon_0}\overleftrightarrow{\mathbf{G}}^{\mathrm{A}}_{\mathrm{sca}} \cdot \overleftrightarrow{\boldsymbol{\alpha}}^{\mathrm{system}} \cdot \mathbf{E}^{\mathrm{A}}_{\mathrm{inc}}$ where we introduced the polarizability of the Antenna-Object system as

$$\overleftrightarrow{\boldsymbol{\alpha}}^{\mathrm{system}} = \overleftrightarrow{\boldsymbol{\alpha}}^{\mathrm{A}} + \overleftrightarrow{\boldsymbol{f}} \cdot \overleftrightarrow{\boldsymbol{\alpha}}^{\mathrm{O}} \cdot \overleftrightarrow{\boldsymbol{f}}. \tag{4.3}$$

We again consider x-polarization of the incident field and prevailing xx-terms in both polarizability and field enhancement tensors. The scalar polarizability of the antenna-object system then reads

$$\alpha^{\mathrm{system}} = \alpha^{\mathrm{A}} + f^2\alpha^{\mathrm{O}}. \tag{4.4}$$

With the polarizability of the antenna-object system, we now express the optical cross sections. Firstly we plug the system polarizability into the extinction cross section in Eq. (2.13) and we get

$$\sigma_{\mathrm{ext}} \approx \frac{k}{\varepsilon_0}\mathrm{Im}\{\alpha^{\mathrm{A}} + f^2\alpha^{\mathrm{O}}\} = \sigma^{\mathrm{A}}_{\mathrm{ext}} + \Delta\sigma_{\mathrm{ext}}. \tag{4.5}$$

We divided the equation into two terms and in the first term, we recognized the bare antenna extinction cross section $\sigma^{\mathrm{A}}_{\mathrm{ext}}$ as in Eq. (2.18). The second term is the signature in the antenna extinction caused by the presence of the object $\Delta\sigma_{\mathrm{ext}}$ which reads

$$\Delta\sigma_{\mathrm{ext}} = \frac{k}{\varepsilon_0}\mathrm{Im}\{f^2\alpha_{\mathrm{O}}\}. \tag{4.6}$$

We can see that the molecular signature in extinction scales with the object polarizability α^{O} and with the square of the field enhancement f^2, which is in concordance with the

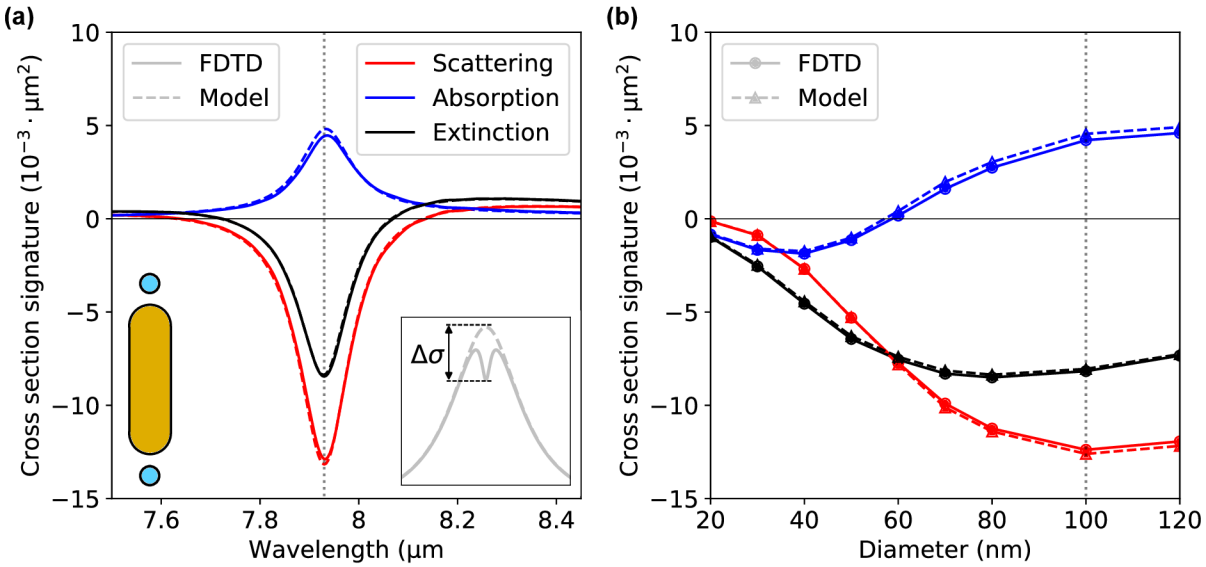

Figure 4.2: (a) Scattering, extinction, and absorption cross section signatures (subtracted molecular features in the SEIRA spectra, see inset) for a system consisting of a nano-antenna and two spherical objects representing molecular samples at its apexes (see inset scheme) The nano-antenna is a round-rod shaped with hemispherical apexes of 100 nm diameter and 3.19 µm length, previously discussed as a model case nano-antenna in Fig. 2.4. With full line we plot obtained from FDTD simulations. With the dashed line, we plot the cross sections obtained analytically from Eqs. (4.6),(4.8) and (4.11). For evaluating the analytical model we used antenna polarizability, object polarizability and field enhancement near the antenna apexes as described in Appendix C.1. With the vertical dotted line, we mark the molecular resonance wavelength (approximately at 7.9 µm), at which we will take the values of the magnitudes into (b). We can see that with the analytical expressions, we are able to fully describe the lineshapes of all three optical cross sections. (b) Cross section signatures magnitudes at resonance for different antennas from Fig. 2.3 (b). We can see that we can attribute the behavior of the different signatures to the antenna coupling regimes from Fig. 2.4 (b). For the critically coupled antenna (diameter 60 nm) the absorption signature vanishes and the extinction is uniquely given by the scattering contribution. With the vertical dotted line, we mark the values for 100 nm diameter antenna from (a). The cross sections obtained analytically from Eqs. (4.9),(4.10) and (4.15).

reports from literature [81, 93]. Thus for the largest extinction signature, when looking at the same molecular sample (α^{O} is the same in all cases), we want to find an antenna with the largest field enhancement at the position of the sample. Previously it was reported that the largest field enhancement would take place in the critical coupling regime for gap antenna (two nanorods coupled together), where the field is evaluated in gap [94]. Thus gap antennas, which already have great field enhancement in the gap, look like promising candidates We plot the computed extinction in Fig. 4.2 (a). We can see that compared to the antenna-enhanced molecular absorption of Eq. (4.1) we are now able to fully describe the extinction signature lineshape.

After deriving the extinction cross section of the SEIRA system, we can also look at the scattering cross section signature. As we mentioned previously, SEIRA was thought of as a unique absorption process, with a negligible enhanced molecular scattering, but in

Ref. By plugging the polarizability of the antenna-object system (4.4) into the scattering cross section (2.16) we obtain

$$\sigma_{\mathrm{sca}} \approx \frac{k^4}{6\pi\varepsilon_0^2}\left(\left|\alpha^{\mathrm{A}}\right|^2 + 2\mathrm{Re}\left\{f^2\left(\alpha^{\mathrm{A}}\right)^*\alpha^{\mathrm{O}}\right\} + \left|f^2\alpha^{\mathrm{O}}\right|^2\right) \approx \sigma_{\mathrm{sca}}^{\mathrm{A}} + \Delta\sigma_{\mathrm{sca}}. \tag{4.7}$$

We divide this expression into three terms, in the first we again recognize the scattering of the bare antenna $\sigma_{\mathrm{sca}}^{\mathrm{A}}$ from Eq. (2.19). Previously it was assumed that the third term, which is the object scattering influenced by the antenna near-field was is the only contribution to the scattering in SEIRA. With the model used here, the interference of the field scattered by the antenna and the $\mathbf{E}^{\mathrm{AOA}}$ is considered and introduces the second term in parentheses. From Fig. 4.1) (a) and (c) we can read values of α^{A}, α^{O} and f of a model-case nano-antenna considered. From the values, we see that the last term in the parentheses of Eq. (4.7) can be neglected, as it is approximately four orders of magnitude smaller than the second term. The second term

$$\Delta\sigma_{\mathrm{sca}} = \frac{k^4}{3\pi\varepsilon_0^2}\mathrm{Re}\left\{f^2\left(\alpha^{\mathrm{A}}\right)^*\alpha^{\mathrm{O}}\right\}, \tag{4.8}$$

is then responsible for the molecular signature in scattering cross section. We recognize that the scattering signature depends on the field enhancement, similarly to the extinction cross section of Eq. (4.6), and in addition, it also depends on the antenna polarizability. This results in the scattering signature being inherently connected to the size and the material of the nano-antenna and also in the need to design nano-antenna with large polarizability which also produces strong near-fields in its vicinity. We plot the scattering signature for our model case antenna in Fig. 4.2 (a) and we see that with this model we are again able to fully describe the lineshape and magnitude of molecular scattering signal.

We now express the cross-section signatures at molecular resonance frequency ω_{res}, and for the next, we denote $\sigma(\omega_{\mathrm{res}}) = \sigma^{\mathrm{r}}$. As we mentioned in the previous section and can see in Fig. 4.1) (c), both the field enhancement and antenna polarizability are purely imaginary at the energy of the molecular resonance ω_{res}, from which we can than deduce that $\arg(f)$ and $\arg(\alpha^{\mathrm{A}})$ are equal to $\pi/2$ at the ω_{res}. As the antenna polarizability is purely imaginary, we also note that at the resonance, we have $\mathrm{Im}\left\{\alpha^{\mathrm{A}}(\omega_{\mathrm{res}})\right\} = \left|\alpha^{\mathrm{A}}(\omega_{\mathrm{res}})\right|$. In the following, we will deal with the cross sections at the resonance frequency and we will then write the antenna polarizabilities at the resonance as $\left|\alpha^{\mathrm{A}}\right|$. For the expression at resonance, we assume that all the variables on the right-hand side are evaluated at the resonance too, and we don't write the index $(\cdot)^{\mathrm{r}}$ for simplicity.

We can now write the extinction signature of Eq. (4.6) at resonance frequency as

$$\Delta\sigma_{\mathrm{ext}}^{\mathrm{r}} = -\frac{k}{\varepsilon_0}\left|f\right|^2\mathrm{Im}\left\{\alpha^{\mathrm{O}}\right\}. \tag{4.9}$$

We recognize that at the resonance the extinction signature is equal to the negative of the enhanced object absorption of Eq. (4.1), which we already saw in Fig. 4.1 (d).

When we express scattering signature from Eq. (4.8), we obtain

$$\Delta\sigma_{\mathrm{sca}}^{\mathrm{r}} = -\frac{k^4}{3\pi\varepsilon_0^2}\left|f\right|^2\left|\alpha^{\mathrm{A}}\right|\mathrm{Im}\left\{\alpha^{\mathrm{O}}\right\}. \tag{4.10}$$

We plot the extinction and scattering signature values at molecular resonance in Fig. 4.2 (b) where we compare them with the numerically calculated ones. We see that despite the non-trivial course of the signatures, we can describe them with the model. We also note that the extinction signature is largest for the antenna of 80 nm diameter, for scattering for the antenna of 100 nm diameter, which is our considered model-case antenna.

To this point, the expressions in this section were recapitulated from Ref. [11], and we added the numerical and analytical results for different antenna sizes. Unlike in the reference, we also focus on the absorption and absorption signatures and express them from the energy conservation, where

$$\sigma_{\mathrm{abs}} = \sigma_{\mathrm{ext}} - \sigma_{\mathrm{sca}} = \sigma_{\mathrm{abs}}^{\mathrm{A}} + \Delta\sigma_{\mathrm{abs}}, \tag{4.11}$$

where we again divided the cross section into two contributions. In the first, we recognize the absorption cross section of the bare antenna $\sigma_{\mathrm{abs}}^{\mathrm{A}} = \sigma_{\mathrm{ext}}^{\mathrm{A}} - \sigma_{\mathrm{sca}}^{\mathrm{A}}$. The second term $\Delta\sigma_{\mathrm{abs}} = \Delta\sigma_{\mathrm{ext}} - \Delta\sigma_{\mathrm{sca}}$ is the molecular signature in the absorption cross section. We plot the absorption signature in Fig. 4.2 (b) and we again compare it with the numerical result, for which we can again describe the lineshape, with a slightly larger error, due to the error propagation.

Now we take a step back and again look at the total antenna cross sections of Eqs. (2.18-2.20), expressed at the energy of the molecular resonance. We again replace the imaginary part of antenna polarizability $\mathrm{Im}\{\alpha^{\mathrm{A}}\}$ with their magnitude at resonance $\left|\alpha^{\mathrm{A}}\right|$. The antenna extinction at the resonance then reads

$$\sigma_{\mathrm{ext}}^{\mathrm{A,r}} = \frac{k}{\varepsilon_0}\left|\alpha^{\mathrm{A}}\right|. \tag{4.12}$$

The scattering cross section is

$$\sigma_{\mathrm{sca}}^{\mathrm{A,r}} = \frac{k^4}{6\pi\varepsilon_0^2}\left|\alpha^{\mathrm{A}}\right|^2. \tag{4.13}$$

We can also express the antenna absorption from the energy conservation and get

$$\sigma_{\mathrm{abs}}^{\mathrm{A,r}} = \sigma_{\mathrm{ext}}^{\mathrm{A,r}} - \sigma_{\mathrm{sca}}^{\mathrm{A,r}}. \tag{4.14}$$

For small antennas, which are dominantly absorbing and their scattering cross section is negligible due to the scaling with the square of the polarizability, the extinction is For large antennas where scattering dominates the extinction, we have $\sigma_{\mathrm{ext}}^{\mathrm{A,r}} \approx \sigma_{\mathrm{sca}}^{\mathrm{A,r}}$. The total cross sections at the energy of the PDMS resonance at approximately 7.9 µm were previously plotted in Fig. where we saw, that the model matches the results obtained from numerical simulations fairly well.

We now express the absorption signature at the molecular resonance from the energy conservation, using Eqs. (4.9) and (4.10)

$$\Delta\sigma_{\mathrm{abs}}^{\mathrm{r}} = \Delta\sigma_{\mathrm{ext}}^{\mathrm{r}} - \Delta\sigma_{\mathrm{sca}}^{\mathrm{r}} = \underbrace{-\frac{k}{\varepsilon_0}\left|f\right|^2\mathrm{Im}\{\alpha^{\mathrm{O}}\}}_{\Delta\sigma_{\mathrm{ext}}^{\mathrm{r}}}\left[1 - \frac{\left|\alpha^{\mathrm{A}}\right|}{\left|\alpha^{\mathrm{A,crit}}\right|}\right]. \tag{4.15}$$

Here, we recognized that we can express scattering from Eq. (4.10) via the extinction signature of Eq. (4.9) which we factor out. We then obtain antenna polarizability magnitude

$\left|\alpha^{\mathrm{A}}\right|$ multiplied by a factor $k^3/(3\pi\varepsilon_0)$. When considering the case of the critically coupled antenna ($\sigma_{\mathrm{abs}} \approx \sigma_{\mathrm{sca}}$), the absorption signature is zero. As the extinction signature is always non-zero at the resonance [Eq. (4.9)], it means that the terms in parentheses must be zero, therefore the antenna polarizability must be equal to the inverse of the prefactor. We label the inverse of the prefactor as the polarizability of the critically coupled antenna which reads

$$\left|\alpha^{\mathrm{A,crit}}\right| = \frac{3\pi\varepsilon_0}{\left(k^{\mathrm{r}}\right)^3}. \tag{4.16}$$

We used this concept as we can see that for critically coupled antennas with polarizability $\left|\alpha^{\mathrm{A}}\right| = \left|\alpha^{\mathrm{A,crit}}\right|$, the absorption signature is zero.

Now we have expressions for all three spectral signatures at the resonance $\Delta\sigma^{\mathrm{r}}_{\mathrm{ext}}, \Delta\sigma^{\mathrm{r}}_{\mathrm{sca}}$ and $\Delta\sigma^{\mathrm{r}}_{\mathrm{abs}}$ and we plot them in Fig. 4.2 (b)[1] with triangles connected by a dashed line. We again used the field enhancement and antenna polarizability obtained from FDTD and analytically calculated object polarizability from Eq. (C.1) as in the previous section. We see very good match with the numerical results, the relative error in scattering is <2.5%, in extinction <5%. In Absorption the relative error is 40% for the critically coupled antenna of diameter 60, as the values are near zero, the error diminishes to about 5% for the smallest and largest antennas and the flip in the absorption signature. We also recognize that the extinction signature is largest for the antenna with diameter 80 nm. From the model, we can then assume that the field enhancement produced by this particular antenna is therefore largest at point 30 nm from the antenna apex. As we are changing the size of the nano-antennas (radii and lengths as in Fig.), many factors, such as the local curvature or charge reservoir can contribute to the spatial decay of the field enhancement. We discuss this behavior for different antennas in Sec. more thoroughly.

Now we focus on the explanation of the flip in absorption signature sign. The total absorption signature consists of the enhanced object absorption $\sigma^{\mathrm{O,enh}}_{\mathrm{abs}}$ and of the change in the absorption cross section caused by the presence of the field of the object $\Delta\sigma^{\mathrm{r}}_{\mathrm{abs}}$. These changes arise due to multiple illumination of the antenna by the near-field of the object. We can evaluate the change in antenna absorption from FDTD simulations, we can put the absorption monitor just around the antenna. Fig. 4.3 (a) In Fig. 4.3 (b) we plot the total absorption signature and the contributions of field-enhanced molecular absorption and change in the antenna absorption for different sizes of antennas of Fig.. We see that there is an interplay between the positive field enhanced and negative antenna absorption which results in the flip.

[1] While obtaining SEIRA baselined spectra of molecular signatures, we subtract BG simulation, with an object characterized by the background permittivity $\varepsilon^{\mathrm{O}}_{\mathrm{r}} = \varepsilon^{\mathrm{O}}_{\infty}$. The response of the object can be described by the quasistatic polarizability from Eq. (C.1) $\alpha^{\mathrm{O}}_{\mathrm{bkg}} = 4\pi\varepsilon_0 a^3(\varepsilon^{\mathrm{O}}_{\infty} - 1)/(\varepsilon^{\mathrm{O}}_{\infty} + 2)$, where we assumed that surrounding medium is vacuum with $\varepsilon_{\mathrm{r,m}} = 1$. In the analytical model, we then plug the polarizability α^{O} from which subtract the background polarizability $\alpha^{\mathrm{O}}_{\infty}$. The argument of the object polarizability after the subtraction of the background would then be $\pi/2$ as we see that it would be purely imaginary in Fig. 4.1 (a).

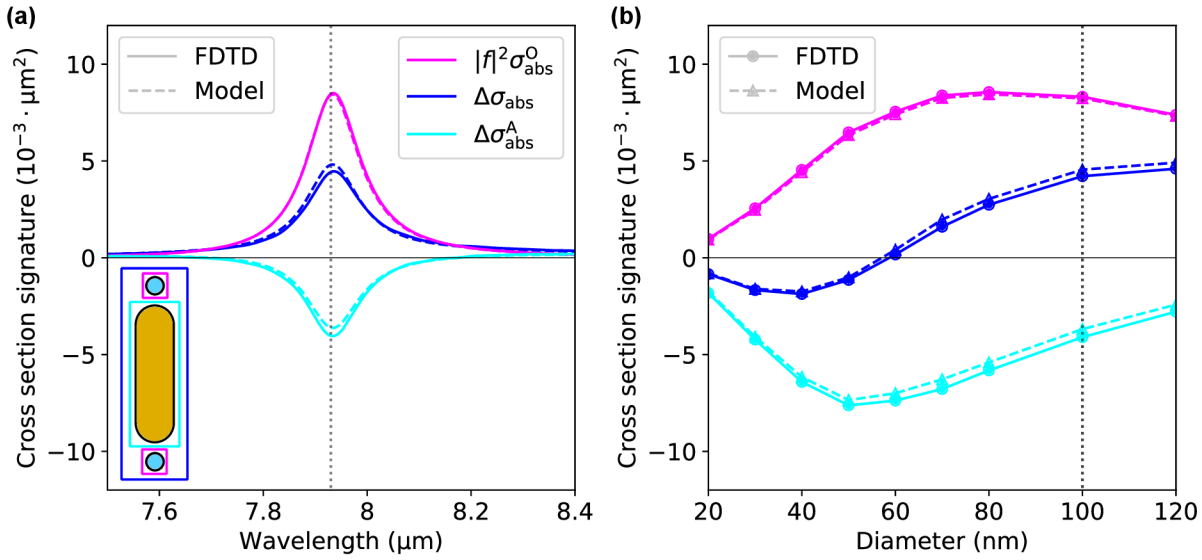

Figure 4.3: a) Absorption cross sections, were obtained from different monitors, as shown in the inset. The pink line corresponds to the field-enhanced molecular absorption obtained from FDTD (full line), previously plotted in Fig. 4.1 (d) and again compared with analytical results of Eq. (4.1) (dashed line). With the blue line, we plot the total absorption signature, as in Fig. 4.2 (a). With the cyan line, we plot the change in the antenna absorption caused by the presence of the object (the difference between the total absorption signature and the field-enhanced molecular absorption). We mark the resonance wavelength of the molecule with the dashed line. (b) Magnitudes of absorption signatures and field-enhanced molecular absorption for different antennas. We can see that depending on the value of the field enhanced molecular and the change in the antenna absorption we get different regimes of the total absorption, resulting in the flip of the sign. As is the enhanced object absorption at resonance equal to the negative extinction signature, it is the largest for the antenna of 80 nm diameter which has the largest field enhancement at the position of the center of the object

Now we evaluate the antenna absorption signature from the analytical model, where we plug for enhanced object absorption at the resonance and use the fact that the imaginary part is the magnitude

$$\Delta\sigma^{\mathrm{A,r}}_{\mathrm{abs}} = \Delta\sigma^{\mathrm{r}}_{\mathrm{abs}} - \sigma^{\mathrm{O,enh,r}}_{\mathrm{abs}} = \underbrace{-\frac{k}{\varepsilon_0}\left|f\right|^2 \mathrm{Im}\left\{\alpha^{\mathrm{O}}\right\}}_{\Delta\sigma^{\mathrm{r}}_{\mathrm{ext}}}\left[2 - \frac{\left|\alpha^{\mathrm{A}}\right|}{\left|\alpha^{\mathrm{A,crit}}\right|}\right]. \tag{4.17}$$

In Fig. 4.3 The field-enhanced molecular absorption in Eq. (4.1) is always positive.

We can see that for critically coupled antennas with polarizability $\left|\alpha^{\mathrm{A}}\right| = \left|\alpha^{\mathrm{A,crit}}\right|$, the antenna absorption signature is equal to the extinction signature, which is the negative of the field-enhanced object absorption. This results after summing the absorption contributions in the vanishing absorption signature for the critically coupled antenna. The validity of this formula needs to be verified, but we again discuss it next chapter.

For large antennas, similarly to the antenna absorption cross section, we can see that the $\Delta\sigma^{\mathrm{A,r}}_{\mathrm{abs}}$ is diminishing. The absorption signature could then be approximated just by the field-enhanced object absorption. From the energy conservation, we see that for this limiting case $\Delta\sigma^{\mathrm{r,lim}}_{\mathrm{ext}} = \Delta\sigma^{\mathrm{r,lim}}_{\mathrm{sca}} + \sigma^{\mathrm{O,enh}}_{\mathrm{abs}}$, and use the fact that the extinction signature

at resonance is negative of the enhanced object absorption $\sigma_{\mathrm{abs}}^{\mathrm{O,enh}}$. We can see that the scattering signature can then be as large as double the extinction signature, as was already reported in Ref. [11]

$$\Delta\sigma_{\mathrm{sca}}^{\mathrm{r,lim}} \approx 2\Delta\sigma_{\mathrm{ext}}^{\mathrm{r,lim}}. \tag{4.18}$$

Therefore, when considering large antennas and performing a scattering experiment, the vibrational signal would be twice as large as one seen in extinction.

4.2.2 Molecular contrasts

Various metrics can be chosen to describe the magnitude of the enhanced SEIRA signal. For example, contrast normalized to the volume of the molecular layer was proposed in Ref. [47]. We choose a different metric and define the relative molecular contrast $\delta\sigma$ as the ratio between molecular signature in the cross section $\Delta\sigma$ and the total antenna cross section σ^{A}. We plot the molecular contrasts for our model case system (cylindrical gold nano-antenna with hemispherical apexes and two nanospheres with the center located 30 nm from each apex) obtained from FDTD calculations with the full lines in Fig. 4.4 (a). Similarly to the signatures, we obtain peak or dip features around the molecular resonance. We can see that for this particular antenna, the absorption contrast is larger than the extinction and scattering in this case, as the antenna cross section in the denominator is diminishing. In Fig. 4.4 (b), we plot the molecular contrasts for various antenna sizes from Fig. 2.3 (b) with dots connected by full lines. For evaluation, we used antenna cross sections from Fig. 2.4 (b) and molecular signatures from Fig. 4.2 (b). We can see that, similarly to the absorption signature, the absorption contrast flips sign and is zero for the critically coupled antenna. For large antennas, where the antenna absorption cross section in the denominator diminishes, the contrast greatly grows. We also note that the largest extinction and scattering contrasts are maximal for the antenna of 50 nm diameter. Furthermore, the scattering contrast appears to be approximately twice as large as the extinction contrast.

We will now express the molecular contrasts analytically, for comparison of the analytical SEIRA model with numerical simulations and for obtaining information about the dependence of the contrasts on antenna parameters (polarizability and the field enhancement at a certain location). We write the molecular contrasts for extinction, scattering, and absorption, by using antenna cross sections from Eqs. (2.18-2.20) and molecular signatures from Eqs. (4.6), (4.8) and (4.11) as

$$\delta\sigma_{\mathrm{ext}} = \frac{\Delta\sigma_{\mathrm{ext}}}{\sigma_{\mathrm{ext}}^{\mathrm{A}}} = -\frac{\mathrm{Im}\{f^2\alpha^{\mathrm{O}}\}}{\mathrm{Im}\{\alpha^{\mathrm{A}}\}}, \tag{4.19}$$

$$\delta\sigma_{\mathrm{sca}} = \frac{\Delta\sigma_{\mathrm{sca}}}{\sigma_{\mathrm{sca}}^{\mathrm{A}}} = -2\frac{\mathrm{Re}\{f^2(\alpha^{\mathrm{A}})^*\alpha^{\mathrm{O}}\}}{|\alpha^{\mathrm{A}}|^2}, \tag{4.20}$$

$$\delta\sigma_{\mathrm{abs}} = \frac{\Delta\sigma_{\mathrm{abs}}}{\sigma_{\mathrm{abs}}^{\mathrm{A}}} = \frac{\Delta\sigma_{\mathrm{ext}} - \Delta\sigma_{\mathrm{sca}}}{\sigma_{\mathrm{ext}}^{\mathrm{A}} - \sigma_{\mathrm{sca}}^{\mathrm{A}}}. \tag{4.21}$$

We plug in the antenna polarizability, field enhancement caused by the antenna at the position where the object center would be, and the object polarizability, as in the previous section. We plot the analytically obtained contrasts in Fig 4.4 (a) with the dashed line. We

can see that for extinction and scattering, we obtain good agreement between the model and numerical results, but for absorption, there is a discrepancy. It is caused by the error propagation in the antenna absorption cross section and the absorption signature, which are both obtained from extinction and scattering.

We again evaluate the cross section contrasts at the frequency of the molecular resonance frequency ω_{res} similarly as total antenna cross sections and molecular signatures in the previous section. Extinction contrast at resonance is

$$\delta\sigma_{\mathrm{ext}}^{\mathrm{r}} = \frac{\Delta\sigma_{\mathrm{ext}}^{\mathrm{r}}}{\sigma_{\mathrm{ext}}^{\mathrm{A,r}}} = -\frac{\left|f\right|^2}{\left|\alpha_{\mathrm{A}}\right|}\mathrm{Im}\{\alpha^{\mathrm{O}}\}. \tag{4.22}$$

We can see that the extinction contrast scales with the field enhancement squared, but compared to the extinction signature is also divided by the magnitude of the antenna polarizability. For the largest extinction contrast, the optimal antenna would be one with strong near-field enhancement in its vicinity and with small polarizability, e. g. a weakly polarizable and/or small antenna. We plot the calculated extinction contrasts at resonance in Fig. 4.4 (b). We can see, that the model predicts the contrasts obtained from FDTD fairly well, the relative error is for all antennas below 2%, except the smallest one (relative error about 7%). We see that the largest contrast emerges for an antenna of diameter 50 nm. From the model, we assume that for this particular antenna, the ratio between field enhancement at a distance 30 nm from the apex and the antenna polarizability would be maximal.

Scattering contrast at resonance is

$$\delta\sigma_{\mathrm{sca}}^{\mathrm{r}} = \frac{\Delta\sigma_{\mathrm{sca}}^{\mathrm{r}}}{\sigma_{\mathrm{sca}}^{\mathrm{A}}} = \underbrace{-2\frac{\left|f\right|^2}{\left|\alpha_{\mathrm{A}}\right|}\mathrm{Im}\{\alpha^{\mathrm{O}}\}}_{2\delta\sigma_{\mathrm{ext}}^{\mathrm{r}}}, \tag{4.23}$$

which is twice as large as the extinction contrast. This could be of great importance for scattering experiments. We again compare the results of the analytical model with the FDTD results in Fig. 4.4 (b). Similarly to the extinction, the relative errors between the model and FDTD are about 2% for all antennas except the smallest one, with a relative error of about 10%.

Absorption contrast at molecular resonance can then be written from the energy conservation as

$$\delta\sigma_{\mathrm{abs}}^{\mathrm{r}} = \frac{\Delta\sigma_{\mathrm{abs}}^{\mathrm{r}}}{\sigma_{\mathrm{abs}}^{\mathrm{A,r}}} = \frac{\Delta\sigma_{\mathrm{ext}}^{\mathrm{r}} - \Delta\sigma_{\mathrm{sca}}^{\mathrm{r}}}{\sigma_{\mathrm{ext}}^{\mathrm{A,r}} - \sigma_{\mathrm{sca}}^{\mathrm{A,r}}}. \tag{4.24}$$

Similarly to the absorption signature, the contrast flips sign and is zero for the case of the critically coupled antenna (diameter 60 nm). For larger antennas, as the antenna absorption in the denominator approaches zero, the absorption contrast grows. We again compare the analytical results with FDTD results in Fig. 4.4 (b). The relative errors for absorption contrast are larger than for the extinction and scattering contrasts, similarly to the absorption signature. It can be seen as a result of the error propagation and the fact, that for the antennas near the critical coupling, the scattering signature is near zero, which enhances the error between the model and FDTD.

We now focus on the contrasts of the antenna signatures, which we obtain after subtracting the molecular contribution to the respective signature. With these contrasts,

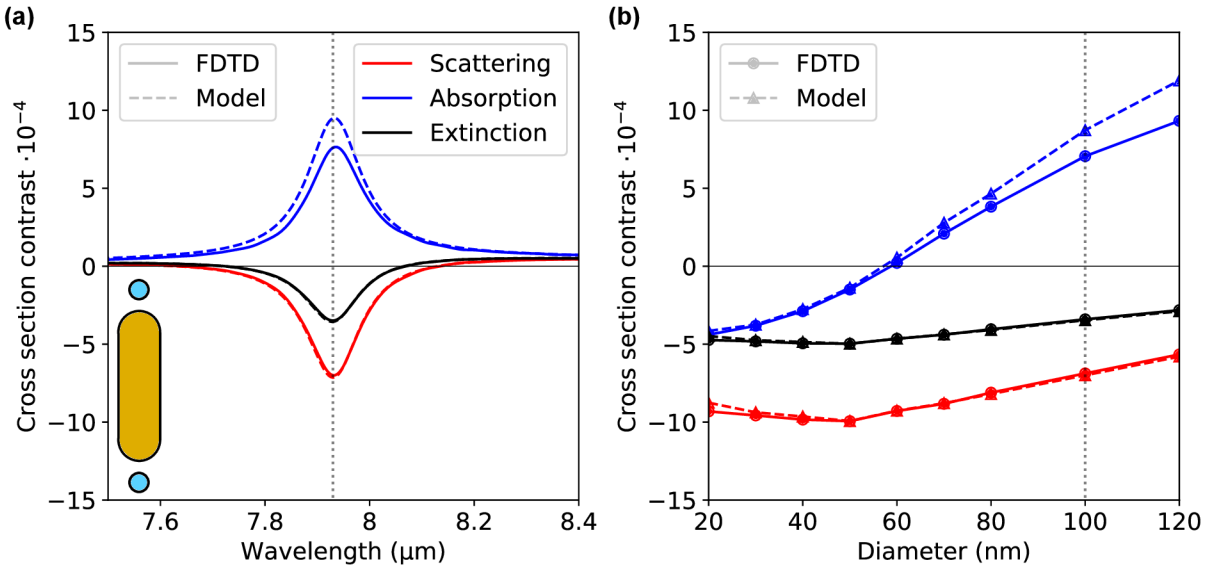

Figure 4.4: (a) Extinction, scattering and absorption cross-section contrasts, which are taken as molecular signatures divided by the total antenna cross sections for model-case system (50 nm diameter round-rod antenna with two objects placed near its apexes) from Figs. 4.2 and 2.4, respectively. With full lines, we plot contrasts obtained from FDTD simulations, with dashed lines contrasts obtained from the analytical model. (b) Cross section contrasts magnitudes for different sizes of nano-antennas. With dots connected by full lines, we plot the results from FDTD, and with triangles connected by dashed lines the analytical results. We recognize that scattering contrast is approximately twice as large as extinction contrast, which is the result of the analytical model. In absorption contrast, we see the characteristic flip of the sign and notice that it gets larger for larger antennas, as the antenna absorption cross section in the denominator diminishes. With the vertical dotted line, we mark the cross sections at resonance for the antenna in (a).

we gain insight into the changes in the antenna cross sections separated from the contribution of the enhanced molecular absorption. We already obtained a change in the antenna absorption in Eq. (4.17), with which we discussed its magnitude compared to the field-enhanced molecular absorption of Eq. (4.1). The relative magnitudes of these two contributions result in the flip of the sign of the summed absorption signature. The antenna absorption contrast is

$$\delta\sigma_{\mathrm{abs}}^{\mathrm{A,r}} = \frac{\Delta\sigma_{\mathrm{abs}}^{\mathrm{A,r}}}{\sigma_{\mathrm{abs}}^{\mathrm{A,r}}} = -2\frac{|f|^2}{|\alpha_{\mathrm{A}}|}|\alpha_{\mathrm{O}}|. \tag{4.25}$$

We used the assumption that the scattering cross section of the object is vanishingly small (the third term in Eq. (4.7) which was neglected) and the scattering signature is fully given by the change in the antenna scattering caused by the presence of the molecule

$$\Delta\sigma_{\mathrm{sca}}^{\mathrm{A,r}} \approx \Delta\sigma_{\mathrm{sca}}^{\mathrm{r}}. \tag{4.26}$$

In SEIRA spectra, one would expect that the enhanced molecular absorption would be in the form of a peak seen in the extinction spectra, as the power is lost in the excitation, but instead, we obtain a dip of the same magnitude in extinction. This means that there

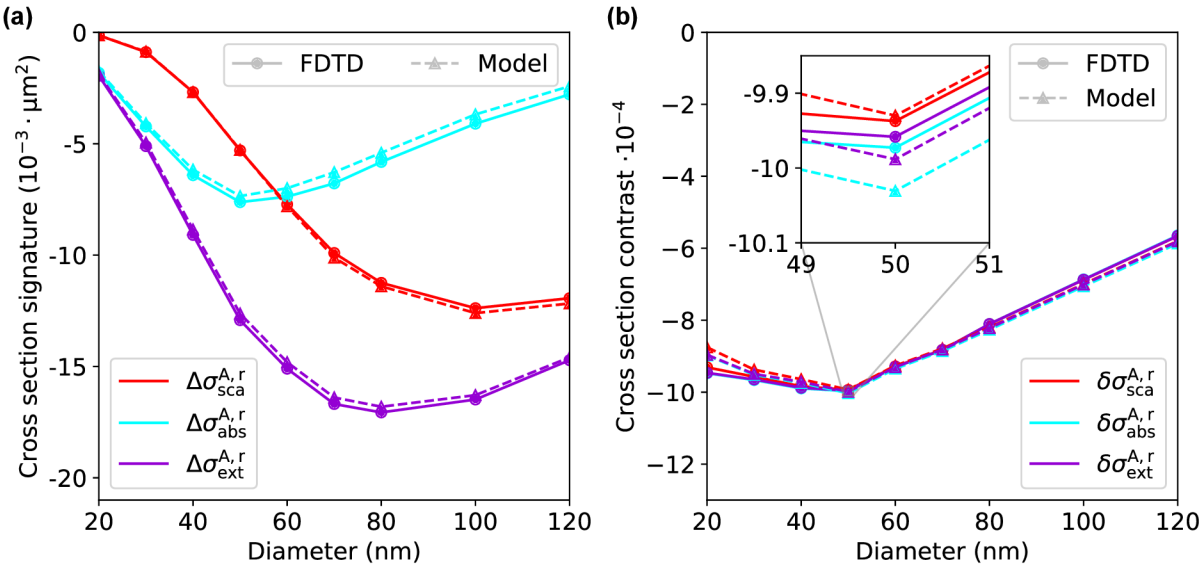

Figure 4.5: (a) Antenna signatures. With the red curve, we plot the change in the scattering cross section, which is fully given by the molecular signature in the scattering, thus the same as in Fig. 4.2 (b). With the cyan line, we plot the change in antenna absorption, which is the same as in Fig. 4.3 (b). With the purple curve, we plot the total change in the antenna extinction caused by the interaction with the object, which is negative of the enhanced object absorption multiplied by the factor of two. We can compare the evolution of the antenna signatures for different antennas with the total antenna cross sections of Fig. 2.4 (b). (b) Antenna cross section contrasts, obtained by dividing respective signatures from (a) with the total antenna cross sections from Fig. 2.4 (b). We can see that the antenna contrasts are the same for all three cross sections.

is a discrepancy of a factor of two and it needs to be compensated by the change in the antenna extinction (scattering and absorption)

$$\delta\sigma^{\mathrm{A,r}}_{\mathrm{ext}} = \frac{\Delta\sigma^{\mathrm{r}}_{\mathrm{ext}} - \Delta\sigma^{\mathrm{O,enh,r}}_{\mathrm{abs}}}{\sigma^{\mathrm{A,r}}_{\mathrm{ext}}} = -2\frac{|f|^2}{|\alpha_{\mathrm{A}}|}|\alpha_{\mathrm{O}}|. \tag{4.27}$$

We plot the changes in antenna cross sections for different antennas in Fig 4.5 (a). We can see that they resemble the total antenna cross sections in some features. The absorption has an extreme near the critical coupling regime and is the same as the scattering. For larger antennas, the absorption diminishes and the major contribution to the extinction is from the scattering. Because of the dependence of signatures on the field enhancement, the extinction and scattering are not increasing, but instead, they have an extreme and, for larger antennas, they diminish too.

When comparing Eqs. (4.25), (4.26) and (4.27), we recognize that all of the antenna contrasts are the same

$$\delta\sigma^{\mathrm{A,r}}_{\mathrm{sca}} = \delta\sigma^{\mathrm{A,r}}_{\mathrm{ext}} = \delta\sigma^{\mathrm{A,r}}_{\mathrm{abs}} = -2\frac{|f|^2}{|\alpha_{\mathrm{A}}|}|\alpha_{\mathrm{O}}|. \tag{4.28}$$

We plot the contrasts in Fig. 4.5 (b). The scattering contrast is from Fig. 4.4 (b). We recognize that both the analytical model and numerical calculations predict that the

contrasts are in fact the same. For this particular choice of antenna shapes and distance from the antenna apexes, where we place the object center, we obtain the largest contrast for an antenna with diameter 50 nm.

4.3 Field-enhanced electron energy-loss spectroscopy

As we stated and reviewed in Sec. 3.3, even the vibrational electron energy loss spectroscopy suffers from a loss of signal when probing small amounts of samples. As was proposed in Ref. [55], and further discussed in Ref. [92] an analog to surface-enhanced infrared absorption could be performed in EELS. By plugging the dipole moments of the antenna-object system [Eq. (2.4)] into Eq. (2.32) we reach the same expressions as in Ref. [55], with which we can model the field-enhanced electron energy loss spectroscopy (FEELS) lineshapes based on the coupled dipole model. We now derive the approximative model, considering a weakly polarizable object, and the EEL signatures and contrasts.

Firstly we assume that the feature in the spectrum caused by the object would only be a weak perturbation added to the loss probability of inducing a resonance within a nanoantenna. The total loss probability that the electron will interact with the antenna-object system can then be written as

$$\Gamma_{\mathrm{EELS}}(\omega) = \Gamma^{\mathrm{A}}_{\mathrm{EELS}}(\omega) + \Delta\Gamma_{\mathrm{EELS}}(\omega), \tag{4.29}$$

where is $\Gamma^{\mathrm{A}}_{\mathrm{EELS}}$ is the loss probability of the bare antenna from Eq. (2.38) and $\Delta\Gamma$ is the object signature in the spectrum. We again assume that the antenna is polarized dominantly in the x-direction. By assuming that we can expand the electric field inducing the dipole moment via the series from Eq. (2.5), we divide the signature in the EEL spectrum into individual terms

$$\begin{aligned}\Delta\Gamma_{\mathrm{EELS}}(\omega) = &\underbrace{\frac{1}{\pi\hbar}\mathrm{Im}\left\{E_x^{\mathrm{el,O},*}\alpha^{\mathrm{O}}E_x^{\mathrm{el,O}}\right\}}_{\Gamma^{\mathrm{O}}_{\mathrm{EELS}}} + \underbrace{\frac{1}{\pi\hbar}\mathrm{Im}\left\{E_x^{\mathrm{el,O},*}\alpha^{\mathrm{O}}fE_x^{\mathrm{el,A}}\right\}}_{\Gamma^{\mathrm{OA}}_{\mathrm{EELS}}} \\ &+ \underbrace{\frac{1}{\pi\hbar}\mathrm{Im}\left\{E_x^{\mathrm{el,A},*}f\alpha^{\mathrm{O}}E_x^{\mathrm{el,O}}\right\}}_{\Gamma^{\mathrm{AO}}_{\mathrm{EELS}}} + \underbrace{\frac{1}{\pi\hbar}\mathrm{Im}\left\{E_x^{\mathrm{el,A},*}f^2\alpha^{\mathrm{O}}E_x^{\mathrm{el,A}}\right\}}_{\Gamma^{\mathrm{AOA}}_{\mathrm{EELS}}} + \dots .\end{aligned} \tag{4.30}$$

The first term $\Gamma^{\mathrm{O}}_{\mathrm{EELS}}$ is the loss probability of the sole object. $\Gamma^{\mathrm{OA}}_{\mathrm{EELS}}$ is the first term which accounts for a multiple scattering between the antenna and the object. The object is induced with the near-field produced by the antenna induced by the electron beam, then the object then acts back on the electron beam causing the energy loss. $\Gamma^{\mathrm{AO}}_{\mathrm{EELS}}$ denotes the loss caused after the beam interacts with the antenna induced by the near-field of the object. The last written term $\Gamma^{\mathrm{AOA}}_{\mathrm{EELS}}$ accounts for the double scattering event between the antenna and the object. The electron beam induces the dipole in the antenna, which then, via its near-field, induces the object, which acts back on the antenna. The antenna then interacts with the beam, which loses energy. The following terms can be derived in a similar manner, but we will not deal with them as we are again considering weakly scattering objects, which results in these terms being negligible.

For the numerical calculations and evaluation of the FEELS, we consider a round-rod-shaped hBN antenna, which supports localized phonon polaritons, previously considered

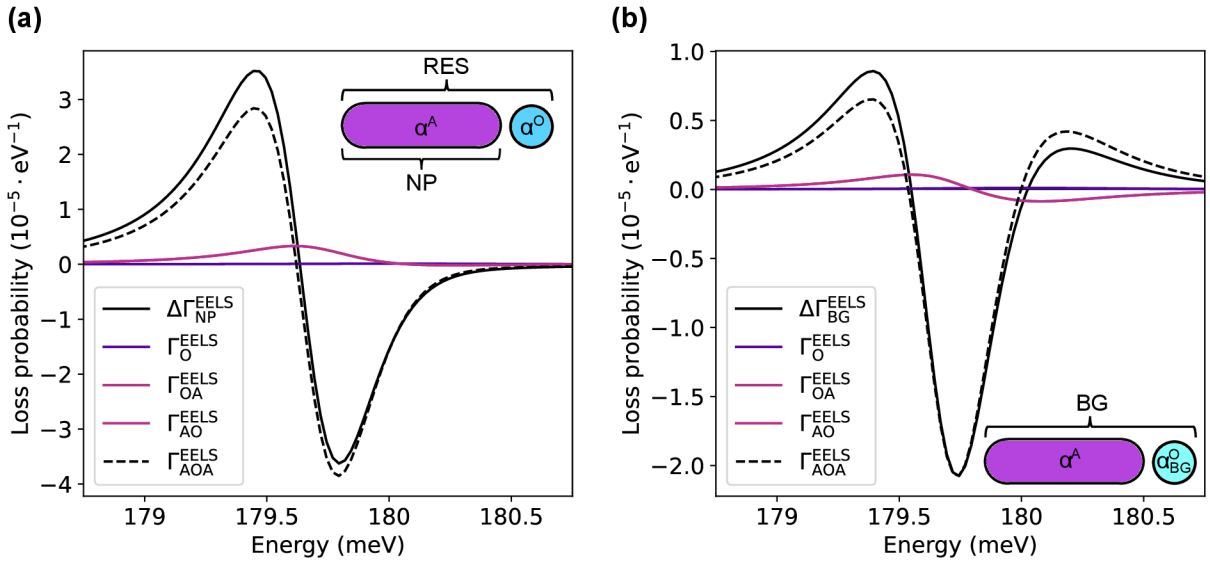

Figure 4.6: (a) Electron-energy loss spectrum molecular signature of a CBP sphere (10 nm radius) with center placed 30 nm from the apex of a cylindrical-shaped hBN antenna with round apexes (radius 20 nm and length 120 nm) obtained after subtraction of the spectrum of the bare antenna with no particle (NP) from the spectrum of the antenna and resonant object (RES). We also plot individual terms of Eq. (4.30): Γ^{O}_{EELS} (purple line), Γ^{OA}_{EELS} and Γ^{AO}_{EELS} are the same (pink lines), and Γ^{AOA}_{EELS} (black line). (b) EEL molecular signature obtained by subtracting the simulation with an object characterized by the background polarizability α^{O}_{∞} of the same sphere from Eq. (C.1), characterized just by $\varepsilon_{\infty} = 2.8$, which we label as the "BG" simulation, compared to the "RES" simulation in (a). We again plot the individual terms from Eq. (4.30) into which we plug the polarizability $\alpha^{O} - \alpha^{O}_{\infty}$ with the same color legend as in (a). CBP was modeled via the Lorentz oscillator model of Eq. (1.44). We assumed one oscillator with parameters $\varepsilon_{\infty} = 2.8$, $F_1 = 382.683\,\text{meV}^2$, $\omega_{0,1} = 179.777\,\text{meV}$ and $\gamma_1 = 1.029\,\text{meV}$.

in Secs. 2.2.2 and 2.3.3. We perform all numerical computations in COMSOL [described in Appendix C.2.2], where we consider just one object at the antenna apex for simplicity, as we do not exploit the simulation symmetries. Our considered object is again a nanosphere of radius 10 nm characterized by one oscillator of the CBP dielectric function [Fig. 1.2 (b)] positioned 30 nm from the antenna apex.

We again perform more simulations to obtain FEEL spectra. The first simulation is with both the antenna and object characterized by their respective dielectric functions interacting with the field of the electron beam, we label this simulation as "resonant" (RES). The second simulation labeled as "no particle" (NP) considers just the bare antenna. When we subtract NP simulation from RES, we obtain a molecular signature in the EEL spectra. Similarly to the optical-cross sections (Fig. 4.1), because of the redshift of the spectra caused by the background permittivity of the object, we obtain an asymmetric Fano-like shape. We plot the loss probability signature in Fig. 4.6 (a) with the full black line.

We plot the individual terms of Eq. (4.30) in Fig. 4.6. We approximate the object polarizability by the quasistatic polarizability of Eq. (C.1). The loss probability of inducing a resonance within the object Γ^{O}_{EELS} is negligible (about $10^{-7}\,\text{eV}^{-1}$). The Γ^{AO}_{EELS} and Γ^{OA}_{EELS} terms are the same with magnitude in the order of $10^{-6}\,\text{eV}^{-1}$. The Γ^{AOA}_{EELS} term almost

describes the lineshape near the resonance, albeit it is a bit distorted further away from the resonance.

Similarly to Sec. 4.1, we subtract a simulation with an object defined by the background permittivity $\varepsilon_\infty = 2.8$, which we again label as "background" (BG) simulation, from the RES simulation, to counteract the redshift caused by the dielectric background. We obtain a different lineshape, which is not as asymmetric as the one obtained by subtracting NP simulation, and we can now recognize the characteristic dip in the spectra (compare with Fig. 4.1). We again plot the individual terms of Eq. (C.1) into which we plugged the polarizability of the object from which we subtracted the background polarizability $\alpha_\infty^{\mathrm{O}}$ given by Eq. (C.1) into which we plugged $\varepsilon_\infty = 2.8$. We can see that the $\Gamma_{\mathrm{EELS}}^{\mathrm{O}}$ term is again negligible, and the $\Gamma_{\mathrm{EELS}}^{\mathrm{AO}}$ and $\Gamma_{\mathrm{EELS}}^{\mathrm{OA}}$ terms contribute mainly off resonance. The $\Gamma_{\mathrm{EELS}}^{\mathrm{AOA}}$ term predicts the lineshape fairly well, particularly near the resonance energy. Therefore we approximate the signature in the EEL only by the contribution by the double scattering event between an antenna and the molecule $\Gamma_{\mathrm{EELS}}^{\mathrm{AOA}}$ as

$$\Delta\Gamma_{\mathrm{EELS}}(\omega) \approx \frac{1}{\pi\hbar}\mathrm{Im}\Big\{E_x^{\mathrm{el,A},*} f^2 \alpha^{\mathrm{O}} E_x^{\mathrm{el,A}}\Big\}. \tag{4.31}$$

The larger the antenna polarizability compared to the object polarizability, the more precise this approximation is. In such case, we obtain larger field enhancement, resulting in all terms except $\Gamma_{\mathrm{EELS}}^{\mathrm{AOA}}$ negligible. From now on, we will always assume that the signatures are obtained by subtracting the BG simulation.

One of the motivations of this study was to compare the obtained signal in enhanced spectroscopy with photons (e.g. extinction cross section) and with electrons (electron energy-loss spectroscopy). Hence, we now compare the EEL probability signature with the extinction signature. The comparison of EEL spectra and extinction spectra of enhanced spectroscopies was already done in Ref. [95], where symmetries and detuning were discussed.

We plot the EEL signature in Fig. 4.7 with the blue line and the extinction signature with the red line and we can recognize that the lineshapes are very similar. We can compare the approximative analytical formulas Eq. (4.31) and Eq. (4.6) where we assume that the molecular signature in the spectra is based on the double scattering event between the antenna and the object and depend on $\mathrm{Im}\{f^2\alpha^{\mathrm{O}}\}$. We plot the analytical models in Fig. 4.7 (a) with dashed lines and recognize that we are able to describe both the extinction (similarly to Sec. 4.2) and EELS signatures close to the resonance energy (dotted line), but further away there appear small deviations, which could be attributed to the neglection of the other terms in the analytical mode.

We can again focus on the loss probability signature at the frequency of the molecular resonance for different sizes of the antennas. We sustain the same resonance energy of the antenna (tuned to approximately the molecular resonance of CBP). For larger antennas, we obtain larger signatures, as the field enhancement produced by the antenna grows significantly. We see that the trend is very similar in EELS and extinction, although they differ a bit. This discrepancy could be caused by different mesh sizes of the domains (in the EELS, the mesh was finer around the beam and needed to be finer around the molecules) or by the detuning of extinction and EELS previously discussed in Ref. [95].

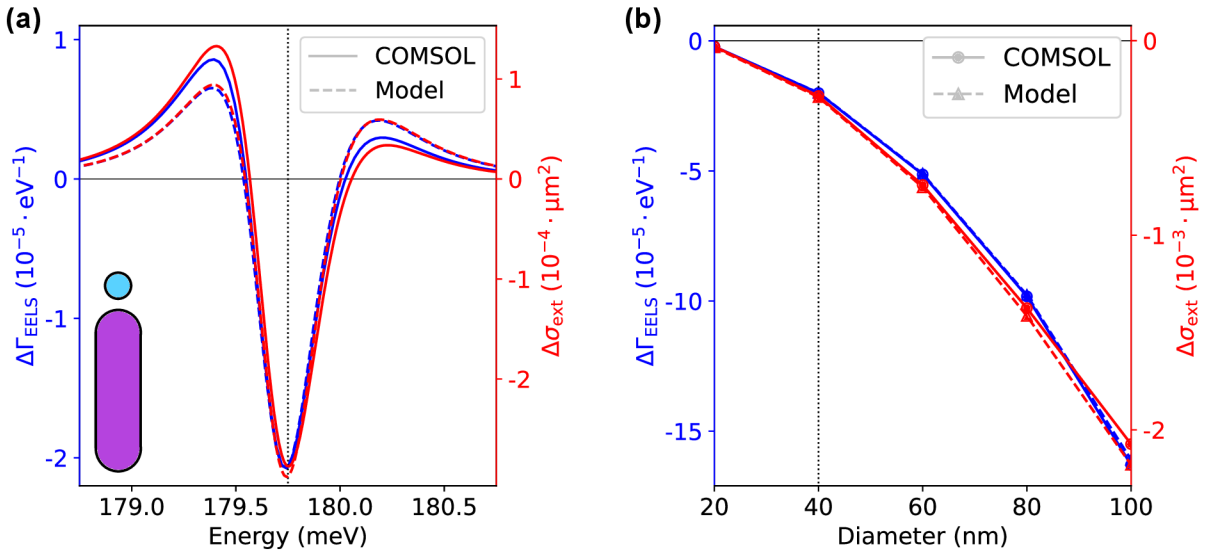

Figure 4.7: (a) Comparison between the molecular signatures in electron energy loss probability (blue) and extinction cross section (red) for a system of hBN antenna and CBP sphere considered in Fig. 4.6 (b). With the full lines, we plot the results from COMSOL simulations, and with dashed lines analytical expressions of Eq. (4.6) and Eq. (4.31) for extinction and EELS, respectively. With the vertical dashed line, we mark the resonance energy of the CBP molecule at approximately 178.8 meV. (b) Molecular signature magnitudes at the energy of the molecular resonance for different sizes of hBN antennas. All antennas were resonantly tuned to approximately the energy of the CBP molecule resonance. The antenna dimensions are in Table. D.3 With circles connected by full lines we plot the results from COMSOL simulations and with triangles connected by dashed lines the analytical results for loss probability contrast of Eq. (4.32) (blue) and extinction contrast of Eq. (4.9) (red). With the vertical dashed line, we mark the values from (a).

For the comparison with the analytical model, we again assume that the field enhancement at the resonance frequency of the molecule ω_{res} is purely imaginary ($\arg(f(\omega_{\text{res}})) = \pi/2$) and write

$$\Delta\Gamma^{\text{r}}_{\text{EELS}} = -\frac{1}{\pi\hbar}\left|E_x^{\text{el,A}}\right|^2\left|f\right|^2\text{Im}\{\alpha^{\text{O}}\}, \tag{4.32}$$

where all the variables on the right-hand side are evaluated at the resonance energy but we did not write the superscript for simplicity. We plot the results of the EELS signature at resonance in Fig. 4.7 (b) and also plot the extinction signatures at resonance evaluated from Eq. (4.9) for the hBN antenna and CBP sphere system. The relative error is largest for the smallest antenna of radius 10 nm, where it is 7% for EELS and 12% for extinction. for the other antennas, it is always under 2% for EELS and under 5% for extinction.

We now focus on the study of the molecular contrasts in spectra. From the analytical model, we assume the mechanisms behind the extinction and EELS to be similar, hence we suppose that contrasts should be the same for both photons and electrons. We define the molecular contrast in the EEL spectra similarly to the extinction cross section contrast [Eq. (4.19)] as a ratio between the molecular signature and the total antenna loss as

$$\delta\Gamma_{\text{EELS}}(\omega) = \frac{\Delta\Gamma_{\text{EELS}}}{\Gamma^{\text{A}}_{\text{EELS}}}. \tag{4.33}$$

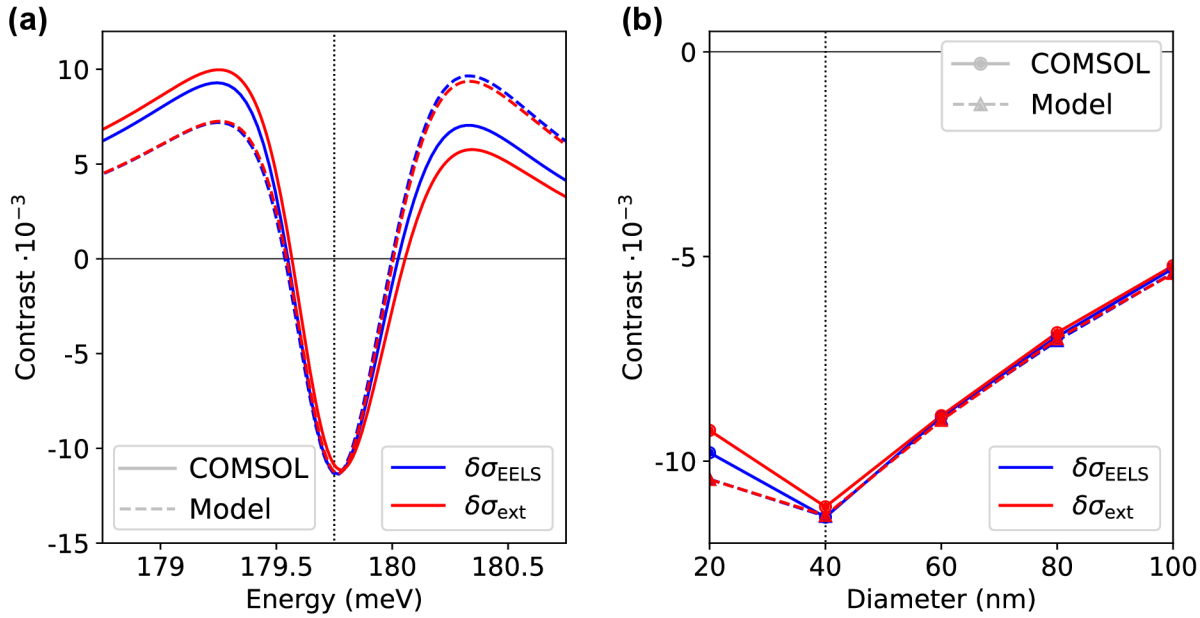

Figure 4.8: (a) Molecular contrasts in electron energy-loss probability (blue) and extinction (red). With the full line, we plot the numerically calculated values from COMSOL and with the dashed line, the analytically calculated contrasts from Eq. (4.33) for EELS and for extinction, we take it from Eq. (4.19). Near the resonance, all the contrasts give us approximately the same values, thus confirming a similar nature of enhancement in both FEELS and SEIRA. With the dashed line, we plot the energy of the molecular resonance of CBP. (b) Molecular contrast at resonance for different sizes of hBN nano-antennas. With blue and red dots connected by the full line, we plot the values of EELS and extinction contrasts, respectively. With the triangles with dashed lines denote the results using Eq. (4.34) for EELS and of Eq. (4.22) for extinction.

We plot the numerically calculated contrast in EEL spectra (obtained from data from Fig. 2.9 for $\Gamma^{\mathrm{A}}_{\mathrm{EELS}}$ and Fig. 4.7 for $\Delta\Gamma_{\mathrm{EELS}}$) for the previously considered system of hBN antenna with 20 nm radius and CBP sphere in Fig. 4.8. We can see that the contrast is about 1% between the signature and the total antenna loss probability. We again compare the contrast with extinction contrast (obtained from Fig. 2.6 and Fig. 4.7) and find that the contrast is the same for EEL spectra and extinction spectra. The contrast is much larger than for the system of the large gold antenna and PDMS molecule (Fig. 4.4). This originates from the small cross section of the hBN antenna relative to the CBP sphere. The only difference between EELS and extinction contrast is their respective scaling with energy, resulting from the distinct natures of the processes.

We compare the contrasts with the analytical models. For extinction contrast, we plug the signature from Eq. (4.31) and the loss probability of the bare antenna from Eq. (2.38) into Eq. (4.33) and for extinction, we take it from Eq. (4.19). For the EEL contrast, we can see that we are able to describe the contrast lineshape and magnitude near the resonance, but there is a difference further away from the resonance. The extinction contrast is described well, similar to the gold antennas with the PDMS molecule of Fig. 4.4 (a). At the resonance, both extinction and EELS with both the model and numerical computation yield the same contrast. The results further confirm the viability of the analytical model approximation for the weakly polarizable object of Eq. (4.31).

We again evaluate the contrasts at the energy of the molecular resonance of CBP at approximately 178.8 meV. We can see that it is the largest for the antenna of radius 20 nm for both EELS and extinction. For larger antennas, the contrasts are approximately the same, confirming the similarity between FEELS and extinction in SEIRA. For the antenna of radius 10 nm, the contrasts differ, which is most likely due to the very small dimensions of the antenna with coarse mesh. We can analytically express the EEL contrast at the resonance with the help of Eq. (4.32) and Eq. (2.38), where in the latter, we evaluate it at the resonance energy of the molecule. We obtain

$$\delta\Gamma^{\mathrm{r}}_{\mathrm{EELS}} = -\frac{\left|f\right|^2}{\left|\alpha_{\mathrm{A}}\right|}\mathrm{Im}\{\alpha^{\mathrm{O}}\} = \delta\sigma^{\mathrm{r}}_{\mathrm{ext}}, \tag{4.34}$$

where we also noted that the molecular contrast at the resonance in EELS is exactly the same as the molecular contrast observed in extinction [Eq. (4.22)]. With this, we can then assume that we only need to know antenna polarizability and the near-field distribution around the antenna to model both molecular signatures and molecular contrast of the enhanced spectroscopies with both photons and electrons. We compare the analytically obtained contrast from EELS with the extinction contrast in Fig. 4.8 (b). Contrasts at the resonance approximately match (the relative error is under 4%.) except for the smallest antennas, where the discrepancy for the antenna of radius 10 nm is under 7% for EELS and under 12% for extinction.

With the analytical formulas for both optical cross section and EELS signatures and contrasts, we now move to design figures of merit for evaluation of the enhanced-spectroscopy performance using the analytical models.

4.4 Figures of merit

In the previous sections, we established analytical expressions for the absorption, scattering, and extinction signatures and contrasts in the SEIRA cross sections using the coupled point-dipoles formalism. We also showed that similar expressions arise for loss probability obtained in electron-energy loss spectroscopy. With the knowledge of the analytical formulas we now focus on the optimization of the antenna for best SEIRA performance depending on the type of collected signal.

There are several aspects of enhanced spectroscopy experiments towards which figures of merit (FOM) can be stated. We can perform the experiment with photon probes or with electron probes. With both types of probes, we can also look at the power lost during the interaction (extinguished power in extinction and electron energy loss in EELS) or the power radiated/scattered.

The detector and sample chosen in the experiment play crucial roles too. When having a poor detector, we are looking for an antenna that gives us the largest molecular signature. When having a good detector but a weakly responding sample, we are targeting the largest contrast.

In all the expressions in Secs. 4.2 and 4.3, the influence of the antenna shape, size, and material in the enhanced spectroscopy is mediated through the antenna polarizability and the field enhancement. We establish figures of merit in the form of dependence of the field enhancement squared on the antenna polarizability. We showed how the

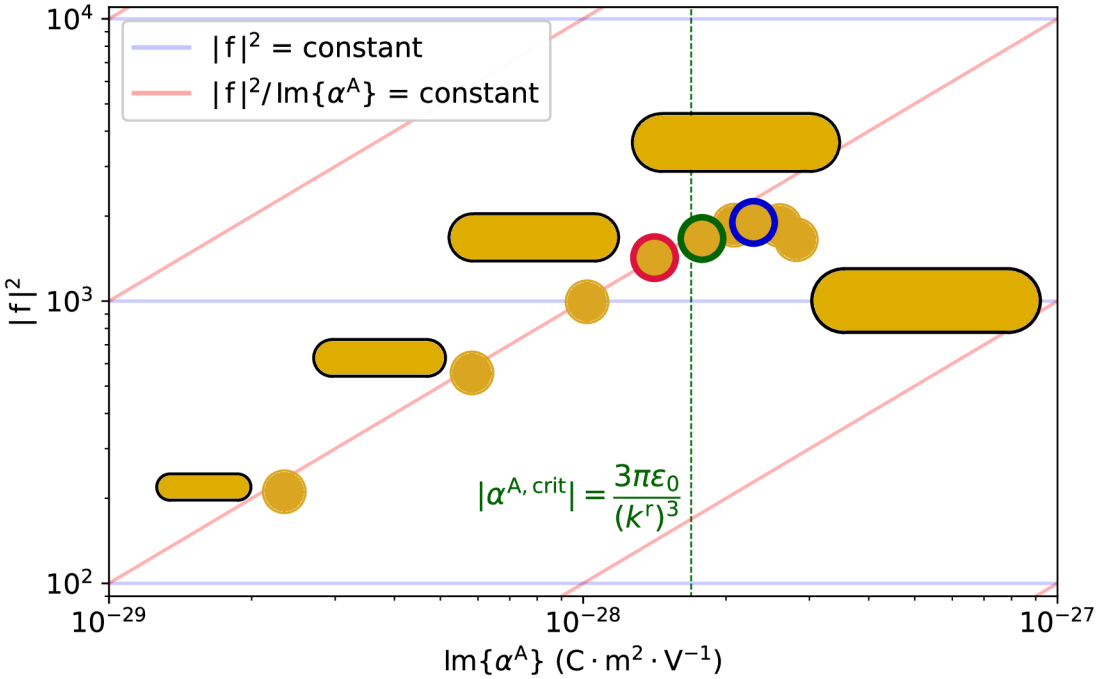

Figure 4.9: Figure of merit for extinction cross section and EELS signatures and contrasts in enhanced spectroscopies. (a) Dependence of the square of the field enhancement $|f|^2$ (evaluated at the resonance energy 0.157 eV and 30 nm from the antenna apex) on the imaginary part of the antenna polarizability $\mathrm{Im}\{\alpha^A\}$ for various gold antennas from Fig. 2.3 (b), for which the dimensions are in Tab. D.2. The diameters of the antennas are increasing from left to right; for some of them, shapes and sizes are schematically depicted in the insets. With the blue horizontal lines, we mark values of constant $|f|^2$. With red diagonal lines, we mark the constant values of the ratio $|f|^2/\mathrm{Im}\{\alpha^A\}$. With the green vertical dashed line, we mark the theoretical value of the polarizability of the critically coupled antenna $\alpha^{A,crit}$ from Eq. (4.16).

molecular signatures and contrasts depend on the antenna's polarizability and the near-field enhancement produced by the antenna. With the analytical expressions, we are now able to state figures of merit for the design of nano-antennas.

Firstly we focus on extinction, which is the quantity measured in a typical transmission experiment. The signatures in both SEIRA extinction and FEELS depend on one parameter of the antenna, which is the near-field enhancement [Eqs. (4.9) and (4.32)]. We plot the values of the field enhancement squared for various gold cylindrical nano-antennas from Fig. 2.3 (b) in Fig. 4.9 as a function of an imaginary part of the respective antenna polarizability with golden dots. We evaluate all the variables at the energy of the molecular resonance at approximately 0.157 eV. At the resonance, $\mathrm{Im}\{\alpha^A\}$ should be equal to $|\alpha^A(\omega_{res})|$, but we consider the fact that the antennas are not precisely tuned to the molecular resonance and not assume the equality. From now on, we will refer to the respective antennas with the value of their diameter (Tab. D.2). With the blue horizontal lines, we mark the values of constant field enhancement. From Eq. (4.6), we see that the largest signature would be for the antenna with the largest $|f^2|$, which happens for the antenna with diameter 80 nm, marked with the blue circle. It is also the antenna with the largest extinction signature [Fig. 4.2].

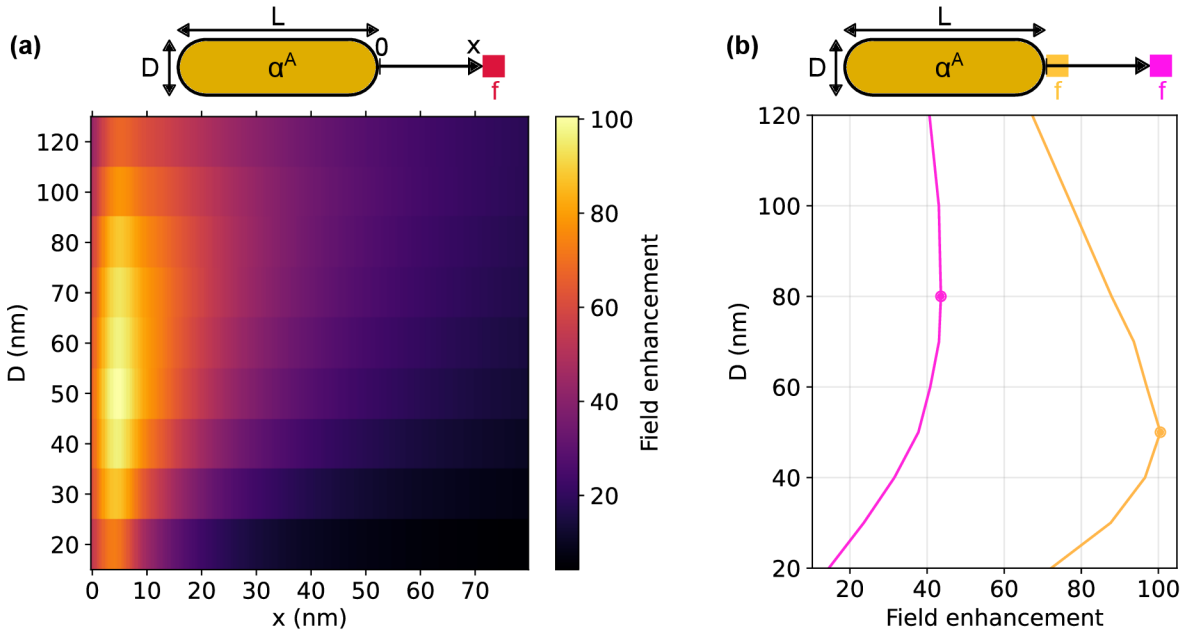

Figure 4.10: (a) Near-field enhancement as a function of distance from the antenna apex x for different antenna diameters D [antennas with diameters and lengths from Fig. 2.3 (b)]. The field enhancement is evaluated at the energy of the molecular resonance at 0.157 eV (7.9 µm). We can see that the largest field enhancements for the antennas are near the apexes (because of the size of the mesh cells, the apex is slightly shifted from $x = 0$ nm). (b) Field enhancement at two different positions for different antennas. With the orange curve, we evaluate it approximately at the antenna apex. With the pink curve, we evaluate it at 30 nm from the apex, where the object center in SEIRA simulations is positioned. The field decays at different rates for different antennas, thus yielding a maximum for antenna of diameter 50 nm when evaluating the field enhancement near the apex, but for antenna for diameter 80 nm, when evaluating 30 nm from the apex. With the dots, we mark the maxima of the respective curves. Data were interpolated for better visibility, as the mesh-cell size is not homogeneous and the points at which the field is evaluated are not equidistant in FDTD.

The contrast (molecular signature in the cross section divided by the total antenna cross section) in SEIRA extinction and FEELS at the energy of the molecular resonance depends on the ratio $|f|^2/\mathrm{Im}\{\alpha^{\mathrm{A}}\}$ [see Eqs. (4.22) and (4.8), where we assumed that for precisely tuned antennas the polarizability at resonance is purely imaginary]. With the red lines, we mark values of constant ratio between the field enhancement squared and antenna polarizability. We can see that the largest value of the ratio is for the antenna of diameter 50 nm, marked with the red circle. We can again compare this result with Fig. 4.4, where the antenna with the largest extinction contrast is the one with diameter 50 nm. We also plot the value of the polarizability for the critically coupled antenna from Eq. (4.16) by the green dashed line. We can see that this value nearly coincides with the polarizability antenna of diameter 60 nm, which is critically coupled. The validity of this formula needs to be verified for other nano-antennas with different shapes and from different materials. For now, it gives us an approximate division line between two regimes of the antennas. On the left-hand side with respect to the green dashed line, we have antennas that have a larger extinction signature than the scattering signature, while on the right-hand side, the scattering signature is larger [Fig. 4.2 (b)].

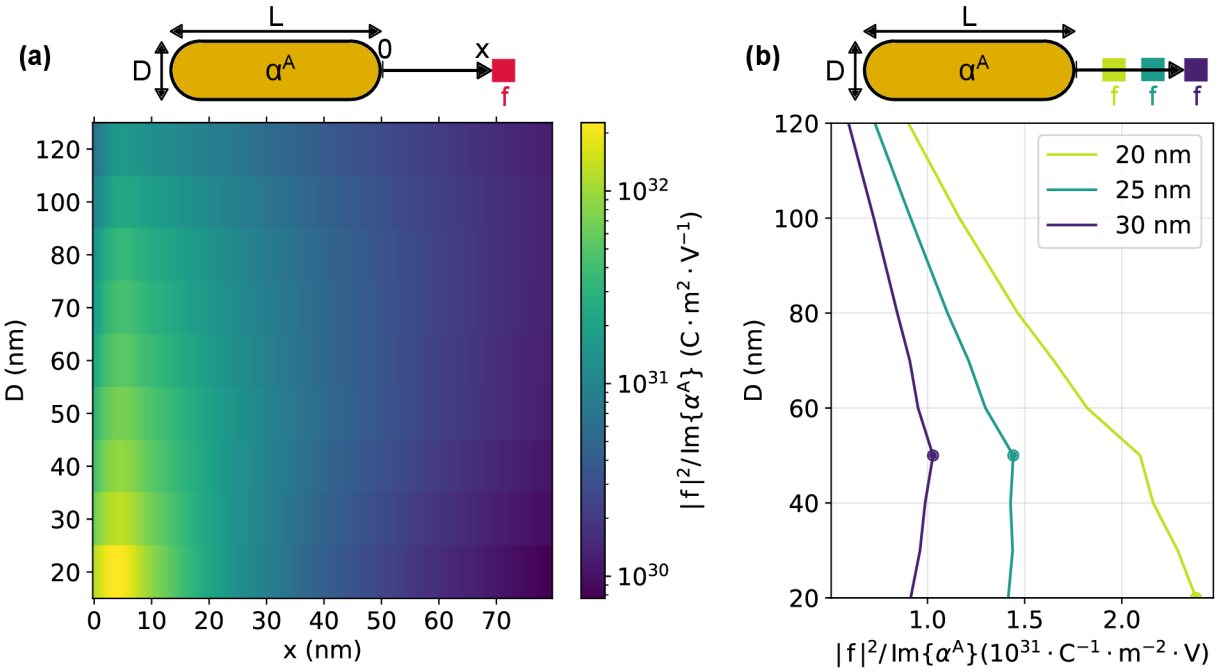

Figure 4.11: (a) Spatial decay of the ratio between the square of the field enhancement and the antenna polarizability, which is proportional to the molecular contrasts. We obtained this data by squaring the spatial decay of the near-field enhancement from Fig. 4.10 and multiplying it with the value of $\mathrm{Im}\{\alpha^{\mathrm{A}}\}$ for respective nano-antennas. This ratio is in the formula for extinction and scattering contrast. We can see that the value of $\left|f\right|^2/\mathrm{Im}\{\alpha^{\mathrm{A}}\}$ is largest for the smallest antennas, as they have smaller polarizability than the larger antennas, and also rises near their apexes, as there is largest $\left|f\right|^2$. (b) The same as in (a), but for three selected distances from the antenna apex x. We can see that for the distance considered in the SEIRA simulations (x = 30 nm) we obtain the largest contrast for antenna of diameter 50 nm, but when approaching closer to the apex, the trend changes and the contrast is largest for the smallest antenna of diameter 20 nm. With the dots, we mark the maxima of the respective curves.

For the simulations of SEIRA and FEELS, we considered the object center to be positioned 30 nm from the antenna apex. Because of the different diameters of the hemispherical apex and sizes of the antennas, even the field decay rate varies between different antennas. We can look at this as a consequence of the form of the field enhancement tensor, where we are changing the polarizability and the distance from the center, where the point dipole is located. Thus the results of the largest signature and contrast are influenced by the considered distance.

We plot the field enhancement for the different sizes of the gold antennas in Fig. 4.10 (a). We set the apex of the antenna as point $x = 0$ nm. Because of the coarse mesh in the simulations near the apexes of the antenna, the apex was in reality shifted, thus the maxima are not precisely at $x = 0$ nm. We can see that the largest field enhancement near the apex of the nano-antenna is for the diameter 50 nm, which is close to the antenna which is critically coupled (antenna of diameter 60 nm). This is in concordance with the previous reports [94]. When looking at the value of the near-field enhancement for the antenna of diameter 50 nm, we can assume [Eq. (4.6)] that the molecular signature would be magnified by the factor $\left|f\right|^2 \approx 10^5$. The near-field decays with the distance from

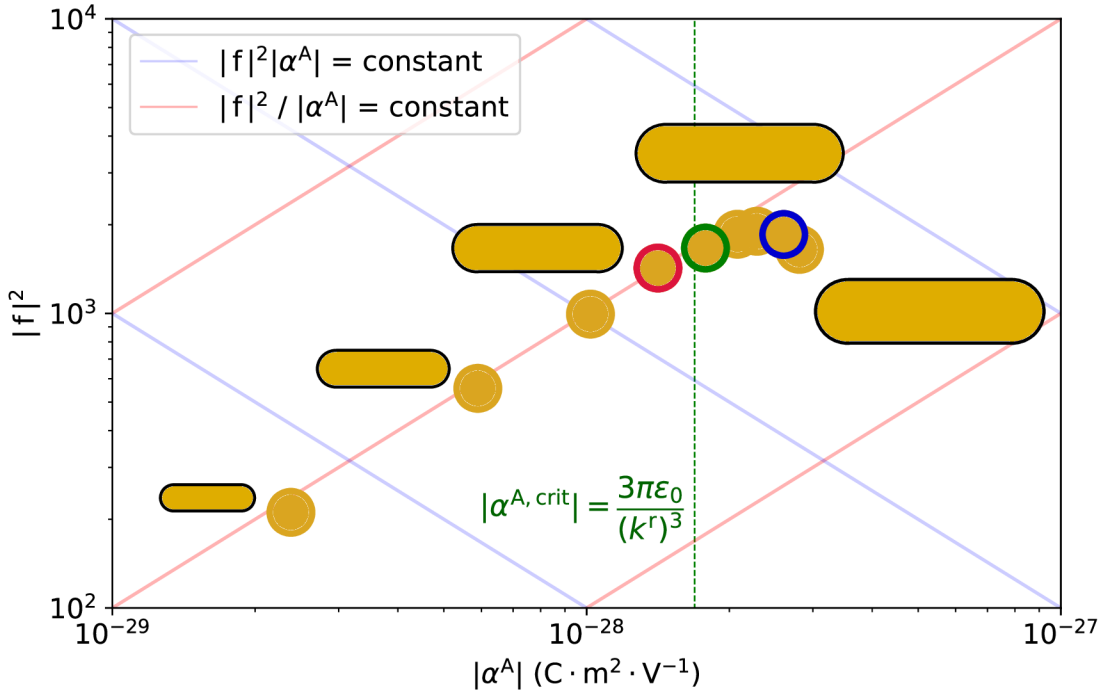

Figure 4.12: Figure of merit for scattering cross section signatures and contrasts in enhanced spectroscopies. (a) Dependence of the square of the field enhancement $|f|^2$ (evaluated at the resonance energy 7.9 µm and 30 nm from the antenna apex) on the magnitude the antenna polarizability $|\alpha^A|$ for various gold antennas from Fig. 2.3 (b), for which the dimensions are in Tab. D.2. With the blue diagonal lines, we mark values of constant product $|f|^2|\alpha^A|$. With the red diagonal lines, we mark the constant values of the ratio $|f|^2/|\alpha^A|$. With the green vertical dashed line, we mark the theoretical value of the polarizability of the critically coupled antenna $\alpha^{A,crit}$.

the antenna apex. When looking at the field enhancement at the point 30 nm from the antenna apex, we can see that it is truly the largest for the antenna of diameter 80 nm, which has the largest extinction signature.

When looking at molecular contrast, we have shown that its magnitude is proportional to $|f|^2/|\alpha^A|$. We take the dependence of $|f|$ for different antennas from Fig. 4.10 and multiply it by $|f|/|\alpha^A|$ and plot the result in Fig. 4.11. From this, we obtain spatial dependence of the molecular contrast for various gold nano-antennas. We can see that for the smallest antenna with the smallest polarizability (polarizabilities with sizes are plotted in Fig. 2.3), we obtain much better contrast near the antenna tip, as proposed previously. When looking at the decay rate of the contrast for different distances, we recognize that for the distance chosen previously (30 nm), the largest contrast is for antenna of diameter 50 nm, as the field decays faster for the one with diameter 20 nm. When going closer to the apex, we can see that the smaller antennas start to have a larger contrast.

When looking at the performance of the antennas in enhanced spectroscopy experiments, where we detect scattered light, we can establish similar FOMs as we did for extinction and EELS. We again plot the values of the field enhancement squared at position 30 nm from the antenna apex, but now we plot their dependence on the magnitude of the antenna polarizability, which enters the scattering cross section in Eq. (2.19). The scattering signature at the resonance frequency in Eq. (4.10) scales with $|\alpha^A|$ and $|f|^2$, thus for the largest scattering signature, a large antenna with large field enhancement

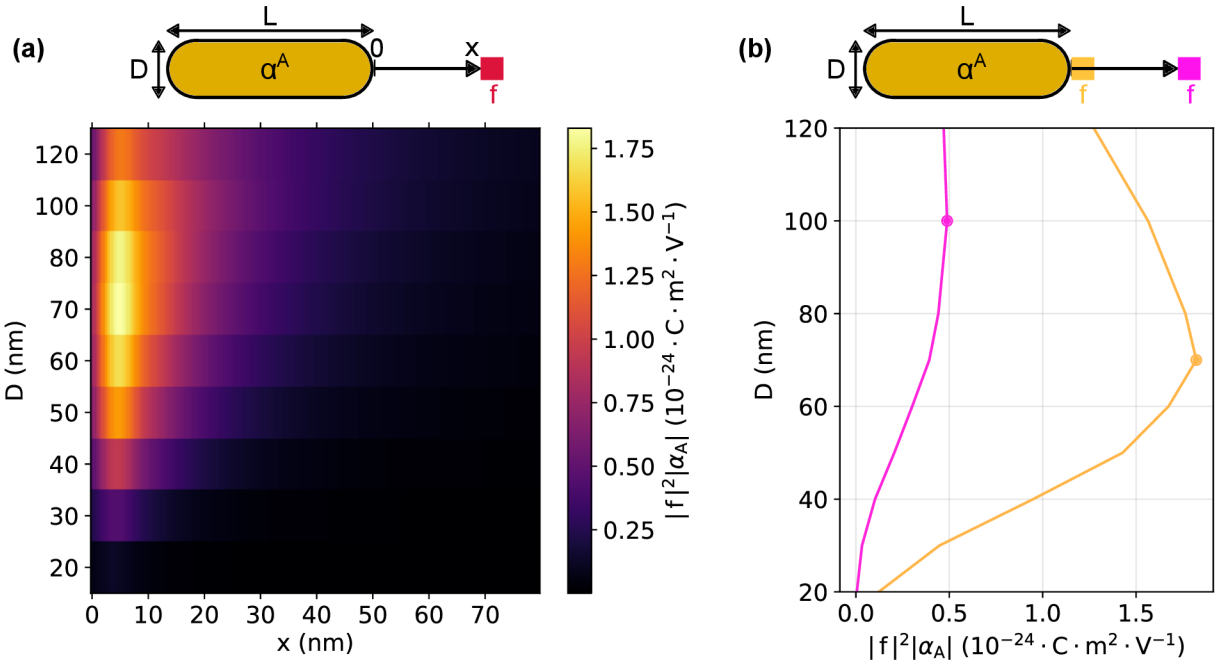

Figure 4.13: (a) Spatial decay of the product $|f|^2|\alpha^{\mathrm{A}}|$ on which the scattering signature at resonance from Eq. (4.13) depends, plotted for various sizes of antennas, labeled with their diameters D. Values of x mark the distance from the antenna apex. (b) Product $|f|^2|\alpha^{\mathrm{A}}|$ for two different positions from the antenna apex, with yellow we plot the values near the antenna apex and with the pink the values 30 nm from the apex. With the dots, we mark the maxima of the respective curves.

would be optimal. With the diagonal blue lines, we plot values of the constant product of $|f|^2|\alpha^{\mathrm{A}}|$, and we mark the dot corresponding to the antenna with the largest value of this product with the blue circle. It is the second largest antenna with diameter 100 nm, which has the largest scattering signature, as we saw in Fig. 4.2 (b). There we have also observed, that the largest scattering signature is for a different antenna than the largest extinction signature (antenna of diameter 80 nm). Nevertheless, the antennas are similar in size, thus one antenna could be used for extinction experiments, where we obtain the largest extinction signature and almost the largest scattering signature, or vice-versa.

With the red diagonal lines, we plot the constant values of the ratio $|f|^2/|\alpha^{\mathrm{A}}|$, which scales the scattering contrast at the resonance energy [see Eq. (4.23)]. The lines are similar to the ones in Fig. 4.9, where we observed the same behavior and largest contrast for antenna of diameter, which is the same for scattering and it is confirmed in Fig. 4.4 (b). We also again mark the critically coupled antenna with the green circle, and with the vertical green line, we plot the theoretical value of the polarizability magnitude. From Figs. 4.9 and 4.12, we can assume that for obtaining the largest contrast (in this considered system of gold antennas of cylindrical shaped tuned to the resonance 0.157 eV), we can choose the same antenna, which is versatile in this point of view.

We can again look at the dependence of the decay rate of the scattering signature as a function of the distance from the antenna apex. In Fig. 4.13 (a), we took the field enhancement of Fig. 4.10 (a), squared it, and multiplied it with the antenna polarizabilities for the respective antennas. We can see that the scattering signature is largest when the object is placed at the apex of the antenna of 35 nm, which we also show in Fig. 4.13 (b). When looking further away from the apex, at a distance 30 nm, where we place the object

in the SEIRA simulations, we obtain the largest value for antenna of diameter 100 nm as previously.

For the decay rate of the scattering contrast, we can look back to Fig. 4.11, where even though we multiply $\left|f\right|^2$ by $\mathrm{Im}\{\alpha^{\mathrm{A}}\}$, we can assume that the relative scaling between antennas is same for $\left|\alpha^{\mathrm{A}}\right|$, as the antennas are tuned or even slightly off-tuned to the energy of the molecular resonance. Thus, the figure would be valid for scattering contrasts and we obtain the same spatial scaling as for extinction, described previously.

With the figures of merit for gold round rod antennas tuned to the molecular resonance of PDMS at 0.157 eV, we can easily design the best antenna for our chosen experiment regarding its size and subsequent polarizability and field enhancement. With the spatial dependence of field enhancement for different antennas and knowledge of the antenna polarizability, we can also choose the best antenna for performance regarding extinction and EELS or scattering signatures and contrasts, when assuming we place our studied sample in different distances. On the other hand, such spatial information about the molecular signatures or contrasts can be used for obtaining information about the field enhancement at the point, when we know where the molecule is placed, or to find out the sample position relative to the nano-antenna apex when we know the field enhancement from simulations.

We now show the figures of merit for different shapes of gold nano-antennas and compare their predicted enhanced-spectroscopy performance. Until now, we were considering cylindrically-shaped antennas with hemispherical apexes. We consider antennas of elliptical cross section, with a constant height 100 nm, for which we change the diameter (semi-minor axis) until we obtain the shape of a disc. Here we study the effects of the local curvature at the end of the nano-antennas on the performance in the enhanced spectroscopies, as the x-dimensions are comparable. All nano-antennas are again tuned to the resonance energy 0.157 eV, thus we also had to elongate them. The dimensions of elliptical antennas are in Tab. D.2.

In Fig. 4.14 (a), we plot the dependence of the field enhancement squared (evaluated at position 30 nm from the antenna apex) on the imaginary part of the antenna polarizability. We also plot the results obtained for the gold rods from Fig. 4.9 for comparison with the elliptical-shaped antennas. We can see that the first elliptical-shaped antenna has similar field enhancement and polarizability as the round-rod antenna of similar dimensions. When making the ellipsis broader, we observe a rapid decrease in the field enhancement. The polarizability is changing for the first few elliptical antennas, but is approaching similar value for the larger ones. This effect can be viewed as a consequence of the length of the antenna in the x-direction, which is almost the same for the antennas (Tab. D.2). With the same polarizability in the x-direction, we can attribute the decrease of the field enhancement to the local curvature, where for the disk, the field is not as localized as for the sharp end of a thinner elliptical nano-antenna.

Overall, the elliptical nano-antennas have similar values of field enhancement as the round rods, but the ones approaching the shape of a disc are worse than even the smallest round rod. The contrast is worse for all the elliptical antennas, as the polarizability (and thus the extinction cross section) is larger than for the round rods, but the field enhancement is smaller.

We can also study the performance of the dimer antennas with a gap previously mentioned in Sec. 2.2.2. We evaluate the field enhancement in the center of the gap and plot the dependence on the $\mathrm{Im}\{\alpha^{\mathrm{A}}\}$. For the smallest antenna, the field enhancement in

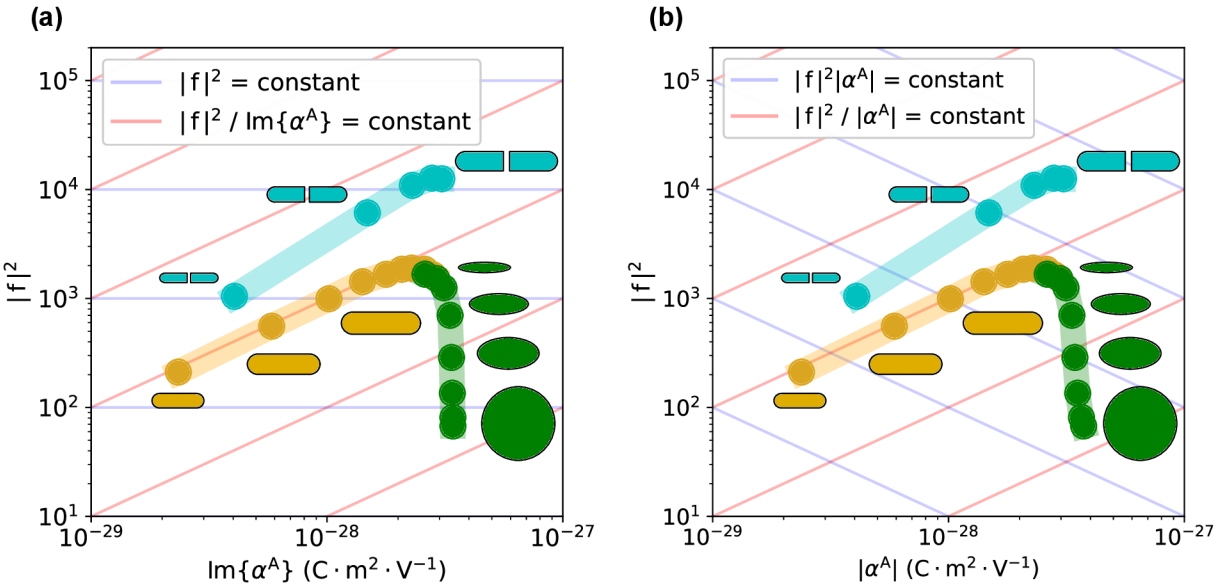

Figure 4.14: (a) Dependence of $|f|^2$ on $\mathrm{Im}\{\alpha^{\mathrm{A}}\}$ for various gold nano-antennas. With the yellow dots, we plot the values for gold rod-like nano-antennas and with the green dots, we plot values for elliptical nano-antennas, which are broadened up until their diameter is the same in length resulting in a disc shape. The field enhancement is evaluated at their resonance energy at approximately 0.157 eV and 30 nm from the antenna apex. With the cyan color, we plot the dimer antennas, where the field enhancement is evaluated in the center of the gap. The shape and dimension of the antennas are schematically depicted by the insets with matching colors. With the blue and red lines, we plot the values of constant $|f|^2$ and the ratio $|f|^2/\mathrm{Im}\{\alpha^{\mathrm{A}}\}$ respectively. (b) Same as in (a), but we plot the dependence on $|\alpha^{\mathrm{A}}|$. The red and blue lines are constant values of $|f|^2|\alpha^{\mathrm{A}}|$ and $|f|^2/|\alpha^{\mathrm{A}}|$ respectively. We can see that for some of the larger elliptical shape antennas, $\mathrm{Im}\{\alpha^{\mathrm{A}}\} \neq |\alpha^{\mathrm{A}}|$.

the gap is comparable with the field enhancement at the ends of gold round rods, but for larger diameters, the field enhancement in the gap is one order of magnitude larger. With the guiding blue horizontal and red diagonal lines, we can see that for the dimer antennas, the model predicts larger signatures and contrasts compared to the round rod antennas or elliptical antennas in extinction and EELS.

In Fig. 4.14 (b) we plot the dependence of the field enhancement on $|\alpha^{\mathrm{A}}|$. We compare the performance of the gold round rods with the elliptical antennas, for which we can see that we again obtain similar values of contrasts and signatures, but for the larger, disc-like nano-antennas, the field enhancement decreases rapidly, resulting in a decrease in both signature and contrast. We can notice that the values of $|\alpha^{\mathrm{A}}|$ differ a bit from the values of $\mathrm{Im}\{\alpha^{\mathrm{A}}\}$ as the ellipsis cross sections were very broad in energy and the resonance was not exactly tuned to the molecular one.

We also plot the dependences of $|f|^2$ on $|\alpha^{\mathrm{A}}|$ for dimer antennas. The two smaller dimer antennas predict similar values of the scattering signature, but the contrast is larger. For the three biggest dimer antennas, the values of both scattering signature and contrast are larger than for all of the other shapes considered.

Overall, dimer antennas seem to be the best candidates for both extinction (and EELS) and scattering experiments of enhanced spectroscopy. Particularly the larger dimer an-

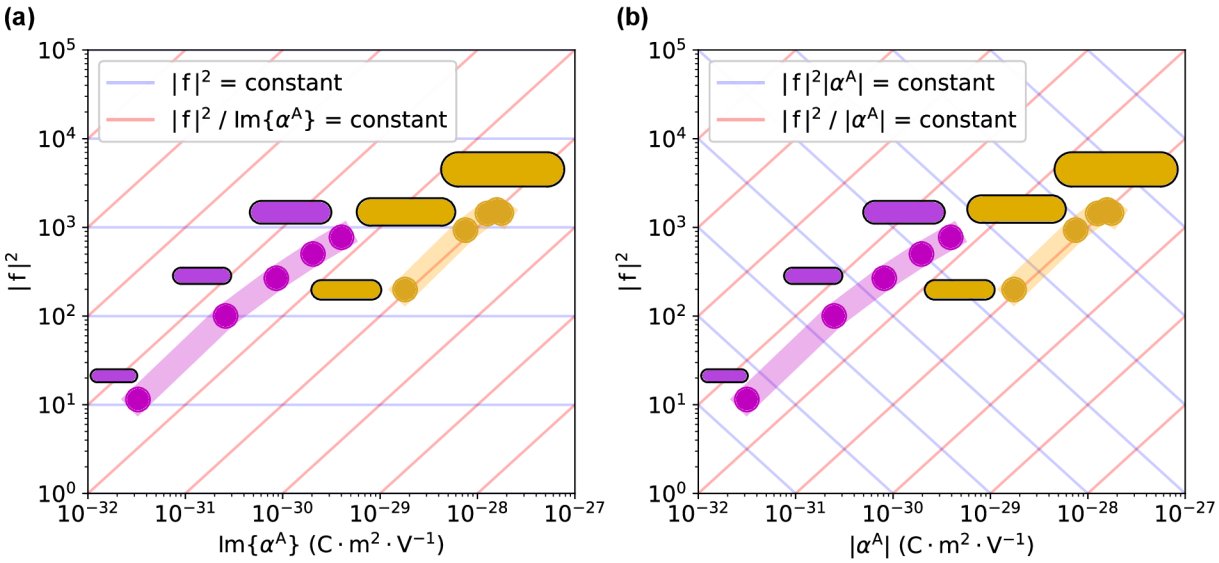

Figure 4.15: (a) Dependence of $\left|f\right|^2$ on $\mathrm{Im}\{\alpha^{\mathrm{A}}\}$ for gold nano-antennas (yellow) and hBN antennas (magenta). We are changing the diameters of the antennas, but they match for hBN and gold in order, to be comparable. The field enhancement is evaluated at the resonance energy 0.18 eV and 30 nm from the antenna apex, therefore the gold antennas are different ones than those considered in previous FOMs. We again plot the isolines with red and blue, as in Fig. (b) Same as in (a), but we plot the dependence on $\left|\alpha^{\mathrm{A}}\right|$.

tennas predict the largest values in both signatures and contrasts. Albeit the large ellipsis shapes and disc nano-antennas showed poor performance, they may be, for example, utilized for the case of a very weakly interacting sample, with which the whole antenna would be covered and the field, which is very non-localized compared to the sharp tip of the nanorod would enhance the signal from a larger volume of the sample.

We now focus on antennas tuned to the molecular resonance of CBP at approximately 0.18 eV. In Fig. 4.15 (a), we plot the values of the $\left|f\right|^2$ for different series of gold round rods (dimensions are in Tab. D.3). We choose different golden nano-antennas, for the comparison of hBN nano-antennas to be fair, as they will be tuned to the same resonance frequency and also will have the same diameter and thus the same shape of their apex. With the same diameter we can exclude the effect of the local curvature on the field enhancement. The major difference between these two antennas is the nature of their resonance (plasmonic in gold and phononic in hBN) and their different length (in order of micrometers for gold antennas and hundreds of nanometers for hBN antennas). The dimensions of hBN antennas, which were previously dealt with in Sec. 4.3 are in Tab. D.3. We plot the values of the field enhancement for hBN nano-antennas previously considered in Fig. 4.7. We can immediately see, that their polarizabilities are a couple of orders of magnitudes smaller than the gold round rods (which results in smaller cross sections, as we showed in Fig. 2.6), but the field enhancements squared are comparable. We have the same color legend of isolines of constant values of $\left|f\right|^2$ and $\left|f\right|^2/\mathrm{Im}\{\alpha^{\mathrm{A}}\}$ as in previous figures. With this figure of merit, we can assume that the signatures appearing in spectra would be comparable in magnitude, albeit smaller for hBN antennas, but the contrast would be much larger in the hBN antennas. The hBN antenna with the largest contrast is the second smallest one, which is in concordance with Fig. 4.8. We can also recognize that even for the gold antennas, the one with radius 20 nm has the largest contrast.

In Fig. 4.15 (b), we plot the values of field enhancement squared as they depend on the magnitude of the polarizability at resonance. In the scattering experiment, the larger signature would be for gold antennas, as it scales with $\left|\alpha^{\mathrm{A}}\right|$, but the contrast would be again the best for hBN antennas as it scales with $1/\left|\alpha^{\mathrm{A}}\right|$.

With the figures of merit, we now have a comparison of antenna performances in enhanced spectroscopies. These FOMs are general for the case of a weakly scattering object enhanced by the near-field of nano-antenna tuned to certain resonance energy. Thus when comparing different antennas at the same resonance frequency, the procedure for recognizing the antenna with best performance would be the same.

5 Conclusions and outlook

This diploma thesis focused on the theoretical description of enhanced spectroscopy, which utilized strong-near fields produced by resonant nanostructures in signal enhancement when studying minute amounts of analytes. One of its aims was the comparison of performance in different experiments (scattering and extinction or electron energy-loss spectroscopy) with nano-antennas made of various sizes and materials (relatively small hBN antennas and relatively large gold antennas) and different shapes (round-rods, ellipses, and dimer antennas).

The first chapter reviewed the electrodynamics and introduced relations needed for the next derivations. With the help of the relations, we were able to perform an approximation of a discrete charge distribution in the form of a point dipole interacting with an external field source. Then we focused on a material response and introduced Lorentz and Drude oscillator models for different materials, which were then used throughout the thesis. Lastly, we introduced the concept of nano-antenna and reviewed some of its aspects and properties.

In the second chapter, we discussed the interaction of a point dipole with external sources of electric field. Firstly we focused on the interaction with a second nearby dipole, after which the two dipoles formed a coupled system. This coupled-dipoles formalism is used for modeling the response of a system consisting of a nano-antenna and a molecular sample, used for enhanced spectroscopy experiments. Under the assumption of a weakly interacting sample that is either small or weakly polarizable (which coincides with the studied molecular sample in enhanced spectroscopy), we expanded the electric field radiated from the coupled dipoles into an infinite series consisting of multiple scattering events between the nano-antenna and the molecular sample. Then we moved back to the description of just one dipole, which is induced by a plane electromagnetic wave. We defined the optical cross sections and then showed the results of numerical calculations of various nano-antennas. We showed how the cross sections depend on the antenna polarizability, into which is projected its material and shape, Next, we briefly reviewed electron energy-loss spectroscopy, showed how we can analytically express the field of a relativistic electron, and introduced the analytical expression for the loss probability. We then expressed the probability that an electron would lose energy towards inducing a dipole. We also pointed out the fact that the relations are similar for EELS and extinction. Then we again showed results of numerical computations, where we compared the polarizabilities obtained by either the dipole expansion in EELS with the dipole expansion by a plane wave illumination. Lastly, we presented numerically calculated EEL spectra and discussed the validity of the dipole expansion with the distance of the electron beam.

In the third chapter, we reviewed infrared vibrational spectroscopy methods, with the main focus on enhanced absorption spectroscopy studying small amounts of analytes. We discussed previous results obtained in the field of resonant surface-enhanced infrared absorption (SEIRA) where the plane wave illumination is considered and then focused on the recently emerged possibility of studying vibrational samples within a transmission electron microscope in electron energy-loss spectroscopy. Similarly to the light-base spectroscopies, even the EELS suffers from a subsequent loss of a signal when studying small samples, thus field-enhanced EELS was proposed.

In chapter four, we introduced the analytical model for explaining SEIRA signatures for a weakly interacting sample, previously derived in Ref. [11]. This model assumes that

the signatures are based on interference between the incident illumination (in extinction) and the field scattered directly by the antenna (in scattering) with one of the terms of the infinite series of scattering events. This one term encompasses the double scattering event between the antenna and sample. We showed a comparison of the numerical results of signatures in optical cross sections and compared them with the analytical model and achieved a very good match. Then we focused on relative contrasts in the cross sections and the explanation of the flip in absorption cross section signatures sign. We showed that there are two contributions to the total absorption signature and its total value is given by the interplay between the field-enhanced object absorption and the change in the antenna absorption given by the interaction with the object. Then, we applied the approximative formalism to the field-enhanced electron energy loss spectroscopy and we compared the results with the results obtained from numerical calculations, where we also compared molecular signatures in EELS and extinction. We showed that the scaling is similar and when considering the loss probability and extinction cross section contrasts, we obtained the same values. The last part was dedicated to establishing figures of merit (FOMs) based on the theoretical model, where we studied the performance of various nano-antennas with respect to their polarizabilities and near-field distribution. With these FOMs, we were able to resolve the enhancement of the signal in different scenarios of experiments (scattering or extinction and EELS) for various nano-antennas.

In this last section, we focus on a future outlook, where we discuss some aspects that were not considered and studied in this thesis.

Firstly, we considered a system of nano-antenna and weakly polarizable object, but the case of a strongly polarizable object, resulting in the strong coupling of the system, could also be studied. With the model, we considered a simple case where all the polarizations were in one direction and we considered the molecular sample to be a small sphere. Other steps could be considering a molecular layer and modeling its polarizability analytically via the core-shell model.

An interesting system to study, considering the results of FOMs, would be hBN dimer antennas, which would provide relatively large contrast, similar to the hBN nanorods, but also large field enhancement as the gold dimers. For the dimers, the proper modeling of the polarizability (by two coupled dipoles and not just one effective dipole) could be done, and the effects of different shapes of the antennas forming the dimer and the gap shape could also be an interesting topic of study.

For the electron-based spectroscopies, cathodoluminescence could a promising candidate for studying samples. It should be possible to model cathodoluminescence similarly to the scattering cross section. Infrared cathodoluminescence is not very common, but the results of the theoretical model are not bound just to the infrared region but different (e.g. excitonic) samples could be studied. In EELS, the feasibility of exciting higher-order modes within the nano-antenna could also be interesting. In EELS, we did not provide results for gold antennas, where the effects of a dipole approximation would not be negligible, as the field would not be homogenous within the nano-antenna as for a relatively small hBN antenna. Some effective position of the distorted dipole would then need to be established.

Appendices

A Fourier transform

A.1 General Fourier transform

The Fourier transform is an integral transform used for the decomposition of a function into the basis of sinusoidal functions. In many fields, e.g. in crystallography, mathematics, or electrotechnics, different conventions are used. We adapt formalism from Ref. [96]. The Fourier transform of a function that is dependent on three space coordinates $\mathbf{r} = (x, y, z)$ and time t, can be written as

$$\mathrm{FT}\{f(\mathbf{r},t)\} = \mathcal{F}(\mathbf{k},\omega) = \iiiint f(\mathbf{r},t)\mathrm{e}^{-\mathrm{i}(\mathbf{k}\cdot\mathbf{r}-\omega t)}\mathrm{d}^3\mathbf{r}\mathrm{d}t, \tag{A.1}$$

and the inverse Fourier transform of a function dependent on Fourier coordinates $\mathbf{k} = (k_x, k_y, k_z)$ and ω is

$$\mathrm{FT}^{-1}\{\mathcal{F}(\mathbf{k},\omega)\} = f(\mathbf{r},t) = \frac{1}{(2\pi)^4}\iiiint \mathcal{F}(\mathbf{k},\omega)\mathrm{e}^{\mathrm{i}(\mathbf{k}\cdot\mathbf{r}-\omega t)}\mathrm{d}^3\mathbf{k}\mathrm{d}\omega. \tag{A.2}$$

Relations can be also written for the Fourier transform for derivatives

$$\mathrm{FT}\left\{\frac{\partial f(\mathbf{r},t)}{\partial t}\right\} = -\mathrm{i}\omega\mathrm{FT}\{f(\mathbf{r},t)\}, \tag{A.3}$$

$$\mathrm{FT}\left\{\frac{\partial f(\mathbf{r},t)}{\partial x_i}\right\} = \mathrm{i}k_i\mathrm{FT}\{f(\mathbf{r},t)\}. \tag{A.4}$$

When considering two real functions of time, we can obtain so-called Rayleigh-Parseval theorem which reads [97]

$$\int f_1(t)f_2(t)\mathrm{d}t = \int F_1(\omega)F_2^*(\omega)\mathrm{d}\omega = \int \mathrm{Re}\{F_1(\omega)F_2^*(\omega)\}\mathrm{d}\omega. \tag{A.5}$$

A.2 Fourier transform of electromagnetic fields

By employing the Fourier transform, we can transform Maxwell equations [Eqs. (1.2-1.3) and (1.7-1.8)] to the Fourier space. In the absence of sources, the equations read

$$\varepsilon_0\varepsilon_\mathrm{r}\mathbf{k}\cdot\mathcal{E}(\mathbf{k},\omega) = 0, \tag{A.6}$$
$$\mathbf{k}\cdot\mathcal{B}(\mathbf{k},\omega) = 0, \tag{A.7}$$
$$\mathbf{k}\times\mathcal{E}(\mathbf{k},\omega) = \omega\mathcal{B}(\mathbf{k},\omega), \tag{A.8}$$
$$\mathbf{k}\times\mathcal{B}(\mathbf{k},\omega) = -\varepsilon_0\varepsilon_\mathrm{r}\mu_0\mu_\mathrm{r}\omega\mathcal{E}(\mathbf{k},\omega). \tag{A.9}$$

B Green's function

B.1 Green's function of general differential equation

Let us consider an ordinary linear differential equation with a differential operator $O(\mathbf{r})$ acting on a function $f(\mathbf{r})$. We suppose that the differential equation is inhomogeneous with a source term $Q(\mathbf{r})$,

$$O(\mathbf{r})f(\mathbf{r}) = -Q(\mathbf{r}). \tag{B.1}$$

We introduce the Green's function of this differential equation as a response to the impact of a point source.

$$O(\mathbf{r})G(\mathbf{r},\mathbf{r}') = -\delta(\mathbf{r}-\mathbf{r}'), \tag{B.2}$$

where $\delta(\mathbf{r}-\mathbf{r}')$ is the Dirac's delta function[1]. With the help of Green's function, we can immediately assume the solution of this differential equation in the form

$$f(\mathbf{r}) = \int G(\mathbf{r},\mathbf{r}')Q(\mathbf{r}')\mathrm{d}V'. \tag{B.3}$$

If we plug this solution back into our differential equation, we show that it is indeed fulfilled.

$$O(\mathbf{r})\int G(\mathbf{r},\mathbf{r}')Q(\mathbf{r}')\mathrm{d}V' = -\int \delta(\mathbf{r}-\mathbf{r}')Q(\mathbf{r}')\mathrm{d}V' = -Q(\mathbf{r}). \tag{B.4}$$

B.2 Green's function of the Helmholtz equation

The Helmholtz equation is widespread in many fields. In its homogeneous form, it can be viewed as a solution of eigenvalues k for the Laplace operator ∇^2. We consider an inhomogeneous case with the source term on the right side $Q(\mathbf{r})$

$$(\nabla^2 + k^2)f(\mathbf{r}) = -Q(\mathbf{r}). \tag{B.5}$$

According to Eq. (B.2), the solution of this equation for a point source located in $\mathbf{r} = \mathbf{r}'$ is

$$(\nabla^2 + k^2)G(\mathbf{r},\mathbf{r}') = -\delta(\mathbf{r}-\mathbf{r}'). \tag{B.6}$$

If we assume unbound and homogeneous space, the Green's function can only depend on the distance $R = \left|\mathbf{r}-\mathbf{r}'\right|$. We then rewrite $G(\mathbf{r},\mathbf{r}') = g(R)$. By transforming the previous equation to the spherical coordinates and realizing that the function depends only on R, we get (for $R \neq 0$)

$$\left(\frac{1}{R}\frac{\partial^2}{\partial R^2}R + k^2\right)g(R) = 0. \tag{B.7}$$

[1] Dirac's delta function is a distribution defined as $\delta(\mathbf{r}-\mathbf{r}') = \begin{cases}\infty, & \text{if } \mathbf{r}=\mathbf{r}'.\\ 0, & \text{otherwise.}\end{cases}$

The general solution of this equation is in the form

$$g(R) = C\frac{\mathrm{e}^{\mathrm{i}kR}}{R} + D\frac{\mathrm{e}^{-\mathrm{i}kR}}{R}. \tag{B.8}$$

We choose only the solution that depends on $\mathrm{e}^{\mathrm{i}kR}$, as we suppose that $k > 0$ and we want a diverging wave. After integration of the Green's function over a sphere with an infinitesimal volume and applying the divergence theorem, we get a value of parameter $C = 1/4\pi$.

The Green's function of the Helmholtz equation then reads

$$G(\mathbf{r}, \mathbf{r}') = \frac{\mathrm{e}^{\mathrm{i}kR}}{4\pi R}. \tag{B.9}$$

.

C Numerical simulations

C.1 Finite-difference time-domain method

For part of the calculations of the interaction of nanostructures with plane electromagnetic wave in this thesis, commercial software based on the finite-difference time-domain (FDTD) method, Ansys Lumerical FDTD (Ansys, Inc) was used. As the name states, the finite-difference method is used to solve partial differential equations by substituting the derivatives with finite differences. FDTD Lumerical is based on the time domain solution of Maxwell's equations, employing temporal and spatial discretization of the problem [98]. The considered system is divided into discrete rectangular cells, often called Yee cells, named after one of the authors of the FDTD algorithm [99]. For more information about the FDTD computational scheme and all the possibilities of simulations, we refer the reader to the Lumerical Learning Center [100].

For simulating the electromagnetic illumination we positioned our nanostructure inside the total-field scattered-field (TFSF) source, which illuminates its insides with a plane wave. This source divides the simulation domain into two regions: (1) Total field region, which is located inside the surface of the source, where is both the incident field and the field scattered from the structure, and (2) Scattered field region, where only the scattered field is included. For obtaining absorption cross section, we placed a monitor inside the TFSF source, so it would record inward flowing power from the source and outward flowing power, which is reduced by the absorbed power. From this monitor, we are able to obtain absorption cross section σ_{abs}. We placed a second monitor outside the TFSF source, where the outward flowing power is given just by the scattered field. This monitor grants us the scattering cross section σ_{sca}. We show the simulation layout in Fig. C.1 (a). We assumed x-polarization of the incident field, which is propagating in the z-direction and a broadband IR source (wavelength from 5 µm to 11.2 µm). We exploited the symmetries of the simulation and by imposing boundary conditions (symmetric in the y-direction and anti-symmetric in the x-direction), we reduced the simulation volume by a factor of 4. We did not consider any substrate, the surrounding medium was assumed to be air $\varepsilon = 1$. For evaluating quantities needed for evaluating the SEIRA model, we followed the approach from Ref. [11] and did four types of simulations, which we will now detail. First, we performed a simulation of a nano-antenna without any surrounding objects. We placed the power-absorbed (PA) monitor inside the TFSF source. The monitor records the distribution of the electromagnetic field and the refractive index in each mesh cell. We show the simulation layout in Fig. C.1 (b). With these quantities, we were able to obtain the dipole moment of the nano-antenna, following the approach from Ref. [101]. Within this approach, evaluation of the exact multipole moments was implemented into Matlab code. We assumed just the dipole contribution, the dipole moment can be expressed using Eq. (2.34). The integration is performed over the volume of the antenna V. The induced current density was calculated from Eq. (2.35), for which the electric field and relative permittivity were obtained from the PA monitor. The integration could have been performed, as the induced currents are zero everywhere outside the antenna, thus the only contribution to the dipole moment comes within the volume of the antenna. With the dipole moment, we can substitute the response of the antenna with the response of a point dipole. We label this simulation as NP (from "no particle").

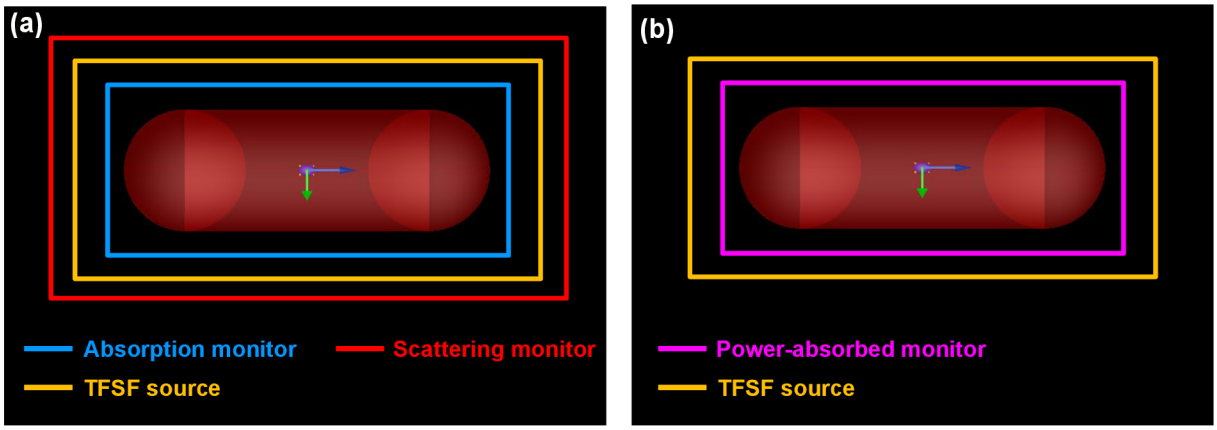

Figure C.1: (a) Simulation layout used for calculating absorption and scattering cross sections. The nanostructure is illuminated by a plane wave, which is polarized along the x-axis and propagates in the z-axis. The source of the plane wave is the total-field scatter-field (TFSF) source (yellow). The absorption monitor (blue) is placed inside the source to record dissipated power. The scattering monitor (red) is placed outside the source to record radiated power. (b) Simulation layout used for monitoring the distribution of electromagnetic field and refractive index. The nanostructure is again illuminated by the TFSF source. Inside the source, we place a power-absorbed monitor, which records the distribution of the refractive index and electromagnetic fields.

A second simulation was done to obtain the polarizability of the antenna. We performed a simulation of an empty domain with just the source and obtained the incident field at the center of the antenna, where the point dipole is situated. The polarizability was then obtained from Eq. (1.37).

Third and fourth simulations were performed to calculate the response of the antenna and object. As we are using the mirror symmetry, we assume two spherical objects situated at the apexes of the antenna. The center of the objects is situated 30 nm from the tip of the antenna. In the third simulation, we considered objects to be absorbing, characterized by the Lorentz model dielectric function (1.44). From this simulation, we obtained cross-sections of the antenna-object system accounting for the response of the antenna resonance and connected molecular signature in the spectrum. We label this simulation as RES (from "resonant object").

Extracting the molecular feature from the spectra is not as straightforward as it may seem. As we show in Sec. 4.1, because of the redshift introduced by the background permittivity of the molecular sample, after subtracting NP simulation from RES simulation, we obtain distorted lineshape [Fig. 4.1 (b)]. In Ref. [4], a smoothing algorithm was used to obtain the plasmonic peak, which can then be subtracted from the RES simulation to obtain baselined molecular features.

We performed a fourth simulation, where we again considered the spherical objects but instead of characterizing them with a resonant dielectric function, we characterized the objects just by the background permittivity of the object $\varepsilon_\infty^{\mathrm{O}}$ from the Lorentz model. Because of this background, the antenna resonance is red-shifted and we can subtract it from the absorbing NP simulation to obtain SEIRA spectra. In Fig. 4.1 (b), we show that the lineshape is less distorted than after subtraction of NP simulation and the molecular feature in the form of a dip is very pronounced. We label this simulation as BG (from "background").

The polarizability of a small nanosphere, approximating the molecules could be obtained similarly as the antenna polarizability. As we are considering a sphere with a radius of 10 nm and we are studying the response in the infrared region, we approximate the polarizability by the formula for quasistatic polarizability of a small sphere in the form

$$\alpha = 4\pi\varepsilon_0\varepsilon_\mathrm{m}a^3\frac{\varepsilon_\mathrm{r}-\varepsilon_\mathrm{r,m}}{\varepsilon_\mathrm{r}+2\varepsilon_\mathrm{r,m}}, \tag{C.1}$$

where a is the sphere radius, $\varepsilon_\mathrm{r,m}$ is the dielectric function of the surrounding medium and ε_r is the dielectric function of the sphere material. For a sphere, it is isotropic, so the polarizability tensor is diagonal with identical components.

C.2 Finite element method

C.2.1 Plane-wave illumination simulations

Finite-element method (FEM) based software Comsol Multiphysics [102] is another possibility for studying the interaction of electromagnetic fields with more complex geometries. FEM is a widely used method for solving differential equations numerically. It takes advantage of dividing the system into small finite-sized elements (mesh). Several comparative studies based on simulation time, accuracy, convergence, and computational demandingness were carried out, showing the pros and cons of FEM and FDTD [103, 104]. One main disadvantage of FDTD is its rectangular mesh, which coarsely describes curved geometries. In comparison, in Comsol, there is a possibility for different mesh-cell shapes.

Similarly to FDTD, plane-wave illumination of a structure can be implemented in Comsol. By recording power flow across boundaries, the scattered power can be computed. Absorption can be obtained by integrating the dissipated power within the structure. In this section, we describe the simulations of a plane-wave illumination implemented in Comsol.

We use the Radio Frequency Toolbox implemented in Comsol. We assume a box-shaped simulation domain. It has to be large enough (at least half a wavelength) for electromagnetic fields. The medium is assumed to be the vacuum, $\varepsilon = 1$; we do not account for the presence of the substrate, although it is mandatory to support the nanostructures in the transmission experiment.

The whole simulation domain is enclosed by swept layers (we typically use five of them), on which are imposed Perfectly-Matched Layer (PML) boundary conditions. PMLs, sometimes called sponge layers, are used to mimic an open simulation domain, where there are no reflections from the borders. In the frequency domain, PMLs transform coordinates into complex-valued ones. This transformation makes waves flowing such domains absorbed and fully attenuated at the last layer, thus forbidding reflections.

The whole simulation is divided into discrete mesh elements, which are shaped as tetrahedrons, using Free tetrahedral. The size of the mesh elements should be, for a typical electromagnetic simulation, about one-tenth of the wavelength considered. Finer mesh refinement needs to be defined around regions, where large or rapidly-changing electromagnetic fields are expected. In our considered simulations, the refinement is typically needed in the vicinity of the nano-antenna and the electron beam. As the real

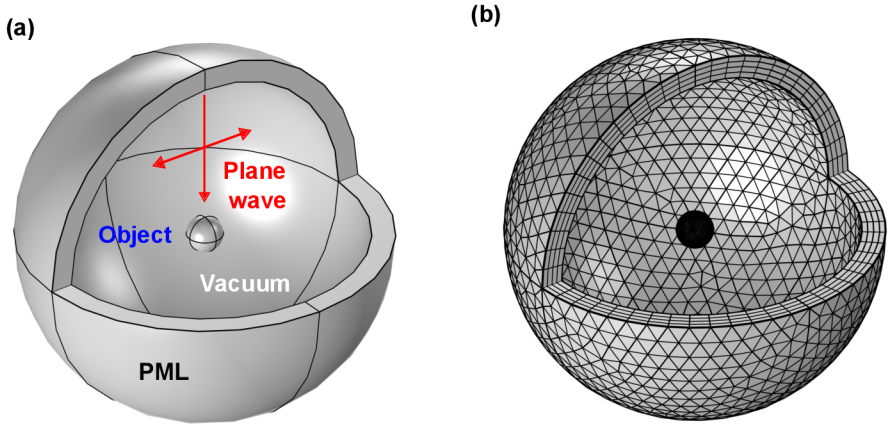

Figure C.2: (a) Simulation layout in COMSOL. An object is placed inside the simulation domain filled with the vacuum. The source of the electromagnetic field is a plane wave, and the whole simulation is enclosed within boundaries onto which PERFECTLY-MATCHED LAYER boundary conditions are imposed. (b) Mesh of the simulation. The object has finer mesh, as we expect greater and fast-changing fields nearby it. The PMLs are swept with five layers.

phenomena do not depend on any artificial mesh, we need to perform convergence tests with respect to the size of the simulation domain and refinement of the mesh elements, until the computed values converge. The simulation layout is depicted in Fig. C.2.

In COMSOL following equation in ELECTROMAGNETIC WAVES interface is solved to obtain distribution of the complex, frequency-dependent electric field $\mathbf{E}$

$$\frac{1}{\mu_\mathrm{r}}\nabla \times (\nabla \times \mathbf{E}) - k_0^2 \varepsilon_\mathrm{r} \mathbf{E} = \mathbf{0}, \tag{C.2}$$

where μ_r is relative permeability, ε_r the dielectric function, k_0 is the free-space wavenumber and ω angular frequency.

We define the incoming electromagnetic wave as a BACKGROUND FIELD in the form of a wave, polarized in x-direction and propagating in z-direction as

$$\mathbf{E} = \mathbf{E}_0 \mathrm{e}^{-\mathrm{i}kz}, \tag{C.3}$$

and we chose the amplitude $|\mathbf{E}_0| = 1$.

The scattering cross section is defined by Eq. (2.14)

$$\sigma_\mathrm{sca} = \frac{1}{\langle \mathbf{S}_\mathrm{inc} \rangle} \oint_{\partial\Omega} \langle \mathbf{S}_\mathrm{sca} \rangle \cdot \hat{\mathbf{r}} \mathrm{d}\Omega, \tag{C.4}$$

where for the time-averaged Poynting vector $\langle \mathbf{S}_\mathrm{sca} \rangle$ we plug the power flow computed in COMSOL, and $\langle \mathbf{S}_\mathrm{inc} \rangle = E_0^2 / 2\sqrt{\varepsilon_0/\mu_0}$ is the time-averaged Poynting vector of the incoming field. The integration is performed over the boundary between vacuum and PMLs.

The absorption cross section is defined with the help of the dissipated power of Eq. (1.17)

$$\sigma_\mathrm{abs} = \frac{1}{\langle \mathbf{S}_\mathrm{inc} \rangle} \int_\Omega Q_\mathrm{h} \mathrm{d}^3\mathbf{r}, \tag{C.5}$$

where Q_h is the total power dissipation density computed in COMSOL. The integration is performed over the volume of the considered structure.

C.2.2 EELS simulations

For a straightforward implementation of the interaction between a structure and a field of a focused beam of swift electrons, COMSOL is typically used, nevertheless it can be calculated using FDTD too [105]. We follow the COMSOL simulation procedure, which uses the classical dielectric formalism for simulating the STEM-EELS experiment with a focused electron beam as reported in previous studies [18, 55, 106, 107].

The electron beam is defined with the node EDGE CURRENT, which describes a line electric current. We express the current produced by an electron as

$$I = I_0 \mathrm{e}^{\mathrm{i}\omega z/v}, \tag{C.6}$$

where I_0 is the current amplitude, z is the electron trajectory and v electron velocity. With the definition of the electron trajectory as a 1D straight line, we assume a non-recoil approximation, where the electron's trajectory is not deviated by the interaction with the nanostructure. This assumption is very precise for high-energy electrons interacting with optical near fields. We also assume a perfectly focused beam, as the edge current flows through 1D POLYGON.

Within the solution of Eq. (C.2), we can calculate the electric field of the bare electron beam. For such calculation, we position the beam at x_b=400 nm from the origin $\mathbf{r}_\mathrm{probe} = (0, 0, 0)$. In the origin, we situate DOMAIN POINT PROBE, which will enable us to monitor the electric field at the point. To achieve reasonable results, we also put a so-called refined domain, for the mesh to be more fine. We can then directly compare the analytically obtained electric field [Eqs. (2.23) and (2.24)] with this numerically calculated field, multiplied by the elementary charge e, which we show in Fig. C.3 (c). The numerically calculated field bears a small imaginary part, which is most likely due to numerical error. We can see that the relative error is about 3% in Fig. C.3 (d).

With the computed electric field, we can compute the loss probability by the EDGE PROBE monitor with the formula

$$\Gamma_\mathrm{EELS}(\omega) = \frac{e}{\pi\hbar\omega} \int_{z_\mathrm{min}}^{z_\mathrm{max}} \mathrm{Re}\Big\{ E_z^\mathrm{ind}(x_\mathrm{b}, y_\mathrm{b}, z, \omega)\mathrm{e}^{-\mathrm{i}\omega z/v} \Big\} \mathrm{d}z, \tag{C.7}$$

where $(x_\mathrm{b}, y_\mathrm{b})$ is the beam position in the xy-plane. We integrate over the electron trajectory z =(z_min,z_max), which extends over the whole simulation domain. For obtaining loss probability in eV^{-1}, we need to normalize the loss probability Γ_EELS by the factor $e^2/I_0\hbar$.

For the simulations, we used an accelerating voltage of 120 keV (the corresponding electron speed is 58.7% of the speed of light, more typical values are specified in Tab. D.1). For the definition of the electromagnetic response of the material, we use the dielectric function ε_r. We can define it analytically via the Lorentz [Eq. (1.44)] or the Drude model [Eq. (1.45)] or import tabulated data. Relative permeability μ_r is considered to be 1.

All simulations had to be performed twice. First, with the structure defined with its dielectric function, we computed the total field, summing the field of the electron beam and also the induced field. The second simulation that needed to be carried out is with $\varepsilon_\mathrm{r} = 1$ everywhere. Both simulations had to have the same mesh and other specifications. By subtracting the second simulation from the first one we obtain the loss probability.

Lastly, we show relative errors between spectra obtained either from Eq. (C.7) with the one calculated using the model of the loss probability for an induced dipole in Eq. (2.38) as we discuss in Sec. 2.3.3.

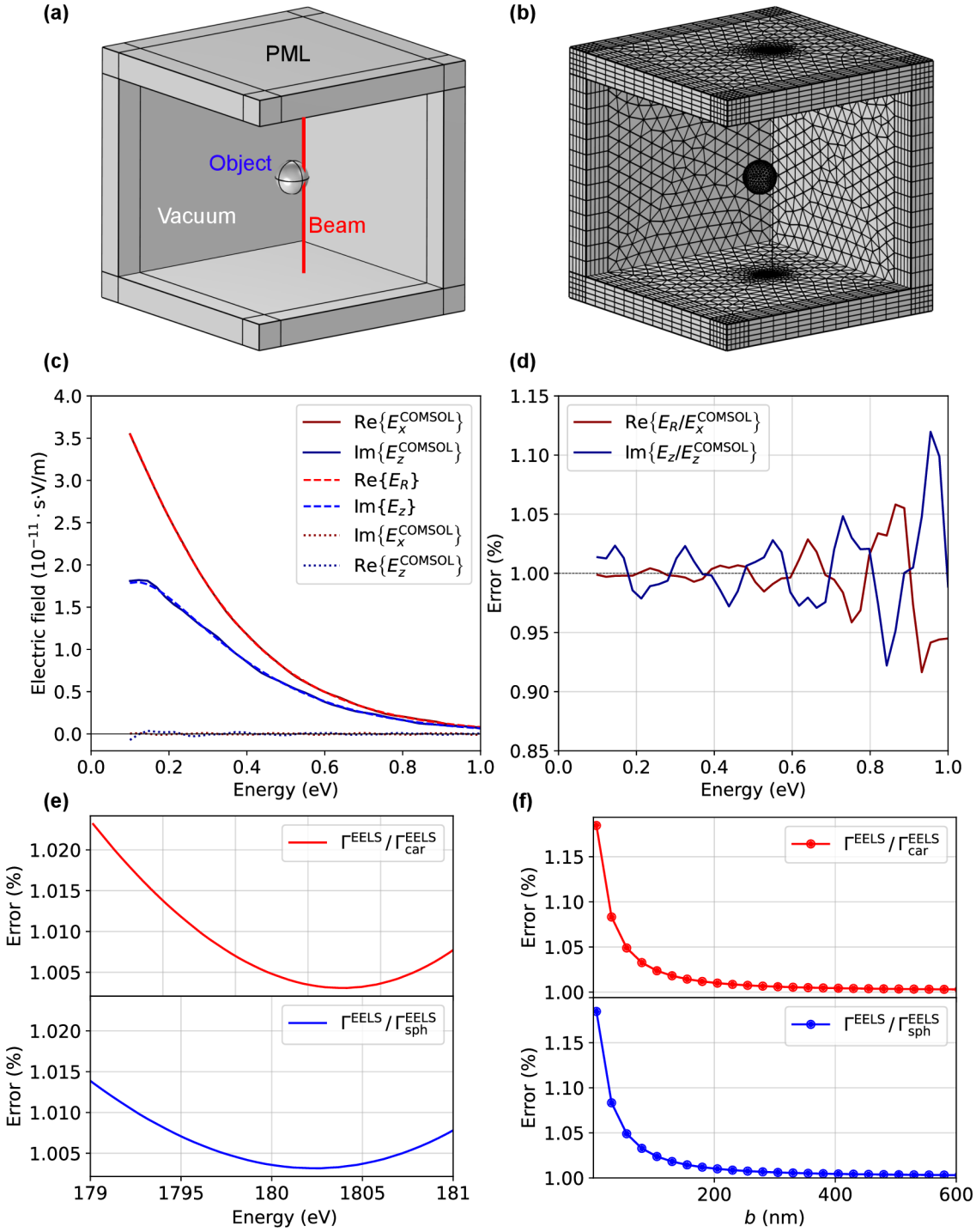

Figure C.3: (a) Geometrical arrangement of EELS simulation in COMSOL. (b) Simulation is discretized into mesh elements, the size of the elements needs to be reduced in the region of large and rapidly changing fields, in this case around the nanostructure and in the vicinity of the electron beam. (c) Comparison of the components of the electric field of a beam of fast electron evaluated 500 nm from the beam. We compare it with the analytical model from Eqs. (2.23) and (2.24) d) Relative error of the electric field components from (c). (e) Relative errors between the loss probabilities are obtained by either integration of the induced field or by the dipole model. (f) Relative errors between the loss probability maxima for different impact parameters b are obtained by either integration of the induced field or by the dipole model.

D Tables

Table D.1: Electron energies and their relativistic velocities (in fraction of the speed of light).

Electron energy / keV	Electron velocity / c
60	0.446
100	0.548
120	0.587
300	0.777

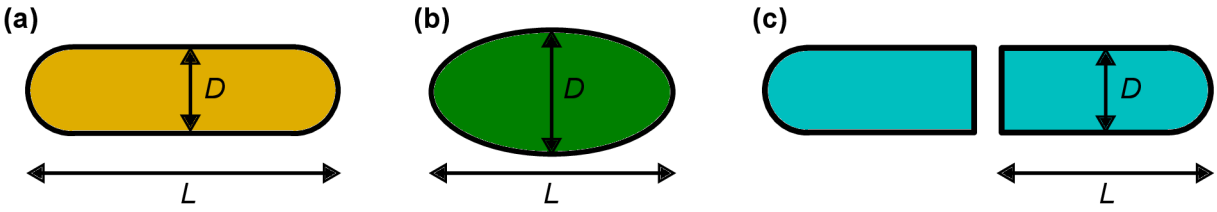

Figure D.1: Schematical depictions of nano-antennas considered in tables, with the labels of their dimensions. (a) Cylindrically shaped nano-antenna with hemispherical apexes, referred to as round-rod. (b) Flat nano-antenna of height 100 nm with elliptical cross section. (c) Dimer antenna consisting of two rods, the size of the gap is 70 nm

Table D.2: Dimensions of different shapes of gold antennas tuned to resonance energy at approximately 0.157 eV. The dimensions legends are schematically depicted in Fig. D.1.

Round-rod		Ellipse		Dimer	
D / nm	L / nm	D / nm	L / nm	D / nm	L / nm
20	1820	100	3300	20	1760
30	2330	200	3400	40	2420
40	2640	300	3500	60	2680
50	2820	600	3600	80	2790
60	2970	1200	3600	100	2815
70	3050	2000	3600		
80	3120	3000	3600		
100	3190	3600	3600		
120	3250				

Table D.3: Dimensions of round-rod gold and hBN nano-antennas tuned to resonance energy at approximately 0.18 eV. The dimensions legend is in Fig. D.1 (a)

Gold		hBN	
Radius	Length	Radius	Length
20	1580	20	60
40	2270	40	120
60	2560	60	180
80	2680	80	239
100	2740	100	295

References

[1] CHALMERS, J. M.; GRIFFITHS, P. R. *Handbook of vibrational spectroscopy*. J. Wiley, 2002. ISBN 978-0471988472.

[2] AROCA, R. F.; ROSS, D. J.; DOMINGO, C. Surface-Enhanced Infrared Spectroscopy. *Applied Spectroscopy*. 2004, vol. 58, no. 11, 324A–338A. Available from DOI: 10.1366/0003702042475420.

[3] SULTANGAZIYEV, A.; BUKASOV, R. Review: Applications of surface-enhanced fluorescence (SEF) spectroscopy in bio-detection and Biosensing. *Sensing and Bio-Sensing Research*. 2020, vol. 30, p. 100382. Available from DOI: 10.1016/j.sbsr.2020.100382.

[4] VOGT, J.; HUCK, C.; NEUBRECH, F.; TOMA, A.; GERBERT, D., et al. Impact of the plasmonic near- and far-field resonance-energy shift on the enhancement of infrared vibrational signals. *Phys. Chem. Chem. Phys.* 2015, vol. 17, pp. 21169–21175. Available from DOI: 10.1039/C4CP04851B.

[5] SCHLÜCKER, S. Surface-Enhanced Raman Spectroscopy: Concepts and Chemical Applications. *Angewandte Chemie (International ed. in English)*. 2014, vol. 53. Available from DOI: 10.1002/anie.201205748.

[6] SHI, X.; COCA-LÓPEZ, N.; JANIK, J.; HARTSCHUH, A. Advances in Tip-Enhanced Near-Field Raman Microscopy Using Nanoantennas. *Chemical Reviews*. 2017, vol. 117, no. 7, pp. 4945–4960. Available from DOI: 10.1021/acs.chemrev.6b00640.

[7] NEUBRECH, F.; PUCCI, A.; CORNELIUS, T. W.; KARIM, S.; GARCÍA-ETXARRI, A., et al. Resonant Plasmonic and Vibrational Coupling in a Tailored Nanoantenna for Infrared Detection. *Phys. Rev. Lett.* 2008, vol. 101, p. 157403. Available from DOI: 10.1103/PhysRevLett.101.157403.

[8] ADATO, R.; AKSU, S.; ALTUG, H. Engineering mid-infrared nanoantennas for surface enhanced infrared absorption spectroscopy. *Materials Today*. 2015, vol. 18, no. 8, pp. 436–446. Available from DOI: https://doi.org/10.1016/j.mattod.2015.03.001.

[9] REZUS, Y. L. A.; SELIG, O. Impact of local-field effects on the plasmonic enhancement of vibrational signals by infrared nanoantennas. *Opt. Express*. 2016, vol. 24, no. 11, pp. 12202–12227. Available from DOI: 10.1364/OE.24.012202.

[10] NEUMAN, T. *Theory of plasmon-enhanced spectroscopy of molecular excitations: infrared absorption, fluorescence, and Raman scattering*. 2018. Ph.D. thesis. University of the Basque Country.

[11] VIRMANI, D.; MACIEL-ESCUDERO, C.; HILLENBRAND, R.; SCHNELL, M. *Prediction and experimental verification of field-enhanced molecular scattering in SEIRA spectroscopy*. 2024. Available from arXiv: 2401.09104 [physics.optics].

[12] HOHENESTER, U. *Nano and Quantum Optics: An introduction to basic principles and theory*. SPRINGER NATURE, 2021. ISBN 978-3-030-30503-1.

[13] NOVOTNY, L.; HECHT, B. *Principles of Nano-Optics*. 2nd ed. Cambridge University Press, 2012. ISBN 978-0511794193.

[14] BENISTY, H.; GREFFET, J.; LALANNE, P. *Introduction to nanophotonics*. Oxford University Press, 2022. ISBN 978–0–19–878613–9.

[15] JACKSON, J. D. *Classical electrodynamics*. Wiley, 1999. ISBN 978-0-471-30932-1.

[16] *ChemSpider, Chemical structure database* [https://www.chemspider.com/Chemical-Structure.9423749.html]. [visited on 2024-05-24].

[17] GLASER, T.; BECK, S.; LUNKENHEIMER, B.; DONHAUSER, D.; KÖHN, A., et al. Infrared Study of the MOO3 doping efficiency in 4,4 -bis(N-carbazolyl)-1,1 -biphenyl (CBP). *Organic Electronics*. 2013, vol. 14, no. 2, pp. 575–583. Available from DOI: 10.1016/j.orgel.2012.11.031.

[18] GOVYADINOV, A. A.; KONEČNÁ, A.; CHUVILIN, A.; VÉLEZ, S.; DOLADO, I., et al. Probing low-energy hyperbolic polaritons in van der waals crystals with an electron microscope. *Nature Communications*. 2017, vol. 8, no. 1. Available from DOI: 10.1038/s41467-017-00056-y.

[19] PALIK, E. D. *Handbook of Optical Constants of Solids*. Academic Press, 1985. ISBN 978-0-12-544422-4.

[20] FOX, M. *Optical properties of solids*. Oxford University Press, 2016. ISBN 978-0-19-957337-0.

[21] GEIM, A. K.; GRIGORIEVA, I. V. Van der waals heterostructures. *Nature*. 2013, vol. 499, no. 7459, pp. 419–425. Available from DOI: 10.1038/nature12385.

[22] BHARADWAJ, P.; DEUTSCH, B.; NOVOTNY, L. Optical Antennas. *Adv. Opt. Photon.* 2009, vol. 1, no. 3, pp. 438–483. Available from DOI: 10.1364/AOP.1.000438.

[23] BEAN, J. A.; TIWARI, B.; BERNSTEIN, G. H.; FAY, P.; POROD, W. Thermal infrared detection using dipole antenna-coupled metal-oxide-metal diodes. *Journal of Vacuum Science amp; Technology B: Microelectronics and Nanometer Structures Processing, Measurement, and Phenomena*. 2009, vol. 27, no. 1, pp. 11–14. Available from DOI: 10.1116/1.3039684.

[24] DERKACS, D.; LIM, S. H.; MATHEU, P.; MAR, W.; YU, E. T. Improved performance of amorphous silicon solar cells via scattering from surface plasmon polaritons in nearby metallic nanoparticles. *Applied Physics Letters*. 2006, vol. 89, no. 9. Available from DOI: 10.1063/1.2336629.

[25] ATWATER, H. A.; POLMAN, A. Plasmonics for improved photovoltaic devices. *Nature Materials*. 2010, vol. 9, no. 3, pp. 205–213. Available from DOI: 10.1038/nmat2629.

[26] CUBUKCU, E.; KORT, E. A.; CROZIER, K. B.; CAPASSO, F. Plasmonic Laser Antenna. *Applied Physics Letters*. 2006, vol. 89, no. 9. Available from DOI: 10.1063/1.2339286.

[27] NOVOTNY, L.; HULST, N. van. Antennas for Light. *Nature Photonics*. 2011, vol. 5, no. 2, pp. 83–90. Available from DOI: 10.1038/nphoton.2010.237.

[28] RAUSCH, T.; TRANTHAM, J. D.; CHU, A. S.; DAKROUB, H.; RIDDERING, J. W., et al. Hamr Drive Performance and Integration Challenges. *IEEE Transactions on Magnetics*. 2013, vol. 49, no. 2, pp. 730–733. Available from DOI: 10.1109/tmag.2012.2218228.

[29] ZHOU, N.; XU, X.; HAMMACK, A. T.; STIPE, B. C.; GAO, K., et al. Plasmonic near-field transducer for heat-assisted magnetic recording. *Nanophotonics*. 2014, vol. 3, no. 3, pp. 141–155. Available from DOI: 10.1515/nanoph-2014-0001.

[30] MITU, S. A.; AHMED, K.; ZAHRANI, F. A.; GROVER, A.; MANI RAJAN, M. S., et al. Development and analysis of surface plasmon resonance based refractive index sensor for pregnancy testing. *Optics and Lasers in Engineering*. 2021, vol. 140, p. 106551. Available from DOI: 10.1016/j.optlaseng.2021.106551.

[31] CALVO-LOZANO, O.; SIERRA, M.; SOLER, M.; ESTÉVEZ, M. C.; CHISCANO-CAMÓN, L., et al. Label-free plasmonic biosensor for Rapid, quantitative, and highly sensitive COVID-19 serology: Implementation and clinical validation. *Analytical Chemistry*. 2021, vol. 94, no. 2, pp. 975–984. Available from DOI: 10.1021/acs.analchem.1c03850.

[32] SZUNERITS, S.; SAADA, H.; PAGNEUX, Q.; BOUKHERROUB, R. Plasmonic approaches for the detection of SARS-COV-2 viral particles. *Biosensors*. 2022, vol. 12, no. 7, p. 548. Available from DOI: 10.3390/bios12070548.

[33] *Merriam Webster dictionary* [https://www.merriam-webster.com/dictionary/antenna]. [visited on 2024-05-24].

[34] NOVOTNY, L. Effective Wavelength Scaling for Optical Antennas. *Phys. Rev. Lett.* 2007, vol. 98, p. 266802. Available from DOI: 10.1103/PhysRevLett.98.266802.

[35] NEUBRECH, F.; HUCK, C.; WEBER, K.; PUCCI, A.; GIESSEN, H. Surface-enhanced infrared spectroscopy using resonant Nanoantennas. *Chemical Reviews*. 2017, vol. 117, no. 7, pp. 5110–5145. Available from DOI: 10.1021/acs.chemrev.6b00743.

[36] CROZIER, K. B.; SUNDARAMURTHY, A.; KINO, G. S.; QUATE, C. F. Optical antennas: Resonators for local field enhancement. *Journal of Applied Physics*. 2003, vol. 94, no. 7, pp. 4632–4642. Available from DOI: 10.1063/1.1602956.

[37] AIZPURUA, J.; BRYANT, G. W.; RICHTER, L. J.; GARCÍA DE ABAJO, F. J.; KELLEY, B. K., et al. Optical properties of coupled metallic nanorods for field-enhanced spectroscopy. *Physical Review B*. 2005, vol. 71, no. 23. Available from DOI: 10.1103/physrevb.71.235420.

[38] NEUMAN, T.; ALONSO-GONZÁLEZ, P.; GARCIA-ETXARRI, A.; SCHNELL, M.; HILLENBRAND, R., et al. Mapping the near fields of Plasmonic Nanoantennas by scattering-type scanning near-field optical microscopy. *Laser amp; Photonics Reviews*. 2015, vol. 9, no. 6, pp. 637–649. Available from DOI: 10.1002/lpor.201500031.

[39] SUN, J.; CARNEY, P. S.; SCHOTLAND, J. C. Strong tip effects in near-field scanning optical tomography. *Journal of Applied Physics*. 2007, vol. 102, no. 10. Available from DOI: 10.1063/1.2812545.

[40] DEUTSCH, B.; HILLENBRAND, R.; NOVOTNY, L. Visualizing the optical interaction tensor of a gold nanoparticle pair. *Nano Letters*. 2010, vol. 10, no. 2, pp. 652–656. Available from DOI: 10.1021/nl9037505.

[41] KELLER, O.; XIAO, M.; BOZHEVOLNYI, S. Configurational resonances in optical near-field microscopy: A rigorous point-dipole approach. *Surface Science*. 1993, vol. 280, no. 1–2, pp. 217–230. Available from DOI: 10.1016/0039-6028(93)90370-y.

[42] *University of Michigan EECS* [https://www.eecs.umich.edu/courses/eecs730/lect/DyadicGF_W09_port.pdf]. [visited on 2024-05-24].

[43] ALONSO-GONZÁLEZ, P.; ALBELLA, P.; SCHNELL, M.; CHEN, J.; HUTH, F., et al. Resolving the electromagnetic mechanism of surface-enhanced light scattering at single hot spots. *Nature Communications*. 2012, vol. 3, no. 1, p. 684. Available from DOI: 10.1038/ncomms1674.

[44] CARNEY, P. S.; SCHOTLAND, J. C.; WOLF, E. Generalized optical theorem for reflection, transmission, and extinction of power for scalar fields. *Phys. Rev. E*. 2004, vol. 70, p. 036611. Available from DOI: 10.1103/PhysRevE.70.036611.

[45] BOHREN, C. F.; HUFFMAN, D. R. *Absorption and scattering of light by small particles*. Wiley-VCH, 2009. ISBN 978-3-527-61816-3.

[46] SCHNELL, M.; SARRIUGARTE, P.; NEUMAN, T.; KHANIKAEV, A. B.; SHVETS, G., et al. Real-space mapping of the chiral near-field distributions in spiral antennas and planar metasurfaces. *Nano Letters*. 2015, vol. 16, no. 1, pp. 663–670. Available from DOI: 10.1021/acs.nanolett.5b04416.

[47] NEUMAN, T.; HUCK, C.; VOGT, J.; NEUBRECH, F.; HILLENBRAND, R., et al. Importance of Plasmonic Scattering for an Optimal Enhancement of Vibrational Absorption in SEIRA with Linear Metallic Antennas. *The Journal of Physical Chemistry C*. 2015, vol. 119, no. 47, pp. 26652–26662. Available from DOI: 10.1021/acs.jpcc.5b08344.

[48] ADATO, R.; ARTAR, A.; ERRAMILLI, S.; ALTUG, H. Engineered Absorption Enhancement and Induced Transparency in Coupled Molecular and Plasmonic Resonator Systems. *Nano Letters*. 2013, vol. 13, no. 6, pp. 2584–2591. Available from DOI: 10.1021/nl400689q.

[49] NORDLANDER, P.; OUBRE, C.; PRODAN, E.; LI, K.; STOCKMAN, M. I. Plasmon hybridization in nanoparticle dimers. *Nano Letters*. 2004, vol. 4, no. 5, pp. 899–903. Available from DOI: 10.1021/nl049681c.

[50] HALAS, N. J.; LAL, S.; CHANG, W.; LINK, S.; NORDLANDER, P. Plasmons in strongly coupled metallic nanostructures. *Chemical Reviews*. 2011, vol. 111, no. 6, pp. 3913–3961. Available from DOI: 10.1021/cr200061k.

[51] DHAWAN, A.; NORTON, S. J.; GERHOLD, . D.; VO-DINH, T. Comparison of FDTD numerical computations and analytical multipole expansion method for plasmonics-active nanosphere dimers. *Opt. Express*. 2009, vol. 17, no. 12, pp. 9688–9703. Available from DOI: 10.1364/OE.17.009688.

[52] CALDWELL, J. D.; KRETININ, A. V.; CHEN, Y.; GIANNINI, V.; FOGLER, M. M., et al. Sub-diffractional volume-confined polaritons in the natural hyperbolic material hexagonal boron nitride. *Nature Communications*. 2014, vol. 5, no. 1. Available from DOI: 10.1038/ncomms6221.

[53] ALFARO-MOZAZ, F. J.; ALONSO-GONZÁLEZ, P.; VÉLEZ, S.; DOLADO, I.; AUTORE, M., et al. Nanoimaging of resonating hyperbolic polaritons in linear boron nitride antennas. *Nature Communications*. 2017, vol. 8, no. 1. Available from DOI: 10.1038/ncomms15624.

[54] AUTORE, M.; LI, P.; DOLADO, I.; ALFARO-MOZAZ, F. J.; ESTEBAN, R., et al. Boron nitride nanoresonators for phonon-enhanced molecular vibrational spectroscopy at the strong coupling limit. *Light: Science amp; Applications*. 2017, vol. 7, no. 4, pp. 17172–17172. Available from DOI: 10.1038/lsa.2017.172.

[55] KONEČNÁ, A.; NEUMAN, T.; AIZPURUA, J.; HILLENBRAND, R. Surface-enhanced molecular electron energy loss spectroscopy. *ACS Nano*. 2018, vol. 12, no. 5, pp. 4775–4786. Available from DOI: 10.1021/acsnano.8b01481.

[56] DOLADO, I.; MACIEL-ESCUDERO, C.; NIKULINA, E.; MODIN, E.; CALAVALLE, F., et al. Remote near-field spectroscopy of vibrational strong coupling between organic molecules and phononic nanoresonators. *Nature Communications*. 2022, vol. 13, no. 1. Available from DOI: 10.1038/s41467-022-34393-4.

[57] GARCÍA DE ABAJO, F. J. Optical excitations in electron microscopy. *Rev. Mod. Phys.* 2010, vol. 82, pp. 209–275. Available from DOI: 10.1103/RevModPhys.82.209.

[58] KRIVANEK, O. L.; LOVEJOY, T. C.; DELLBY, N.; AOKI, T.; CARPENTER, R. W., et al. Vibrational spectroscopy in the electron microscope. *Nature*. 2014, vol. 514, no. 7521, pp. 209–212. Available from DOI: 10.1038/nature13870.

[59] CHU, M.; MYROSHNYCHENKO, V.; CHEN, C. H.; DENG, J.; MOU, C., et al. Probing bright and dark surface-plasmon modes in individual and coupled noble metal nanoparticles using an electron beam. *Nano Letters*. 2009, vol. 9, no. 1, pp. 399–404. Available from DOI: 10.1021/nl803270x.

[60] RITCHIE, R. H. Plasma Losses by Fast Electrons in Thin Films. *Phys. Rev.* 1957, vol. 106, pp. 874–881. Available from DOI: 10.1103/PhysRev.106.874.

[61] MACIEL-ESCUDERO, C. A. *Probing nanoscale light-matter interactions with fast electrons and near-field optical probes*. 2023. Ph.D. thesis. University of the Basque Country.

[62] ALAEE, R.; ROCKSTUHL, C.; FERNANDEZ-CORBATON, I. An electromagnetic multipole expansion beyond the long-wavelength approximation. *Optics Communications*. 2018, vol. 407, pp. 17–21. Available from DOI: 10.1016/j.optcom.2017.08.064.

[63] STUART, B. H. *Infrared Spectroscopy: Fundamentals and Applications*. J. Wiley Sons, 2005. ISBN 978-0-470-85428-0.

[64] BOKOBZA, L. Some applications of vibrational spectroscopy for the analysis of polymers and Polymer Composites. *Polymers*. 2019, vol. 11, no. 7, p. 1159. Available from DOI: 10.3390/polym11071159.

[65] PETIBOIS, C.; DÉLÉRIS, G. Chemical mapping of tumor progression by FT-IR imaging: Towards molecular histopathology. *Trends in Biotechnology*. 2006, vol. 24, no. 10, pp. 455–462. Available from DOI: 10.1016/j.tibtech.2006.08.005.

[66] OLD, O. J.; FULLWOOD, L. M.; SCOTT, R.; LLOYD, G. R.; ALMOND, L. M., et al. Vibrational Spectroscopy for Cancer Diagnostics. *Analytical Methods*. 2014, vol. 6, no. 12, p. 3901. Available from DOI: 10.1039/c3ay42235f.

[67] REHMAN, I. U.; KHAN, R. S.; REHMAN, S. Role of artificial intelligence and vibrational spectroscopy in cancer diagnostics. *Expert Review of Molecular Diagnostics*. 2020, vol. 20, no. 8, pp. 749–755. Available from DOI: 10.1080/14737159.2020.1784008.

[68] RAGAI, J. *The scientist and the forger: Insights into the scientific detection of forgery in paintings*. Imperial College Press, 2015. ISBN 978-1783267408.

[69] CASADIO, F.; DAHER, C.; BELLOT-GURLET, L. Raman spectroscopy of cultural heritage materials: Overview of applications and New Frontiers in instrumentation, sampling modalities, and data processing. *Topics in Current Chemistry*. 2016, vol. 374, no. 5. Available from DOI: 10.1007/s41061-016-0061-z.

[70] WEBER, A.; HOPLIGHT, B.; OGILVIE, .; MURO, C.; KHANDASAMMY, S. R., et al. Innovative Vibrational Spectroscopy Research for Forensic Application. *Analytical Chemistry*. 2023, vol. 95, no. 1, pp. 167–205. Available from DOI: 10.1021/acs.analchem.2c05094.

[71] MARFUNIN, A. S. *Spectroscopy, luminescence and radiation centers in Minerals*. Springer-Verlag, 1979. ISBN 978-3-642-67114-2.

[72] HICKEY, S. M.; UNG, B.; BADER, C.; BROOKS, R.; LAZNIEWSKA, J., et al. Fluorescence microscopy—an outline of hardware, biological handling, and fluorophore considerations. *Cells*. 2021, vol. 11, no. 1, p. 35. Available from DOI: 10.3390/cells11010035.

[73] DATTA, R.; HEASTER, T. M.; SHARICK, J. T.; GILLETTE, A. A.; SKALA, M. C. Fluorescence lifetime imaging microscopy: Fundamentals and advances in instrumentation, analysis, and applications. *Journal of Biomedical Optics*. 2020, vol. 25, no. 07, p. 1. Available from DOI: 10.1117/1.jbo.25.7.071203.

[74] CAMPANELLA, B.; PALLESCHI, V.; LEGNAIOLI, S. Introduction to vibrational spectroscopies. *ChemTexts*. 2021, vol. 7, no. 1. Available from DOI: 10.1007/s40828-020-00129-4.

[75] ORLANDO, A.; FRANCESCHINI, F.; MUSCAS, C.; PIDKOVA, S.; BARTOLI, M., et al. A Comprehensive Review on Raman Spectroscopy Applications. *Chemosensors*. 2021, vol. 9, no. 9. Available from DOI: 10.3390/chemosensors9090262.

[76] FLEISCHMANN, M.; HENDRA, P.J.; MCQUILLAN, A.J. Raman spectra of pyridine adsorbed at a silver electrode. *Chemical Physics Letters*. 1974, vol. 26, no. 2, pp. 163–166. Available from DOI: https://doi.org/10.1016/0009-2614(74)85388-1.

[77] PILOT, R.; SIGNORINI, R.; DURANTE, C.; ORIAN, L.; BHAMIDIPATI, M., et al. A review on surface-enhanced Raman scattering. *Biosensors*. 2019, vol. 9, no. 2, p. 57. Available from DOI: 10.3390/bios9020057.

[78] LE RU, E. C.; ETCHEGOIN, P. G. Quantifying SERS enhancements. *MRS Bulletin*. 2013, vol. 38, no. 8, pp. 631–640. Available from DOI: 10.1557/mrs.2013.158.

[79] HARTSTEIN, A.; KIRTLEY, J. R.; TSANG, J. C. Enhancement of the Infrared Absorption from Molecular Monolayers with Thin Metal Overlayers. *Phys. Rev. Lett.* 1980, vol. 45, pp. 201–204. Available from DOI: 10.1103/PhysRevLett.45.201.

[80] OSAWA, M. Surface-Enhanced Infrared Absorption. In: *Near-Field Optics and Surface Plasmon Polaritons*. Ed. by KAWATA, S. Berlin, Heidelberg : Springer Berlin Heidelberg, 2001, pp. 163–187. ISBN 978-3-540-44552-4. Available from DOI: 10.1007/3-540-44552-8_9.

[81] DREGELY, D.; NEUBRECH, F.; DUAN, H.; VOGELGESANG, R.; GIESSEN, H. Vibrational near-field mapping of planar and buried three-dimensional plasmonic nanostructures. *Nature Communications*. 2013, vol. 4, no. 1. Available from DOI: 10.1038/ncomms3237.

[82] KILGUS, J.; LANGER, G.; DUSWALD, K.; ZIMMERLEITER, R.; ZORIN, I., et al. Diffraction Limited mid-infrared reflectance microspectroscopy with a supercontinuum laser. *Optics Express*. 2018, vol. 26, no. 23, p. 30644. Available from DOI: 10.1364/oe.26.030644.

[83] HUTH, F.; GOVYADINOV, A.; AMARIE, S.; NUANSING, W.; KEILMANN, F., et al. Nano-ftir absorption spectroscopy of molecular fingerprints at 20 nm spatial resolution. *Nano Letters*. 2012, vol. 12, no. 8, pp. 3973–3978. Available from DOI: 10.1021/nl301159v.

[84] ZHOU, W.; KAPETANAKIS, M. D.; PRANGE, M. P.; PANTELIDES, S. T.; PENNYCOOK, S. J., et al. Direct determination of the chemical bonding of individual impurities in graphene. *Physical Review Letters*. 2012, vol. 109, no. 20. Available from DOI: 10.1103/physrevlett.109.206803.

[85] RAMASSE, Q. M.; SEABOURNE, C. R.; KEPAPTSOGLOU, D.; ZAN, R.; BANGERT, U., et al. Probing the bonding and electronic structure of single atom dopants in graphene with electron energy loss spectroscopy. *Nano Letters*. 2013, vol. 13, no. 10, pp. 4989–4995. Available from DOI: 10.1021/nl304187e.

[86] EGERTON, R.F.; LI, P.; MALAC, M. Radiation damage in the TEM and Sem. *Micron*. 2004, vol. 35, no. 6, pp. 399–409. Available from DOI: 10.1016/j.micron.2004.02.003.

[87] EGERTON, R.F. Scattering delocalization and radiation damage in stem–eels. *Ultramicroscopy*. 2017, vol. 180, pp. 115–124. Available from DOI: 10.1016/j.ultramic.2017.02.007.

[88] JOKISAARI, J. R.; HACHTEL, J. A.; HU, X.; MUKHERJEE, A.; WANG, C., et al. Vibrational spectroscopy of water with high spatial resolution. *Advanced Materials*. 2018, vol. 30, no. 36. Available from DOI: 10.1002/adma.201802702.

[89] HAIBER, D. M.; CROZIER, P. A. Nanoscale probing of local hydrogen heterogeneity in disordered carbon nitrides with vibrational electron energy-loss spectroscopy. *ACS Nano*. 2018, vol. 12, no. 6, pp. 5463–5472. Available from DOI: 10.1021/acsnano.8b00884.

[90] HACHTEL, J. A.; HUANG, J.; POPOVS, I.; JANSONE-POPOVA, S.; KEUM, J. K., et al. Identification of site-specific isotopic labels by vibrational spectroscopy in the electron microscope. *Science*. 2019, vol. 363, no. 6426, pp. 525–528. Available from DOI: 10.1126/science.aav5845.

[91] HAGE, F. S.; RADTKE, G.; KEPAPTSOGLOU, D. M.; LAZZERI, M.; RAMASSE, Q. M. Single-atom vibrational spectroscopy in the scanning transmission electron microscope. *Science*. 2020, vol. 367, no. 6482, pp. 1124–1127. Available from DOI: 10.1126/science.aba1136.

[92] KORDAHL, D.; DWYER, C. Enhanced vibrational electron energy-loss spectroscopy of adsorbate molecules. *Physical Review B*. 2019, vol. 99, no. 10. Available from DOI: 10.1103/physrevb.99.104110.

[93] VOGT, J.; ZIMMERMANN, S.; HUCK, C.; TZSCHOPPE, M.; NEUBRECH, F., et al. Chemical identification of individual fine dust particles with resonant plasmonic enhancement of Nanoslits in the infrared. *ACS Photonics*. 2017, vol. 4, no. 3, pp. 560–566. Available from DOI: 10.1021/acsphotonics.6b00812.

[94] SEOK, T. J.; JAMSHIDI, A.; KIM, M.; DHUEY, S.; LAKHANI, A., et al. Radiation Engineering of optical antennas for maximum field enhancement. *Nano Letters*. 2011, vol. 11, no. 7, pp. 2606–2610. Available from DOI: 10.1021/nl2010862.

[95] KONEČNÁ, A. *Theoretical description of low-energy excitations in nanostructures as probed by fast electrons*. 2019. Ph.D. thesis. University of the Basque Country.

[96] KOMRSKA, J. *Fourierovské metody v teorii difrakce a ve strukturní analýze*. VUTIUM, Brno, 2001. ISBN 978-80-214-3532-2.

[97] KONEČNÁ, A. *Interaction of metallic nanoparticles and fast electrons*. 2015. Master thesis. Brno: Vysoké učení technické v Brně, Fakulta strojního inženýrství.

[98] RAJESWARI, R.; JOTHILAKSHMI, R. Modeling and simulation of plasmonic nanoparticles using finite-difference time-domain method: A Review. *Materials Science Forum*. 2014, vol. 781, pp. 33–44. Available from DOI: 10.4028/www.scientific.net/msf.781.33.

[99] YEE, K. Numerical solution of initial boundary value problems involving maxwell's equations in isotropic media. *IEEE Transactions on Antennas and Propagation*. 1966, vol. 14, no. 3, pp. 302–307. Available from DOI: 10.1109/TAP.1966.1138693.

[100] *Lumerical Learning Center* [https://www.lumerical.com]. [visited on 2024-05-24].

[101] HINAMOTO, T.; FUJII, M. MENP: an open-source MATLAB implementation of multipole expansion for nanophotonics. *OSA Continuum*. 2021, vol. 4, no. 5, pp. 1640–1648. Available from DOI: 10.1364/OSAC.425189.

[102] *Comsol Inc. The Finite Element Method (FEM) documentation.* [https://doc.comsol.com/]. [visited on 2024-05-24].

[103] SMAJIC, J.; HAFNER, C.; RAGUIN, L.; TAVZARASHVILI, K.; MISHRIKEY, M. Comparison of numerical methods for the analysis of Plasmonic Structures. *Journal of Computational and Theoretical Nanoscience*. 2009, vol. 6, no. 3, pp. 763–774. Available from DOI: 10.1166/jctn.2009.1107.

[104] HADA, S. L.; RAHMAN, B. M. Rigorous analysis of numerical methods: A comparative study. *Optical and Quantum Electronics*. 2016, vol. 48, no. 6. Available from DOI: 10.1007/s11082-016-0579-x.

[105] CAO, Y.; MANJAVACAS, A.; LARGE, N.; NORDLANDER, P. Electron Energy-loss spectroscopy calculation in finite-difference time-domain package. *ACS Photonics*. 2015, vol. 2, no. 3, pp. 369–375. Available from DOI: 10.1021/ph500408e.

[106] WIENER, A.; DUAN, H.; BOSMAN, M.; HORSFIELD, A. P.; PENDRY, J. B., et al. Electron-energy loss study of nonlocal effects in connected plasmonic Nanoprisms. *ACS Nano*. 2013, vol. 7, no. 7, pp. 6287–6296. Available from DOI: 10.1021/nn402323t.

[107] RAZA, S.; STENGER, N.; PORS, A.; HOLMGAARD, T.; KADKHODAZADEH, S., et al. Extremely confined gap surface-plasmon modes excited by electrons. *Nature Communications*. 2014, vol. 5, no. 1. Available from DOI: 10.1038/ncomms5125.

List of abbreviations

AE	Auger electron
BG	background
CBP	4,4-bis(N-carbazolyl)-1,1-biphenyl
CL	cathodoluminescence
EELS	electron energy-loss spectroscopy
FDTD	finite-difference time-domain method
FEELS	field-enhanced electron energy-loss spectroscopy
FEM	finite element method
FF	far field
FOM	figure of merit
FTIR	Fourier-transformed infrared spectroscopy
FWHM	full width at half maximum
HAMR	heat-assisted magnetic recording
hBN	hexagonal boron nitride
IR	infrared
LSP	localized surface plasmon
MENP	multipole expansion for nanophotonics
NF	near field
NP	no particle
PDMS	polydimethylsiloxane
PMMA	poly(methyl methacrylate)
RES	resonance
RF	radio frequency
SARS-CoV-2	strain of coronavirus, which causes COVID-19 illness
SE	secondary electron
SEF	surface-enhanced fluorescence
SEIRA	surface-enhanced infrared absorption

SERS	surface-enhanced Raman spectroscopy
SNOM	scanning near-field optical microscopy
SPP	surface plasmon polariton
s-SNOM	scattering-type scanning near-field optical microscopy
STEM	scanning transmission electron microscope
TEM	transmission electron microscope
TFSF	total-field scattered-field
ZLP	zero-loss peak